N84-34253

TIMING PERFORMANCE OF PHASED-LOCKED LOOPS IN OPTICAL PULSE POSITION MODULATION COMMUNICATION SYSTEMS

by

D. A. Lafaw
C. S. Gardner

EOSL Publication No. 84-001

Technical Report
August 1984

Supported by
Contract No. NASA NSG-5049

NATIONAL AERONAUTICS & SPACE ADMINISTRATION
Goddard Space Flight Center
Greenbelt, Maryland 20771

ELECTRO-OPTIC SYSTEMS LABORATORY
DEPARTMENT OF ELECTRICAL AND COMPUTER ENGINEERING
COLLEGE OF ENGINEERING
UNIVERSITY OF ILLINOIS
URBANA, ILLINOIS 61801

TIMING PERFORMANCE OF PHASED-LOCKED LOOPS IN OPTICAL PULSE POSITION MODULATION COMMUNICATION SYSTEMS

by

D. A. Lafaw
C. S. Gardner

EOSL Publication No. 84-001

Technical Report
August 1984

Supported by
Contract No. NASA NSG-5049

NATIONAL AERONAUTICS & SPACE ADMINISTRATION
Goddard Space Flight Center
Greenbelt, Maryland 20771

ELECTRO-OPTIC SYSTEMS LABORATORY
DEPARTMENT OF ELECTRICAL AND COMPUTER ENGINEERING
COLLEGE OF ENGINEERING
UNIVERSITY OF ILLINOIS
URBANA, ILLINOIS 61801

ABSTRACT

An optical digital communication system requires that an accurate clock signal be available at the receiver for proper synchronization with the transmitted signal. Phase synchronization is especially critical in M-ary pulse position modulation (PPM) systems where the optimum decision scheme is an energy detector which compares the energy in each of M time slots to decide which of M possible words was sent. Timing errors cause energy spillover into adjacent time slots (a form of intersymbol interference) so that only a portion of the signal energy may be attributed to the correct time slot. This effect decreases the effective signal, increases the effective noise, and increases the probability of error.

In this report, we simulate a timing subsystem for a satellite-to-satellite optical PPM communication link. The receiver employs direct photodetection, preprocessing of the detected signal, and a phase-locked loop for timing synchronization. The variance of the relative phase error is examined under varying signal strength conditions as an indication of loop performance, and simulation results are compared to theoretical calculations.

TABLE OF CONTENTS

CHAPTER 1

INTRODUCTION

In an optical digital communication system, the laser is modulated using an appropriate signaling format. In pulse position modulation (PPM) systems, an accurate clock signal must be available at the receiver to provide proper synchronization with the transmitted signal. In some systems, timing information is sent to the receiver in the form of a special timing signal which is superimposed on the transmitted data waveform. This timing signal is identified and separated at the receiver and used to ensure time synchronization. Alternatively, a receiver could contain a subsystem to extract timing directly from the data stream and no special timing waveform would be required, resulting in a simpler and more power efficient transmitter. A synchronous subsystem usually contains a local oscillator tuned near the expected frequency of the incoming signal. Correct frequency tuning of the local oscillator is essential for synchronous reception. However, the phase of the local oscillator must also agree with that of the incoming signal. Phase synchronization is especially critical in M-ary PPM systems where the optimum decision scheme is an energy detector which compares the energy in each of M time slots in a frame to decide which of M possible words was sent. A timing error causes energy spillover into adjacent time slots (a form of intersymbol interference) so that

only a portion of the signal energy may be attributed to the correct time slot. This effect increases the probability of error. The system must also have the capability to track frequency displacements due to an actual frequency difference between the receiver and transmitter, a drift of the receiver oscillator, or Doppler shift, due to motion between the transmitter and receiver, as in satellite tracking.

The effects of timing errors in optical digital systems have been extensively investigated [1]. Many methods have been proposed and employed for tracking systems including pulse-edge tracking, early-late gate detection, and maximum a posteriori (MAP) estimation. Phase-locked loops have also been studied for use in both optical on-off keying and optical sinusoidal modulation schemes [2], [3].

In this report, we simulate a timing subsystem for a satellite-to-satellite optical PPM communication link. The receiver employs direct photodetection, preprocessing of the optical signal, and a phase-locked loop for timing synchronization. The photodetector output is modeled as a filtered, doubly stochastic Poisson shot noise process. The variance of the relative phase error is examined under varying signal strength conditions as an indication of loop performance, and simulation results are compared to theoretical relations.

CHAPTER 2

DETECTOR MODEL AND SIGNAL PREPROCESSING

A diagram of the proposed receiver timing subsystem is given in Figure 2.1. An optical signal from a free space link or optical fiber is incident on a photodetector which produces an electrical current in response to the incident photons. The photodetector output is preprocessed and applied to the input of a phase-locked loop (PLL) which tracks the signal and supplies timing information to the decision section of the receiver for proper decoding of the data sequence.

2.1 Pulse Position Modulation

The signaling method under consideration is M-ary pulse position modulation (PPM). In PPM, a single pulse is sent in one of M time slots comprising a word or frame. Therefore, M distinct messages can be sent during each frame. In the absence of timing errors, the optimum detection method for optical PPM is an energy detector or photon counter. In this decoding scheme, the receiver compares the number of counts in each of the M time slots and selects the word corresponding to the maximum count. If $M=2^k$, then the PPM signaling format can be used for block encoding, where $M=2^k$ represents a binary word of k bits. If each time slot is T seconds long, the system transmits data at a rate of $R = [(\log_2 M)/MT]$ bits/sec.

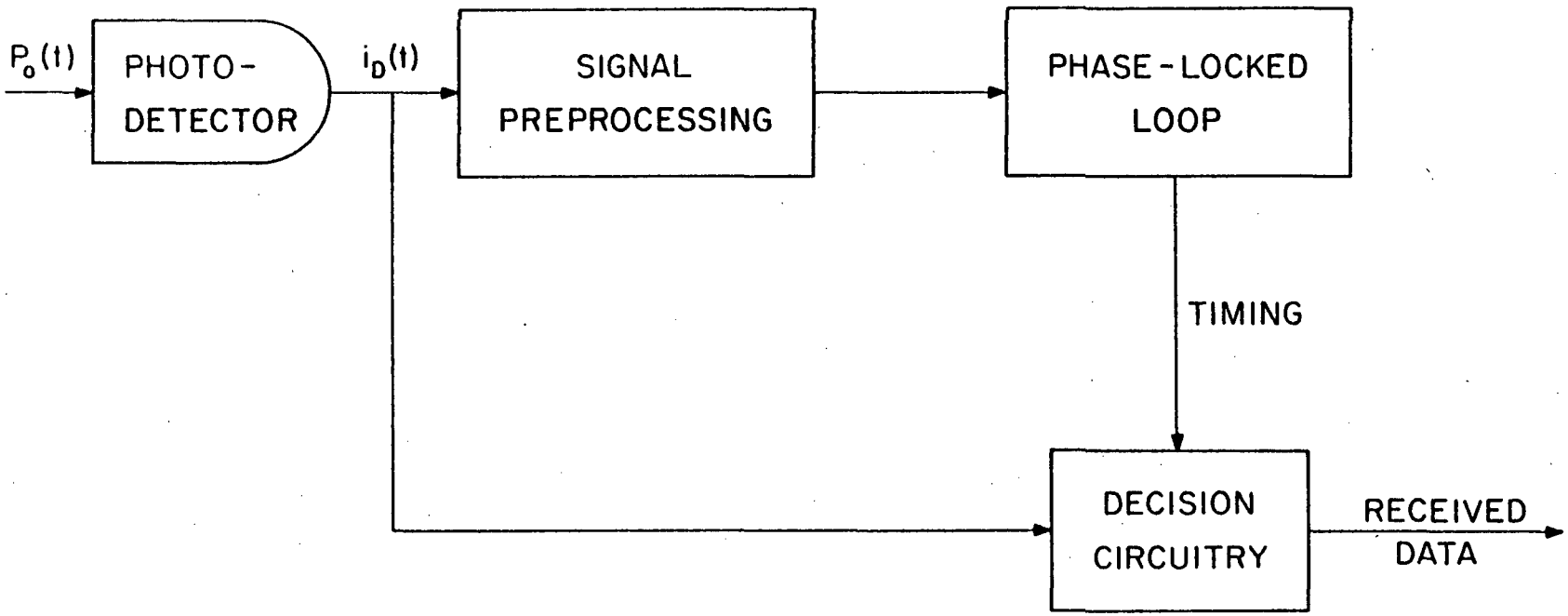

Figure 2.1. Block diagram of the receiver timing subsystem.

Higher-order PPM systems demonstrate superior performance and require less signal power for a given probability of error than other digital signaling methods. However, use of PPM carries stringent timing requirements. Timing offsets during decoding cause only a portion of the signal energy to be included in the signal count for the correct time slot. Some energy will spill over into adjacent slots causing intersymbol interference. This spillover decreases the effective signal power, increases the effective noise, and increases the probability of error.

The performance criterion for block encoded systems is the average probability of making a word error, PWE. From [4], the PWE for a block encoded PPM signaling format with no timing error is

$$PWE = 1 - \frac{\exp[-(K_s + MK_b)]}{M} - \sum_{k=1}^{\infty} Pos(k, K_s + K_b) \times \left[\sum_{j=0}^{k-1} Pos(j, K_b)\right]^{M-1} \left(\frac{1}{Ma}\right)[(1 + a)^M - 1] \tag{2.1}$$

where

$$a \triangleq \frac{K_b^k}{k! \sum_{t=0}^{k} K_b^t/t!}, \quad Pos(k, m_v) \triangleq \frac{(m_v)^k}{k!} \exp(-m_v) \tag{2.2}$$

and

K_s = average signal count

K_b = average background count

M = time slots/word.

The probability of bit error, PBE, is related to the word error

probability by

$$PBE = \frac{k}{2}\left(\frac{M}{M-1}\right) PWE \quad . \tag{2.3}$$

Equation (2.3) is useful for comparing the performance of block encoded PPM to other digital signaling techniques.

2.2 Photodetector Model

The output current of a photodetector, $i_D(t)$, consists of a signal current component, $i_s(t)$, due to the incident optical power on the detector and a Gaussian noise (thermal) current component $i_g(t)$, such that

$$i_D(t) = i_s(t) + i_g(t). \tag{2.4}$$

The signal component $i_s(t)$ of (2.4) is a non-stationary, inhomogeneous shot noise process represented by [4]

$$i_s(t) = \sum_{j=1}^{N(t)} G_j \, w(t - t_j) \tag{2.5}$$

where

t_j = arrival time of the j^{th} photon

$N(t)$ = the total number of arrival photons during $(0,t)$

G_j = random, statistically independent detector gains

$w(t)$ = response of the detector to a single electron.

In response to each arriving photon, the detector produces a primary electron-hole pair. The photon arrival times and thus the electron

release times can be modeled as a filtered, doubly stochastic Poisson process with arrival rate

$$\lambda_R(t) = \lambda_o + \lambda_s \sum_{k=-\infty}^{\infty} p(t - kT_w - c_k T_w/M) \tag{2.6}$$

where the received optical pulse shape, p(t), is a unit-amplitude, square pulse of duration T_w/M shown in Figure 2.2, where λ_s is the signal counting rate defined by

$$\lambda_s = \frac{\eta_d P_o}{hf} \tag{2.7}$$

and

P_o = optical power of the received signal

η_d = quantum efficiency of the detector

h = Planck's constant

f = the optical frequency of the signal

M = the number of time slots in a word

c_k = {0, 1, 2,..., M} is the random data sequence

λ_o = counting rate due to dark current

T_w = word width

T_w/M = time slot width.

Note that $\lambda_R(t)$ is the average rate of the photon arrival times. In any given time period of T seconds, the probability that exactly N counts are detected is given by

$$P[N,(t_o,t_o+T)] = \frac{\mu^N e^{-\mu}}{N!} \tag{2.8}$$

where

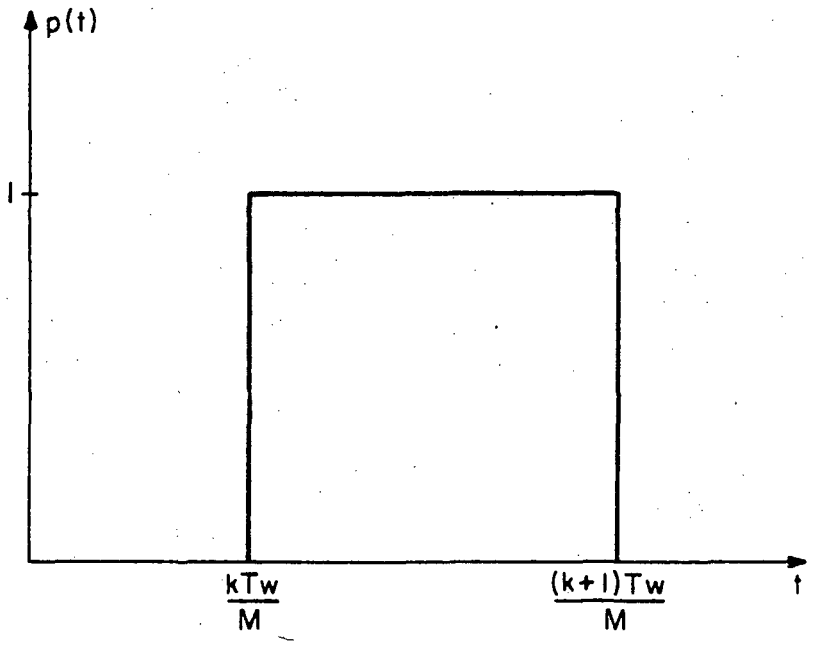

Figure 2.2. The received optical pulse shape, p(t).

$$\mu = \int_{t_o}^{t_o+T} \lambda_R(t)\, dt \quad . \tag{2.9}$$

2.3 Signal Preprocessing

Correct operation of the PLL requires that a dominating frequency component, close to that of the local oscillator in the PLL, be present in the input signal. This frequency component is what the PLL "locks" onto, enabling it to precisely track the input signal. In analog radio communication, for example, the tracked component is the modulating waveform frequency. If we expect successful operation of the PLL under the proposed operating conditions, we must ensure that the PLL input contains an adequate frequency component.

First consider the output from the photodetector described in Section 2.2. Assuming a constant detector gain, a square optical signal pulse, p(t), and neglecting thermal noise, the expectation of the photodetector output conditioned on the random data sequence, c_k, is

$$E\{i_D(t)|c_k\} = w(t) * \lambda_R(t) \tag{2.10}$$

where $\lambda_R(t)$ is the photocount rate given in (2.6) and w(t) is the detector impulse response. The unconditioned expectation of the detector output is

$$E\{i_D(t)\} = w(t) * \langle\lambda_R(t)\rangle \tag{2.11}$$

where

$$\langle\lambda_R(t)\rangle = \lambda_o + \lambda_s \sum_{k=-\infty}^{\infty} \sum_{j=0}^{M-1} \frac{1}{M}\, p(t - kT_w - jT_w/M) \quad . \tag{2.12}$$

The second term of (2.12) is the signal pulse shape averaged over the M slots in a word. Since the received signal pulse shape, p(t), is square, the second term of (2.12) is a constant. Therefore, (2.12) reduces to

$$\langle \lambda_R(t) \rangle = \lambda_o + \frac{\lambda_s}{M} \tag{2.13}$$

and

$$E\{i_D(t)\} = \text{constant} \tag{2.14}$$

which implies

$$F[E\{i_D(t)\}] = 2\pi(\text{constant})\ \delta(\omega). \tag{2.15}$$

From this analysis, we conclude that, for a square pulse shape, there is no trackable frequency component in an expected detector output signal, only a dc term is present. Modeling p(t) as a square pulse represents a worst case situation. If p(t) has a shape other than square, (2.13) would no longer hold and other frequency components would appear in the output spectrum. However, further analysis would be required to determine if the frequency components generated would be of sufficient amplitude for the PLL to track.

We now consider a form of signal processing which will result in a trackable frequency component in the spectrum of the signal before it is applied to the PLL input. Figure 2.3 is a block diagram of the proposed detector and signal preprocessor model. The use of a linear operation

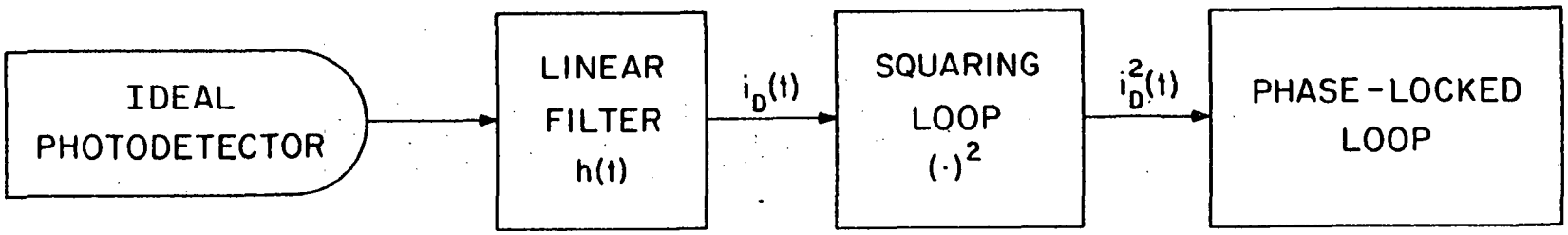

Figure 2.3. Block diagram of the proposed detector and signal preprocessor model. The linear filter, h(t), includes the photodetector impulse response.

will result only in a convolution in the time domain or multiplication in the frequency domain which will change nothing but the magnitude of the output spectrum. A nonlinear operation is needed to produce a frequency component at the slot rate. A square-law device was selected to produce the nonlinear effect because of its simplicity and ease of implementation and analysis.

Consider the expected value of the square of the detector output current. From Reference [4] we have

$$E\{i_D^2(t)\} = \langle [h(t) * \lambda_R(t)]^2 \rangle + h^2(t) * \langle \lambda_R(t) \rangle \tag{2.16}$$

where h(t) is the combined impulse response of the detector and an additional linear filter contained in the preprocessor. Again, we assume a square, unit-amplitude signal pulse, p(t). Since p(t) is a square pulse, $\langle \lambda_R(t) \rangle$ is again a constant and thus the second term of (2.16) is also a constant. However, the first term in (2.16) can be written as

$$h(t) * \lambda_R(t) = \lambda_o \int_{-\infty}^{\infty} h(t)\, dt + \lambda_s \sum_{k=-\infty}^{\infty} g(t - kT_w - c_k T_w/M) \tag{2.17}$$

where

$$g(t) = h(t) * p(t). \tag{2.18}$$

For computational convenience let

$$\int_{-\infty}^{\infty} h(t)\, dt = 1 \quad . \tag{2.19}$$

In this case, we obtain

$$\langle [h(t) * \lambda_R(t)]^2 \rangle = \lambda_o + \frac{2\lambda_o\lambda_s}{M}$$

$$+ \lambda_s \sum_{j=-\infty}^{\infty} \sum_{k=-\infty}^{\infty} \langle g(t - kT_w - c_kT_w/M) \cdot g(t - jT_w - c_jT_w/M) \rangle \quad . \tag{2.20}$$

The first two terms of (2.20) are constants. Assuming the pulses occupying the time slots are narrow and no significant overlap occurs, the cross terms of the double summation in (2.20) are negligible. The more slots per word, the better this approximation will be. Use of this approximation implies that the only significant terms in the summation are those for which j=k, and we obtain

$$\lambda_s \sum_{j=-\infty}^{\infty} \sum_{k=-\infty}^{\infty} \langle \cdot \rangle \simeq \lambda_s^2 \sum_{k=-\infty}^{\infty} \langle g^2(t - kT_w - c_kT_w/M) \rangle \tag{2.21}$$

so that

$$\lambda_s^2 \sum_{k=-\infty}^{\infty} \langle g^2(t - kT_w - c_kT_w/M) \rangle = \lambda_s^2 \sum_{n=-\infty}^{\infty} \frac{1}{M} g^2(t - nT_w/M) \quad . \tag{2.22}$$

After substituting (2.22), (2.21), and (2.20) into (2.16), we obtain

$$E\{i_D^2(t)\} \simeq \left(\lambda_o + \frac{\lambda_s}{M}\right) \int_{-\infty}^{\infty} h^2(t)\, dt + \left[\lambda_o^2 + \frac{2\lambda_s\lambda_o}{M}\right] \left[\int_{-\infty}^{\infty} h(t)\, dt\right]^2$$

$$+ \frac{\lambda_s^2}{M} \sum_{k=-\infty}^{\infty} g^2(t - kT_w/M) \quad . \tag{2.23}$$

Since all but the last term are constants, (2.23) is equivalently expressed as

$$E\{i_D^2(t)\} \simeq K + \frac{\lambda_s^2}{M}[h(t) * p(t)]^2 * \sum_{k=-\infty}^{\infty} \delta(t - kT_w/M) \tag{2.24}$$

where K denotes the sum of the constant terms of (2.23).

Taking the Fourier transform of (2.24) yields

$$[E\{i_D^2(t)\}] = 2\pi K\delta(\omega) + \frac{2\pi\lambda_s^2}{T_w}[H(\omega)P(\omega)] * [H(\omega)P(\omega)] \times \sum_{k=-\infty}^{\infty} \delta(\omega - k2\pi M/T_w) \tag{2.25}$$

where $H(\omega)$ and $P(\omega)$ are the Fourier transforms of h(t) and p(t), respectively. $P(\omega)$ is simply the transform of the transmitted square pulse and is given by

$$P(\omega) = \int_0^{\frac{T_w}{M}} e^{-j\omega t}\, dt = \frac{T_w}{M}\frac{\sin(\omega T_w/2M)}{\omega T_w/2M} e^{-j\frac{\omega T_w}{2M}} \quad . \tag{2.26}$$

From (2.25) it is apparent that we have spectral frequency components at

$$\omega_n = \frac{2\pi M}{T_w} n \quad . \tag{2.27}$$

When n=1, ω_1 corresponds to the time slot transmission rate. $H(\omega)$ should be chosen to maximize the signal component at ω_1 and to minimize the other background noise components.

The next step is to put a constraint on the choice of the combined receiver filter impulse response. First, the detector output can be represented by

$$i(t) = \overline{i(t)} + \Delta i(t) \tag{2.28}$$

where the subscripts are dropped for convenience, and $\overline{i(t)} = E\{i(t)\}$. The squared output of the detector is

$$i^2(t) = \overline{i(t)}^2 + 2\overline{i(t)}\,\Delta i(t) + \Delta i^2(t) \quad . \tag{2.29}$$

Taking expectations on both sides of (2.29) and assuming $E\{\Delta i(t)\} = 0$ give

$$\overline{i^2(t)} = \overline{i(t)}^2 + \overline{\Delta i^2(t)} \quad . \tag{2.30}$$

Substituting (2.30) into (2.29) yields

$$i^2(t) = \overline{i^2(t)} + 2\overline{i(t)}\,\Delta i(t) + [\Delta i^2(t) - \overline{\Delta i^2(t)}] \quad . \tag{2.31}$$

In comparision to the first two terms of (2.31), the third term, $\Delta i^2(t) - \overline{\Delta i^2(t)}$, is considered small and can be neglected for a first approximation, leaving

$$i^2(t) \simeq \overline{i^2(t)} + 2\overline{i(t)}\,\Delta i(t) \quad . \tag{2.32}$$

To examine the power density spectrum of (2.32), we first calculate the autocorrelation function

$$\begin{aligned} \langle i^2(t_1), i^2(t_2)\rangle = {} & \overline{i^2(t_1)}\;\overline{i^2(t_2)} + 4\overline{i(t_1)}\;\overline{i(t_2)} \\ & \times [i(t_1) - \overline{i(t_1)}][i(t_2) - \overline{i(t_2)}] \quad . \end{aligned} \tag{2.33}$$

The first term of (2.33) is the expected output signal from the squaring loop which contains a nonzero frequency component; the second term is noise. To minimize the noise term, remember

$$\overline{i(t)} = h(t) * \langle \lambda_R(t) \rangle . \tag{2.34}$$

So if $H(\omega)$ is chosen such that

$$H(0) = 0 \tag{2.35}$$

the first noise term in (2.33) vanishes. Many functions satisfy (2.35) and an optimal choice of $H(\omega)$ is beyond the scope of this report. An intuitive choice is the bandlimited derivative function of Figure 2.4a, with impulse response, $h(t)$, plotted in Figure 2.4b. It can be shown that the optimum bandwidth, B_o, is equal to the time slot frequency. A sinusoidal function also satisfies (2.35). In the simulation model

$$h(t) = \sin\left(\frac{2\pi M}{T_w} t\right) , \quad |t| \leq \frac{T_w}{2M} \tag{2.36}$$

which is plotted in Figure 2.5a. The Fourier transform of $h(t)$ is given by

$$H(\omega) = \frac{\pi T_w}{jM}\left[\frac{\sin\left[\frac{T_w}{2M}\left(\omega - \frac{2\pi M}{T_w}\right)\right]}{\frac{T_w}{2M}\left(\omega - \frac{2\pi M}{T_w}\right)} - \frac{\sin\left[\frac{T_w}{2M}\left(\omega + \frac{2\pi M}{T_w}\right)\right]}{\frac{T_w}{2M}\left(\omega + \frac{2\pi M}{T_w}\right)}\right] \tag{2.37}$$

and plotted in Figure 2.5b. This filter was used because of its easier, more efficient implementation in software. Preprocessing the detector output as described above will generate a spectral component at the time slot frequency which can now be tracked by the PLL.

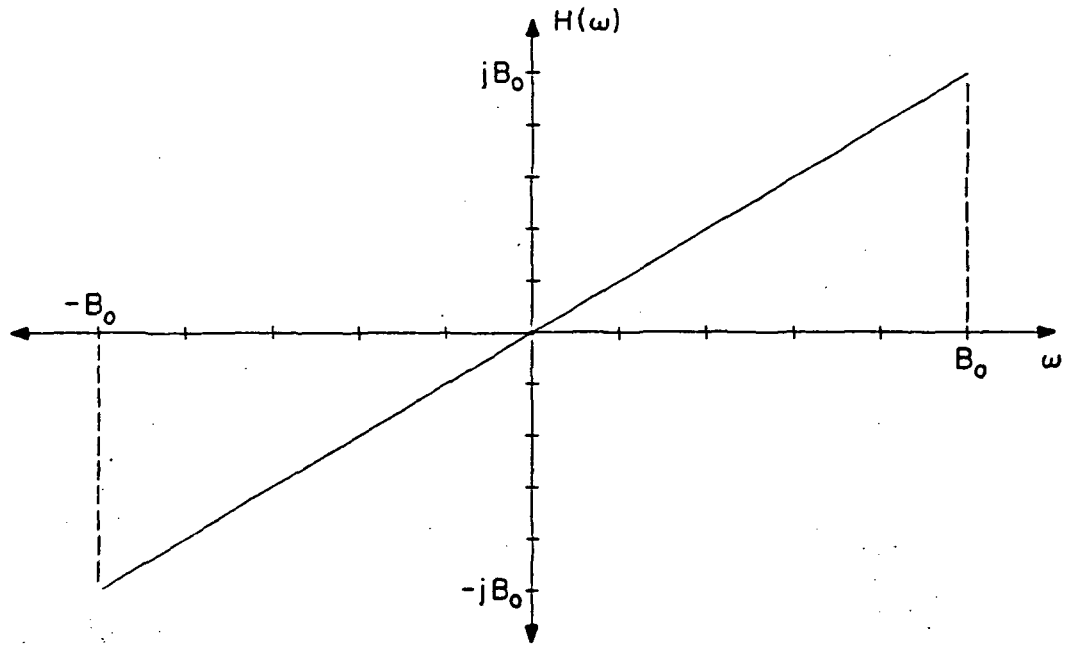

Figure 2.4a. Bandlimited derivative function.

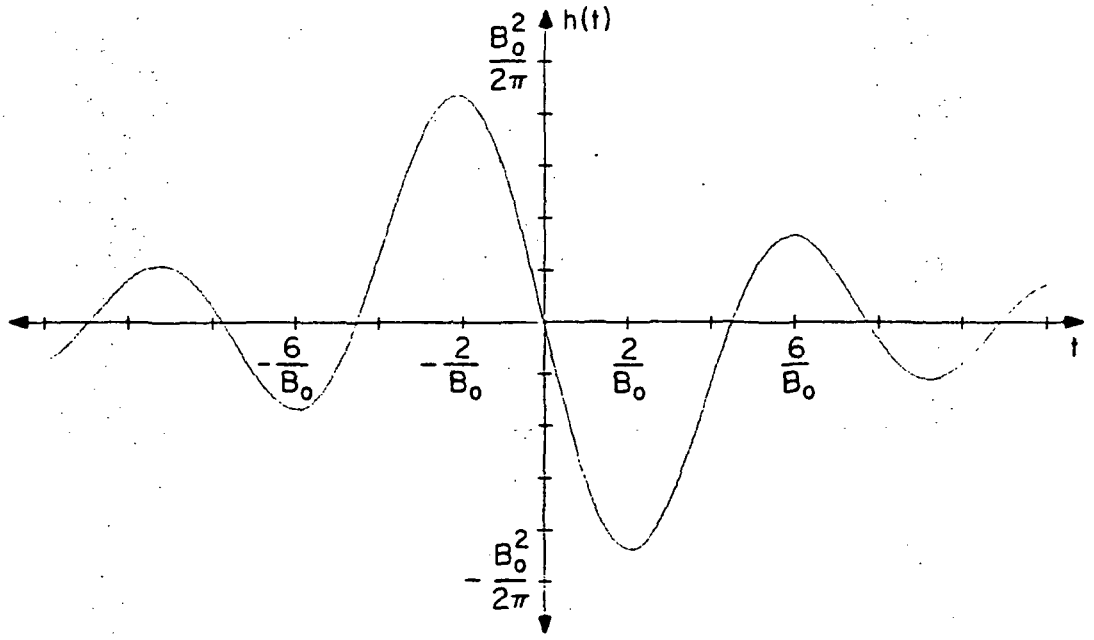

Figure 2.4b. Impulse response of the bandlimited derivative function of Figure 2.4a.

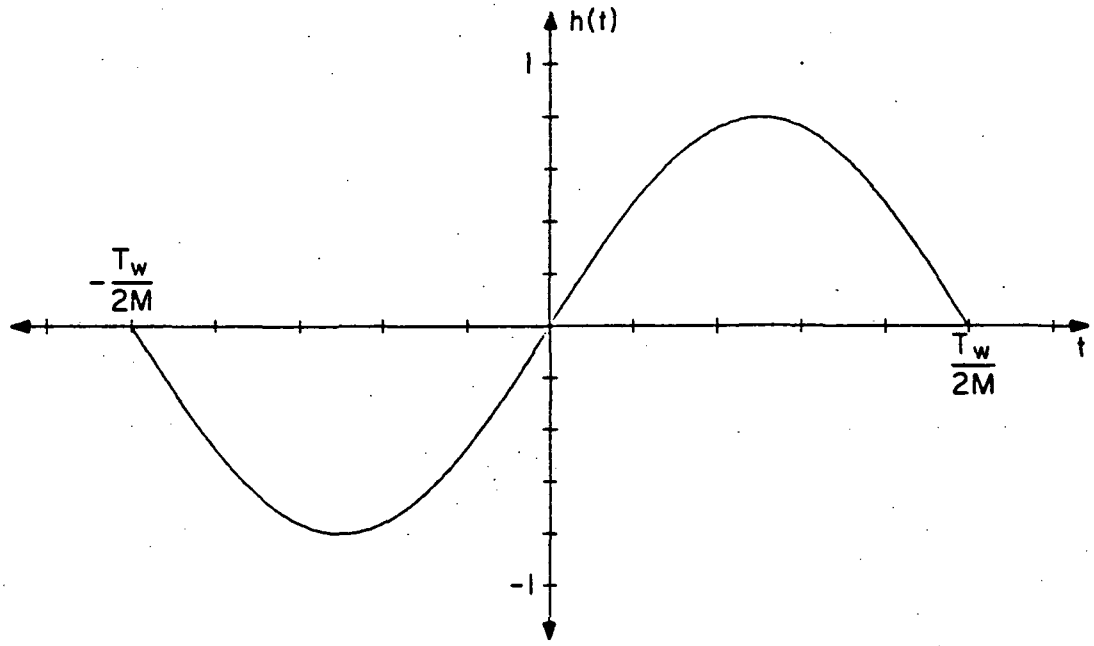

Figure 2.5a. Impulse response of sinusoidal filter used in the simulation model.

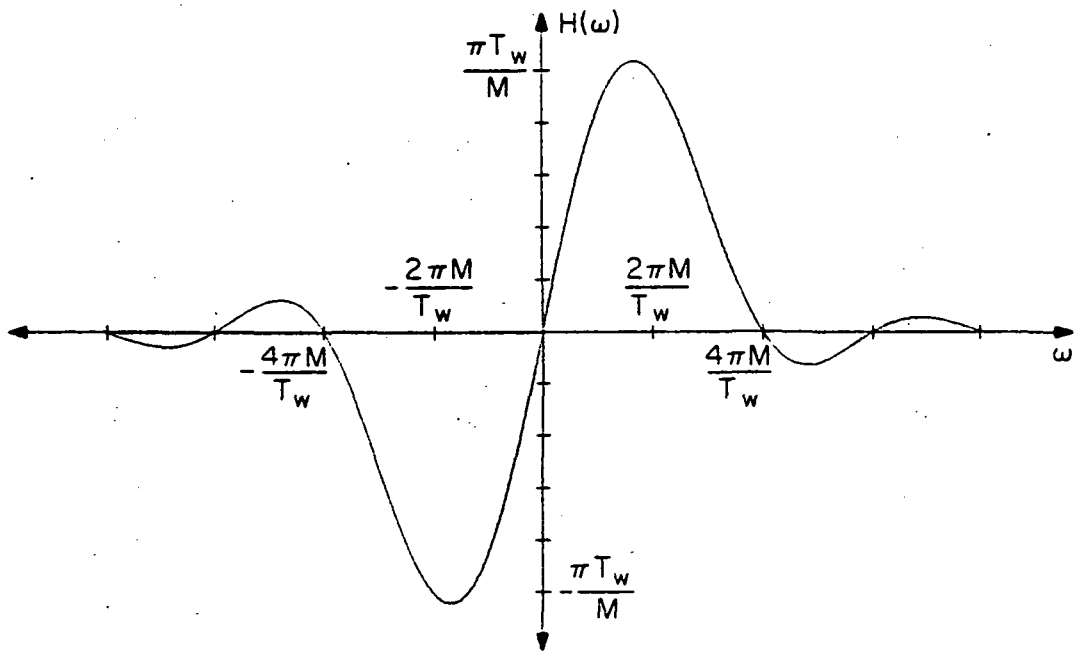

Figure 2.5b. Frequency response of the sinusoidal filter used in the simulation model. This filter approximates the ideal low-pass differentiator plotted in Figure 2.4a.

CHAPTER 3

DESIGN AND ANALYSIS OF THE PHASE-LOCKED LOOP

3.1 Mathematical Model of the Phase-Locked Loop

A block diagram of a phase-locked loop (PLL) is given in Figure 3.1. In the basic operation of the PLL, a phase detector measures the phase difference between its two inputs and then outputs a voltage proportional to this difference, $v_d(t)$. The difference voltage is then passed through a loop filter and fed into a voltage controlled oscillator (VCO) which changes its frequency in a direction to minimize the phase difference between the VCO output and the input signal. The loop is said to be "locked" when the control voltage applied to the VCO keeps the frequency of the VCO equal to the average frequency of the incoming signal.

For the analysis of the PLL, assume that the input signal has phase $\theta_s(t)$, the VCO output has phase $\theta_o(t)$, and that the loop is locked. The phase detector is modeled as a perfect multiplier of gain K_m whose output, over a specified operating range, is a direct voltage, $v_d(t)$, that is a function of the phase difference $\theta_s(t) - \theta_o(t)$. Under locked conditions the phase difference will be small and the phase detector output is [5]

$$v_d(t) = K_d[\theta_s(t) - \theta_o(t)] \tag{3.1}$$

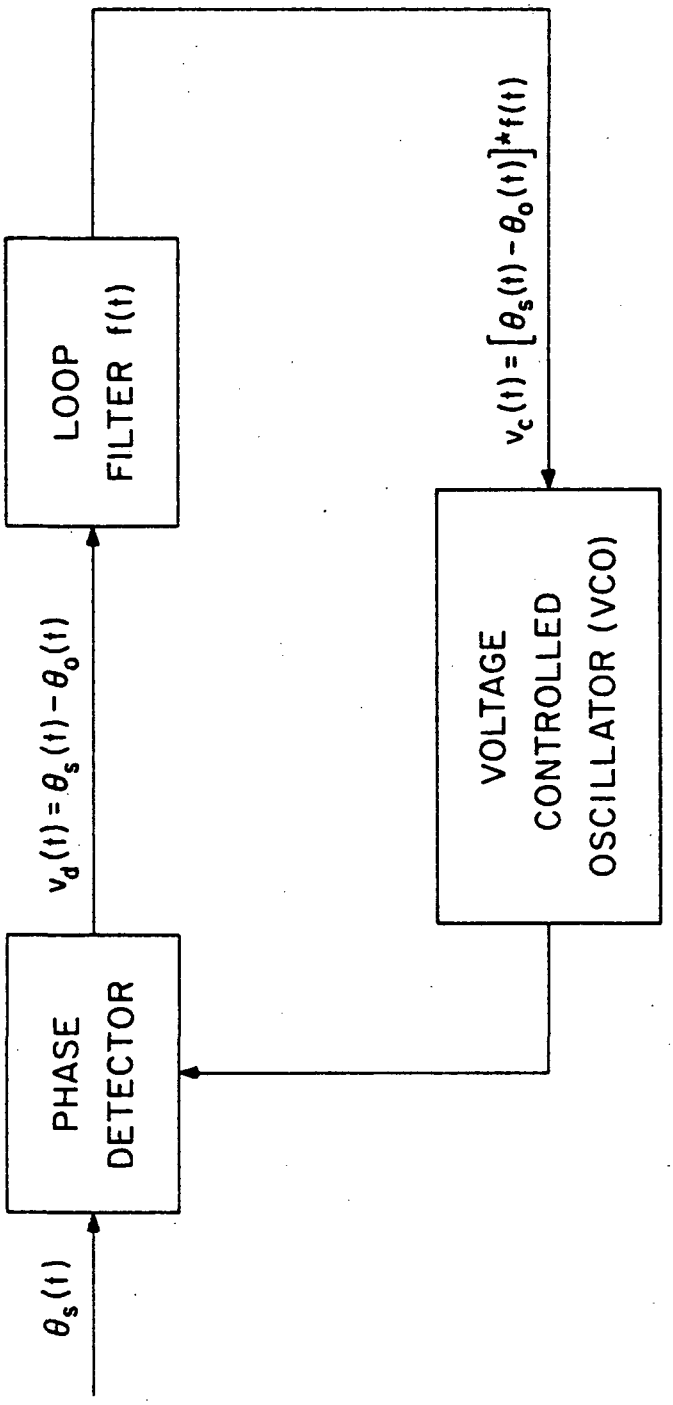

Figure 3.1. Block diagram of a phase-locked loop (PLL).

where

$$K_d = K_m A_o A_s \tag{3.2}$$

is the phase detector gain and A_o and A_s are the amplitudes of the VCO output and input signals, respectively.

To reject high frequency signal components, the phase detector voltage is filtered by a low-pass loop filter of transfer function F(s). The resulting control voltage is then applied to the VCO.

The VCO has a free-running frequency ω_f and an instantaneous frequency shift proportional to the control voltage input, $\Delta\omega = K_o v_c(t)$, where K_o is the VCO gain constant and $v_c(t)$ is the filter output voltage. The VCO output frequency is written as

$$\omega_o = \omega_f + \Delta\omega_f = \omega_f + K_o v_c(t) \quad . \tag{3.3}$$

Noting that frequency is the derivative of phase, we see that

$$\frac{d\theta_o(t)}{dt} = K_o v_c(t) \quad . \tag{3.4}$$

Using the Laplace tranforms of (3.1) and (3.4) we arrive at the linearized mathematical PLL model of Figure 3.2. The loop transfer function of Figure 3.2 is

$$\frac{\theta_o(t)}{\theta_s(t)} = H(s) = \frac{K_o K_d F(s)}{s + K_o K_d F(s)} \quad . \tag{3.5}$$

For a further analysis we need to specify F(s). Using a simple low-pass filter, F(s) is of the form

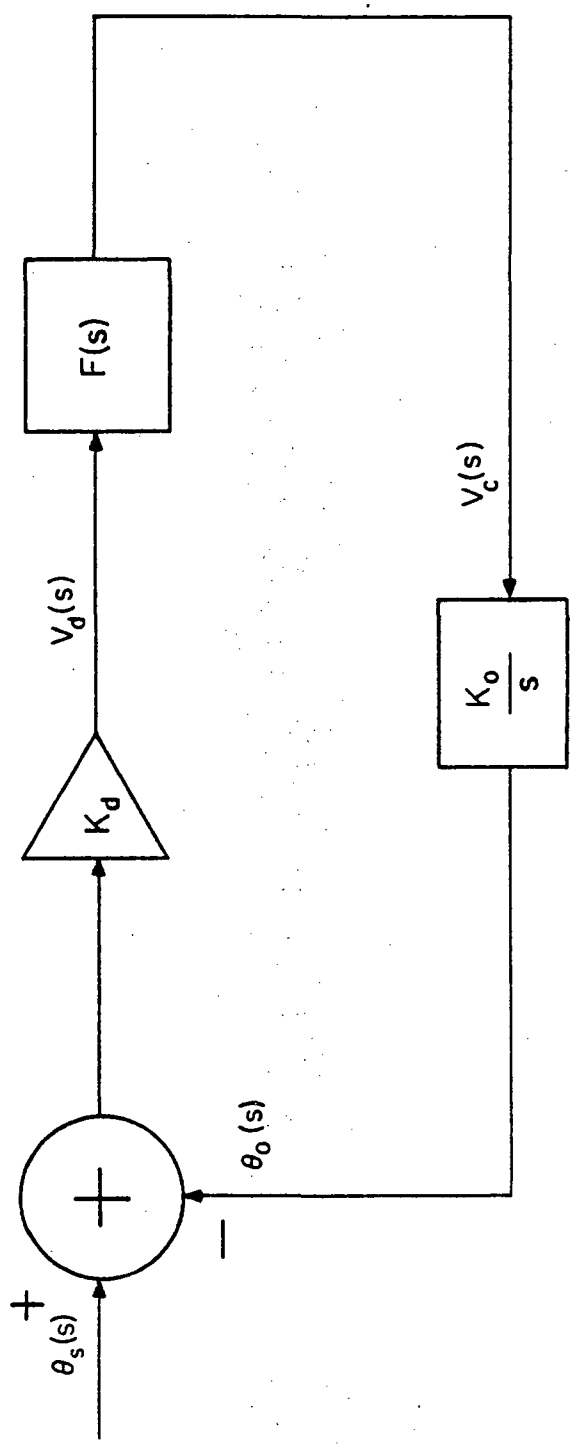

Figure 3.2. Linearized mathematical model of the phase-locked loop.

$$F(s) = \frac{1}{s\tau + 1} \tag{3.6}$$

where $1/\tau$ is the 3 db cutoff frequency of the filter. Substituting (3.6) into (3.5), the loop transfer function becomes

$$H(s) = \frac{K_o K_d/\tau}{s^2 + s/\tau + K_o K_d/\tau} \quad . \tag{3.7}$$

From control theory let us define ξ as the damping ratio and ω_N as the natural undamped frequency. The denominator of (3.7) is the characteristic equation of the system that determines the system response and is defined by

$$\Delta = s^2 + 2\xi\omega_N s + \omega_N^2 \tag{3.8}$$

which implies

$$\omega_N = \left(\frac{K_o K_d}{\tau}\right)^{1/2} \tag{3.9}$$

and

$$\xi = \frac{1}{2}\left(\frac{1}{\tau K_o K_d}\right)^{1/2} \tag{3.10}$$

The selection of the damping ratio is of particular importance. With too large a value of ξ, the system response is overdamped, resulting in a very long response time to an input. With too low a value, the system is underdamped, causing oscillation about the steady-state value and requiring a long time for a settled final response.

Two final design parameters to consider are the lock-in range and

hold-in range, $\Delta\omega_L$ and $\Delta\omega_H$, respectively. When the difference between the free-running VCO frequency and the average incoming frequency is less than the 3 db loop bandwidth, the loop will lock up almost immediately without skipping cycles. The maximum frequency for which this is possible is the lock-in range and is roughly equivalent to the loop bandwidth [5]. The range of frequency difference over which a loop will maintain phase lock is the hold-in range and is defined by [5]

$$\Delta\omega_H = \pm K_o K_d F(s) \quad . \tag{3.11}$$

More detailed discussion and derivation of PLL design parameters can be found in [5] and [6].

3.2 Selection of Design Parameters

Successful PLL design represents a compromise between performance features. A wide loop bandwidth will result in a fast acquisition and lock-up time as well as an extended lock-in range, but will admit more noise, may have a smaller hold-in range, and be more sensitive to small changes in the input signal frequency. Alternatively, a narrow loop bandwidth insures good noise performance and will tolerate a larger amount of input frequency change without losing lock, but will have difficulty initially acquiring phase-lock. Advanced techniques such as frequency sweeping and loop bandwidth changing have been developed for acquiring lock even with very narrow bandwidths, but they are beyond the scope of this report. A thorough treatment may be found in [6].

3.2.1 Simulated PLL parameters

The simulations described in this report used one-second time slots which correspond to an expected input frequency (slot rate) of 2π rad/sec. The VCO free-running frequency was selected as 6.18 rad/sec. The difference of 0.103 rad/sec represents a 1.6% deviation from the expected input frequency, and is used to account for uncertainties about the exact frequency of the received signal. Such uncertainties are commonly caused by Doppler shifts, drift in the transmitted clock, or drift of the receiver local oscillator. The phase detector gain, VCO gain constant, loop filter bandwidth, and damping ratio were chosen as:

$$K_d = 0.3333 \quad V/rad$$

$$K_o = 1.0 \quad rad/sec/V$$

$$1/\tau = 0.3333 \quad rad/sec$$

$$\xi = 0.5$$

which yield the parameters:

$$\Delta\omega_H = 0.3333 \quad rad/sec$$

$$\Delta\omega_L = 0.42 \quad rad/sec.$$

It is important to recall from (2.2) that the phase detector gain K_d is dependent on the amplitude of the input signal, A_s. In fact, we are implicitly assuming that the average magnitude of A_s is equal to one. If the value of K_d changes due to a change in A_s, the design parameters of the PLL also change. For example, if A_s increases from 1 to 10, the 3 db loop bandwidth increases from 0.42 to 1.6 rad/sec causing the loop to reject less noise than originally intended. Realistically, the input signal will vary over a substantial range of values and the square-law

device in the preprocessor compounds the problem. To compensate for varying signal amplitudes, an attenuator is placed between the squaring loop and the PLL input. This device will adjust the preprocessor output signal to insure the average PLL input signal will not exceed unity.

To choose the attenuation constant, we first must find the expected value of the amplitude out of the preprocessing components. As in Chapter 2, let g(t) denote the convolution of the input pulse shape, p(t), and the combined receiver impulse response, h(t). Let each pulse have amplitude P_o and width $T=T_w/M$ sec. From (2.33), the receiver impulse response is

$$h(t) = \sin\left(\frac{2\pi}{T} t\right) \quad , \quad |t| \leq \frac{T}{2} \quad . \tag{3.12}$$

Convolving h(t) with p(t) yields

$$g(t) = \begin{cases} -\frac{P_o T}{2\pi}\left(1 - \cos\frac{2\pi}{T} t\right) & , \quad -T \leq t \leq 0 \\ +\frac{P_o T}{2\pi}\left(1 - \cos\frac{2\pi}{T} t\right) & , \quad 0 \leq t \leq T \quad . \end{cases} \tag{3.13}$$

Figure 3.3a shows that as a result of the convolution operation, g(t) has duration 2T. After passing g(t) through the squaring loop, we obtain

$$g^2(t) = \frac{3P_o^2T^2}{8\pi^2} - \frac{P_o^2T^2}{2\pi^2}\cos\frac{2\pi}{T} t + \frac{P_o^2T^2}{8\pi^2}\cos\frac{4\pi}{T} t, \quad -T \leq t \leq T \ , \tag{3.14}$$

which consists of two identical, positive waveforms each of duration T, as shown in Figure 3.3b. Thus, the total amplitude of the fundamental frequency component of $g^2(t)$ is

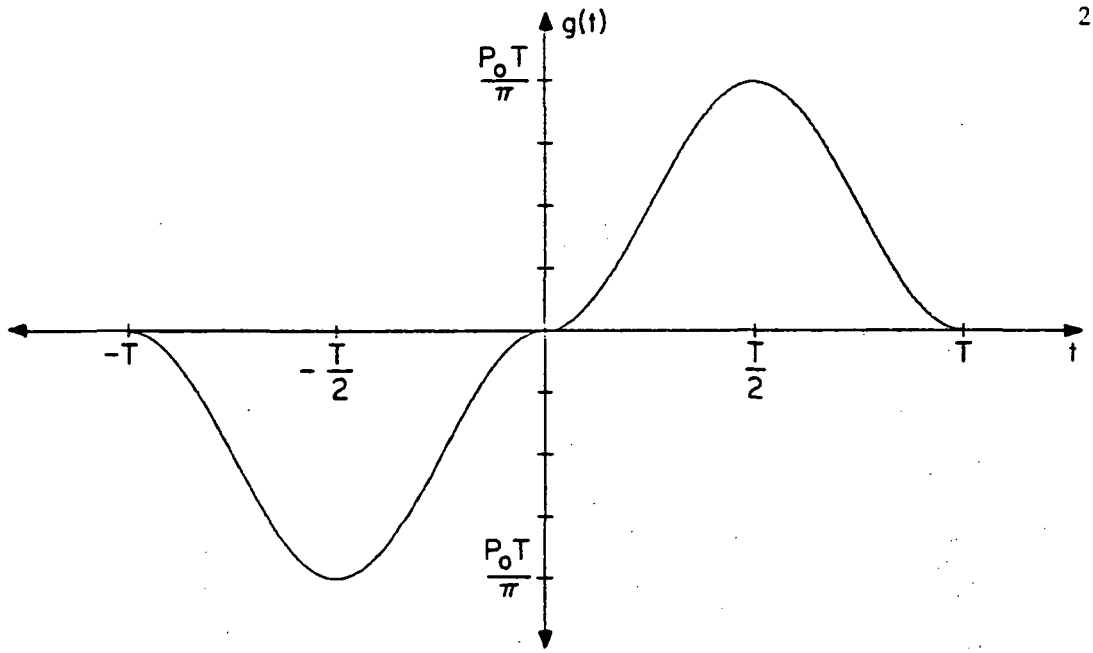

Figure 3.3a. Result of convolving a sinusoidal receiver impulse response, h(t), with a square signal pulse, p(t).

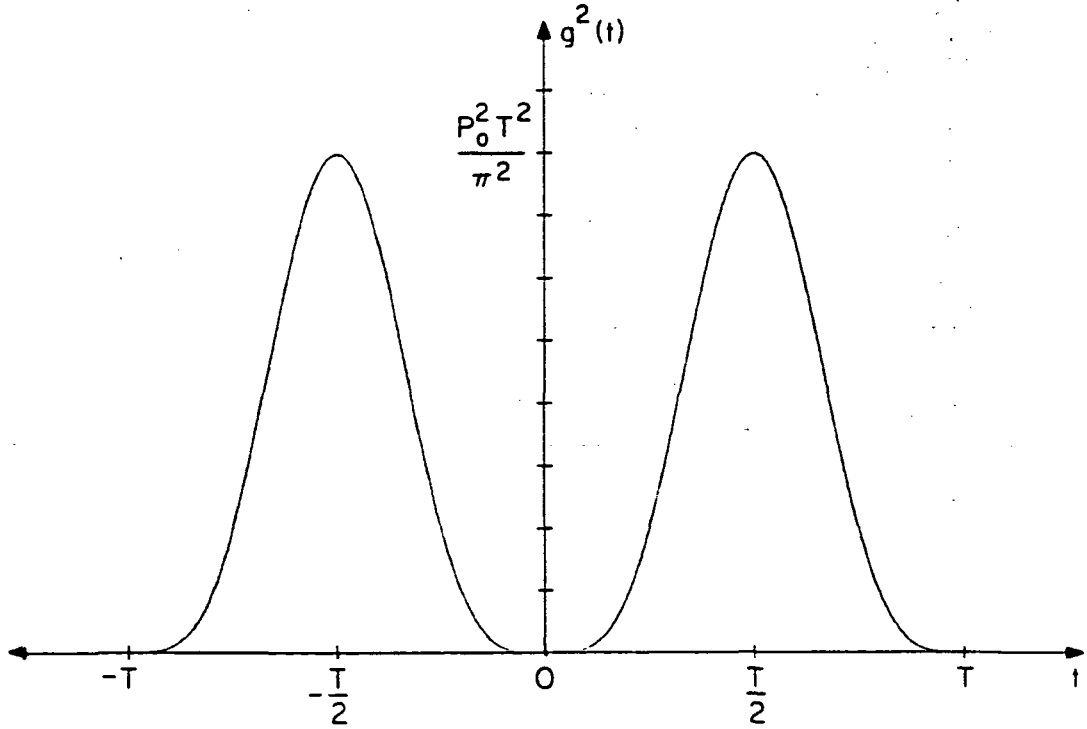

Figure 3.3b. Result of passing g(t) of Figure 3.3a through the squaring loop.

$$a_1 = 2\left(\frac{P_o^2 T^2}{2\pi^2}\right) \quad . \tag{3.15}$$

Averaging (3.15) over the M time slots in a word and substituting $T = T_w/M$ give us an amplitude coefficient of

$$a_1 = \frac{P_o^2 T_w^2}{M^3 \pi^2} \quad . \tag{3.16}$$

So multiplying the PLL input by the attenuation constant, α, defined by

$$\alpha = \frac{1}{a_1} = \frac{M^3 \pi^2}{P_o^2 T_w^2} \quad , \tag{3.17}$$

limits the average PLL input signal to unity. This completes the design and analysis of the receiver timing subsection.

CHAPTER 4

COMMUNICATION SYSTEM LINK

Of importance in any practical communication link is the amount of signal power received. The larger the received signal, the better we can determine the original message and the lower the probability of making an error. In this analysis, we are ultimately interested in the number of photocounts per signal pulse or time slot received by the photodetector. Specifically, we now consider optical transmission between two satellites, one in a geosynchronous orbit and the other in a lower earth orbit.

4.1 Transmitter Design

The purpose of an optical transmitter is to focus as much of the modulated signal power (led or laser) as possible onto the receiving telescope. For a laser transmission system, the transmitter usually consists of a beam expander which is used to reduce the beam divergence. The beam expander may consist of reflecting or refracting optics depending on cost, weight, and wavelength of the source. Figure 4.1 shows two beam expander configurations.

The output of the beam expander can be considered as a uniformly illuminated circular diffracting aperture of diameter d_T. The amplitude distribution of the Fraunhofer (far-field) diffraction pattern is [7]

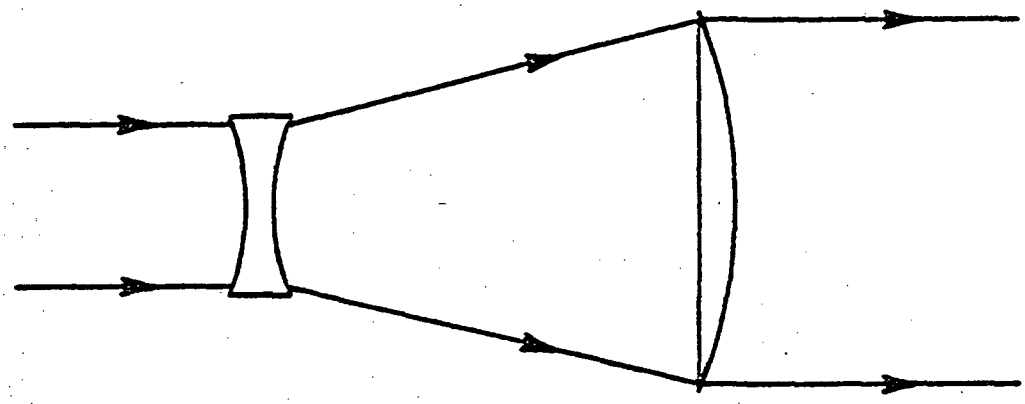

REFRACTING BEAM EXPANDER

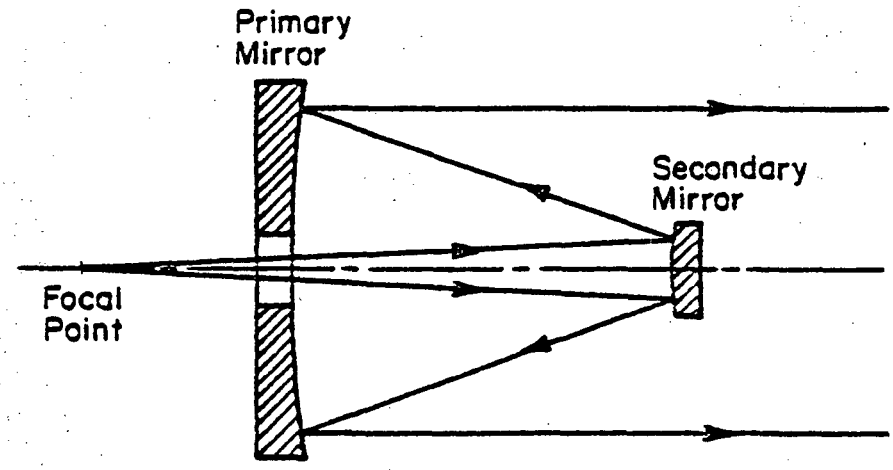

CASSEGRAINIAN TELESCOPE

Figure 4.1. Typical beam expander configurations.

$$U(r_o) = \exp(jkz)\ \exp(jkr_o^2/2z)\ \frac{kd_T^2}{j8z}\left[\frac{2J_1(kd_T r_o/2z)}{kd_T r_o/2z}\right] \tag{4.1}$$

where

r_o = radial coordinate in the far-field plane

d_T = diameter of the transmitting aperture

k = wave number of the source

z = transmission distance

and $J_1(x)$ is a first-order Bessel function. Thus the far-field intensity distribution is

$$I(r_o) = U(r_o)\ U^*(r_o) = \left(\frac{kd_T^2}{8z}\right)^2 \left(\frac{2J_1(kd_T r_o/2z)}{kd_T r_o/2z}\right)^2 I_T \tag{4.2}$$

where I_T is the transmitted intensity. This intensity distribution is commonly known as the Airy pattern and has well-defined zeros wherever the quantity

$$\left[\frac{2J_1(kd_T r_o/2z)}{kd_T r_o/2z}\right] = 0 \quad . \tag{4.3}$$

For large distances, the receiver aperture is small compared to the size of the Airy disk (the circular area contained within the first minimum of (4.3)). Therefore, we make the approximation for an aperture of diameter d_r, centered at a point r_o in the receiving plane, that the total optical power, P_r, intercepted by the aperture is

$$P_r \approx \frac{\pi d_r^2}{4} I(r_o) = A_r\ I(r_o) \tag{4.4}$$

where $A_r = \pi d_r/4$ is the receiver aperture area. Also, assuming uniform

illumination of the transmitting aperture, the transmitter laser power P_L is related to the transmitted intensity by

$$P_L \simeq \frac{\pi d_T^2}{4} I_T = A_T I_T \tag{4.5}$$

where $A_T = \pi d_T/4$ is the transmitter aperture area. Now using (4.2), (4.4), and (4.5), we write

$$P_r = \frac{A_T A_r}{z^2 \lambda^2}\left[\frac{2J_1(\pi d_T r_o/z\lambda)}{\pi d_T r_o/z\lambda}\right]^2 P_L \tag{4.6}$$

where we have used $k=2\pi/\lambda$, where λ is the wavelength of the source.

We now consider optical power losses in the transmitter. First, no optical surface will transmit all of the incident optical power. Compounding this problem is the fact that there is generally more than one lens or mirror, and the combined effects are multiplicative. Second, since the laser cross-section can be mathematically described as a Gaussian beam which is infinite in extent, we must account for truncation of the expanded beam by the finite diameter transmission aperture. Finally, if a Cassegrainian or similar type of reflecting telescope is used, the secondary mirror obstructs the beam and reduces the overall transmissivity of the telescope. In some cases, the secondary mirror mounting supports may also contribute to obscuration of the beam. A detailed analysis of beam truncation and obscuration effects can be found in [8] and [9].

For this analysis, we account for all the transmitter losses by defining a constant, η_T, which is the overall efficiency (transmittance) of the transmitting telescope. Thus, (4.6) becomes

$$P_r = \frac{\eta_T A_r A_T}{z^2 \lambda^2} \left[\frac{2J_1(\pi d_T r_o / 2z)}{\pi d_T r_o / 2z} \right]^2 P_L \quad . \tag{4.7}$$

4.2 Receiver Design

The objective of the optical receiver is to focus the light gathered by the aperture onto a photodetector while rejecting as much background radiation as possible. A typical receiver is shown in Figure 4.2. The field stop iris is used to narrow the field of view of the receiver so radiation from areas adjacent to the transmitter is ignored. The interference filter eliminates wavelengths which are not the same as that of the source. In addition to the optical losses mentioned in Section 4.1, the receiver has the additional loss associated with the interference filter. Narrow band filters have small transmittances whereas wider band filters have higher transmittances. For our analysis, as in the transmitter, we define a constant, η_r, to be the overall receiver efficiency to account for all losses.

The receiver focuses the optical power onto a photodetector such as an avalanche or PIN photodiode. In turn, the incident photons cause the generation of electron-hole pairs which flow to produce current in the device. The detector quantum efficiency, η_d, is defined as

$$\eta_d = \frac{\text{Number of electron hole pairs generated}}{\text{Number of incident photons}} \quad . \tag{4.8}$$

A practical photodiode may have a quantum efficiency of between 30% and 90%. However, a high quantum efficiency requires a thick depletion region of material which results in a slow response time. A fast

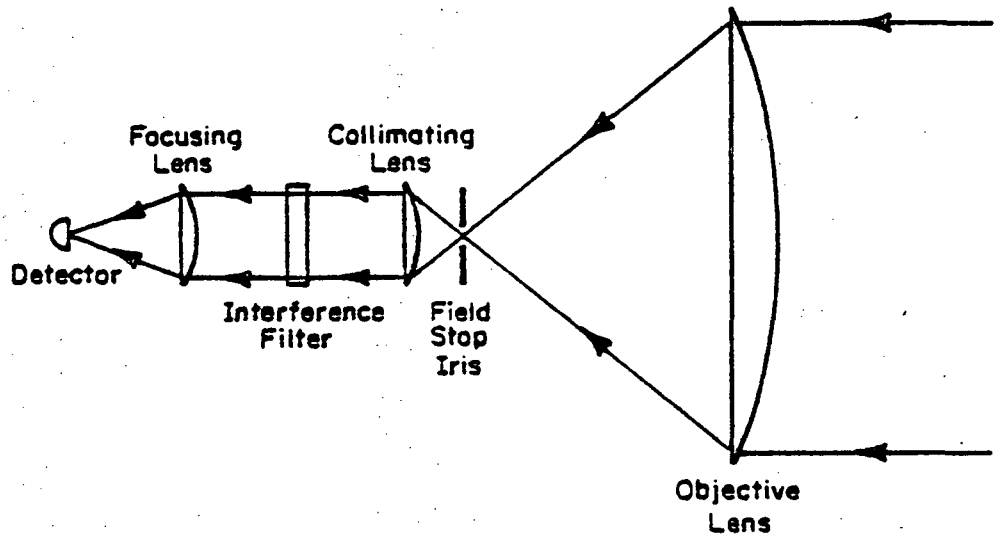

Figure 4.2. Simple direct detection receiver.

response photodiode, necessary for high data rate communication systems, will typically have a much lower quantum efficiency due to the tradeoff between response time and efficiency.

We are interested in determining the number of photocounts per signal pulse generated by the photodiode. Letting D denote the data rate of the signal, we write

$$\langle N \rangle = \frac{\eta_d \eta_r \lambda}{Dhc} P_r \tag{4.9}$$

where

$\langle N \rangle$ = expected number of photocounts per signal pulse

h = Planck's constant

c = speed of light.

Combining (4.9) and (4.7) gives us

$$\langle N \rangle = \frac{\eta_d \eta_r \eta_T A_T A_r}{Dhcz^2 \lambda} \left[\frac{2J_1(\pi d_T r_o / z\lambda)}{\pi d_T r_o / z\lambda} \right]^2 P_L \quad . \tag{4.10}$$

Equation (4.10) is the total link equation for the system. Note that (4.10) is maximized if $r_o = 0$ which corresponds to zero pointing error between the transmitter and receiver. So

$$\langle N \rangle_{max} = \frac{\eta_d \eta_r \eta_T A_T A_r}{Dhcz^2 \lambda} P_L \tag{4.11}$$

is the maximum number of photocounts per signal pulse.

4.3 Background Radiation

For two satellites in an earth orbit, background radiation (noise)

sources include the stars, planets, earth, moon, and sun. Reception with the sun directly in the background is usually not attainable because of its high brightness, and will not be considered here. A useful radiation measurement is the spectral radiant emittance, $W(\lambda)$, which is the radiant power at a wavelength λ emitted into a hemisphere per unit area of source in the hemisphere. Assuming a Lambertian source of diameter d_s at distance z from the receiver, the total amount of background radiation power incident on the detector, P_B, is

$$P_B = \frac{\pi \eta_r \lambda_i d_s^2 d_r^2}{16 z^2} W(\lambda) \tag{4.12}$$

where

η_r = receiver efficiency

d_s = source aperture diameter (m)

d_r = receiver aperture diameter (m)

z = distance between source and receiver (m)

λ_i = interference filter bandwidth (Å).

Equation (4.12) assumes that the whole source is contained in the receiver field of view. If the solid angle of the receiver field of view, Ω_r, is less than the solid angle subtended by the source at the receiver, Ω_s, the background radiation power is given to a good approximation by [10]

$$P_B = \frac{\pi \eta_r \lambda_i d_s^2 d_r^2}{16 z^2} \left(\frac{\Omega_r}{\Omega_s} \right) W(\lambda) \quad . \tag{4.13}$$

The solid angle for the receiver (assuming small angles) is

$$\Omega_r = \frac{\pi \theta_r^2}{4} \tag{4.14}$$

where θ_r is the planar angle of the receiver field of view. Using (4.14), (4.13) and

$$\Omega_s = \frac{\pi d_s^2}{4z^2} \tag{4.15}$$

yields

$$P_B = \frac{\pi \eta_r \lambda_i \theta_r^2 d_r^2}{16} W(\lambda) \tag{4.16}$$

which is the formula for an extended source filling the receiver field of view, as is the case when a satellite is pointed towards the earth for signal reception.

For smaller sources such as stars, it is usually more convenient to make background radiation measurements in terms of the spectral irradiance, $H(\lambda)$, which is the power per unit wavelength interval incident on a unit area of the receiver [10]. Therefore, if a background radiation measurement is given in terms of $H(\lambda)$, then the background radiation power gathered by the receiver is

$$P_B = \frac{\pi \eta_r \lambda_i d_r^2}{4} H(\lambda) \ . \tag{4.17}$$

Of primary concern is the background radiation from the earth due to reflection of the sun. Figure 4.3 shows the spectral radiant emittance of the earth versus wavelength. Note that for the wavelengths of interest (between 0.8 and 0.9 μm), $W(\lambda)$ is near its peak value. As indicated in Figure 4.3, this measurement is valid when there is no cloud cover in the earth's atmosphere. Radiance from sunlit clouds is

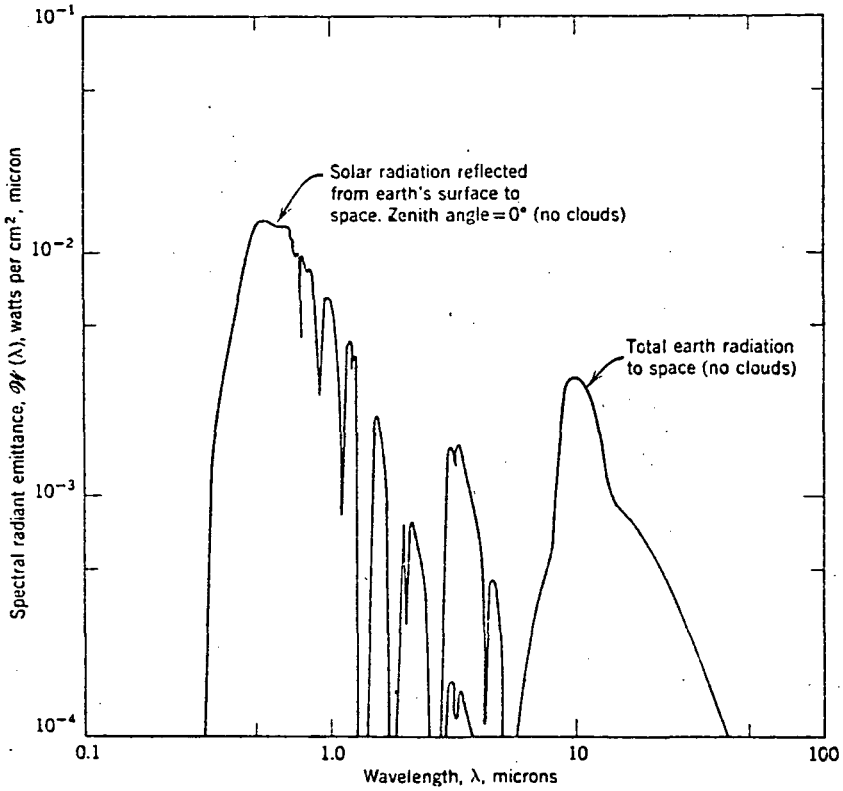

Figure 4.3. Spectral radiant emittance of the earth. (From W. K. Pratt, Laser Communication Systems. New York: John Wiley and Sons, 1968, p. 125.)

approximately one order of magnitude larger and, as we will see in calculations to follow, it represents the strongest, worst case background noise source. Figure 4.4 shows the spectral irradiance for the planets and moon, and Figure 4.5 shows the spectral irradiance for the brighter stars immediately outside the earth's atmosphere. Figures 4.3 and 4.4 show that a full moon exibits the largest background emission next to that of the earth. Because of the close proximity of the satellite to the moon, the use of (4.17) would be incorrect since it assumes the whole source is in the field of view, when actually only a portion of the moon would be in the satellite's field of view. Assuming that the moon appears as a uniformly illuminated Lambertian surface, we have the relation [10]

$$W(\lambda) = \frac{\pi}{\Omega_s} H(\lambda) \quad . \tag{4.18}$$

Substituting (4.18) and (4.15) into (4.16) yields

$$P_B = \frac{\pi \eta_r \lambda_i \theta_r^2 d_r^2 z^2}{4 d_s^2} H(\lambda) \tag{4.19}$$

which is the background power gathered by the receiver when the source fills the field of view and the spectral irradiance is the given measurement parameter. We can convert the background radiation power gathered by the receiver aperture into background counts/time slot output by the detector using

$$\langle N \rangle_B = \frac{\eta_d \lambda}{DhcM} P_B \tag{4.20}$$

where

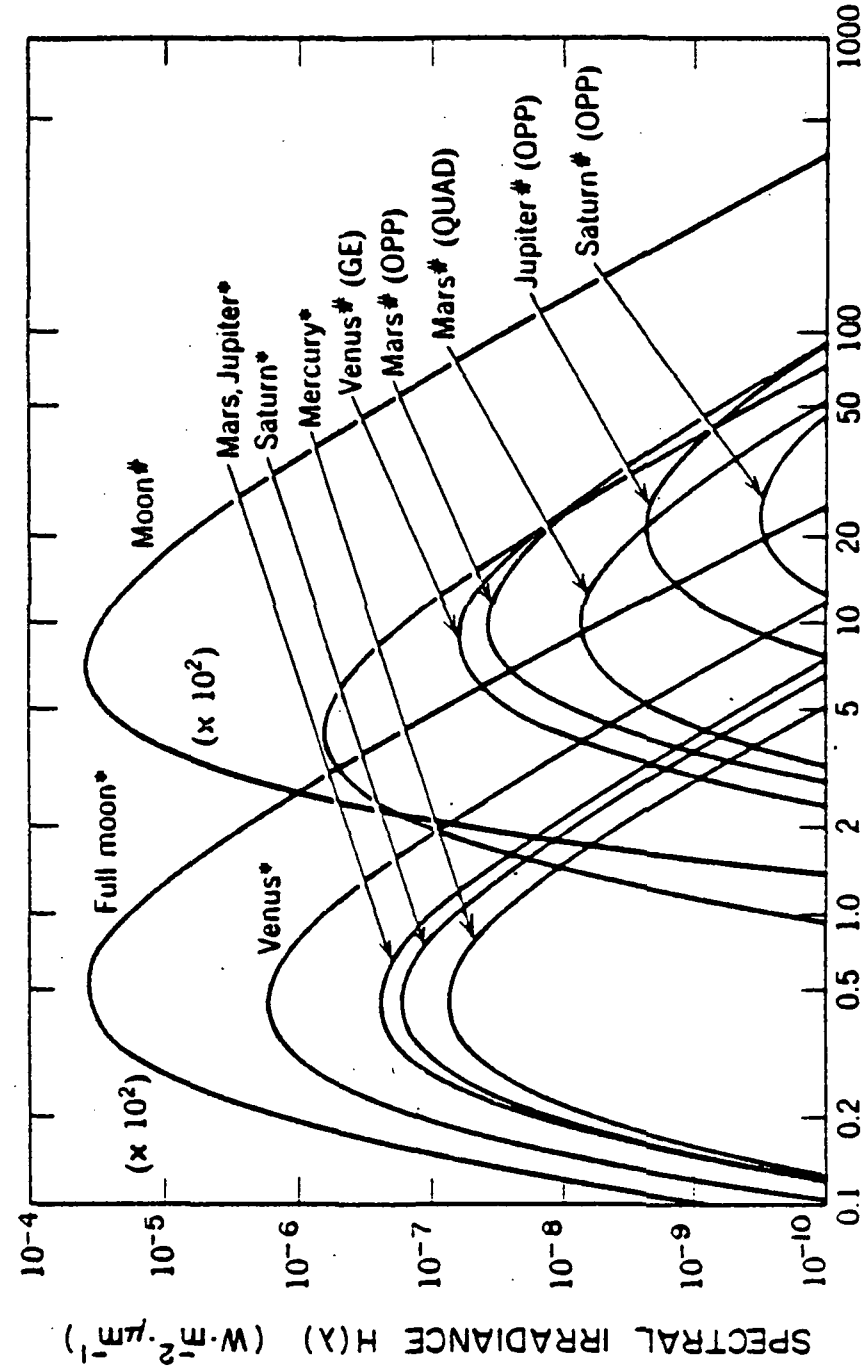

Figure 4.4. Calculated planetary and lunar spectral irradiance outside the terrestrial atmosphere. (From W. K. Pratt, Laser Communication Systems. New York: John Wiley and Sons, 1968, p. 123.)

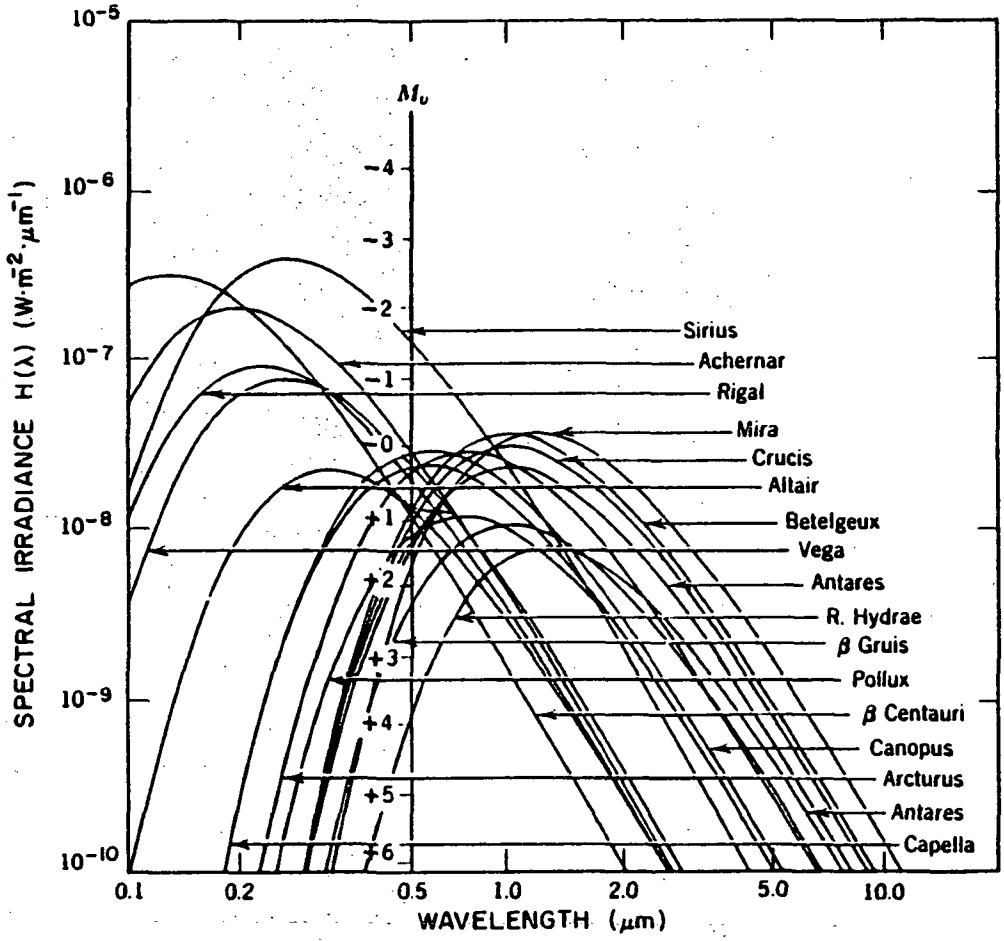

Figure 4.5. Spectral irradiance of brightest stars outside the terrestrial atmosphere. (From W. K. Pratt, Laser Communication Systems. New York: John Wiley Sons, 1968, p. 126.)

$\langle N \rangle_B$ = expected number of background counts/time slot

and

M = number of time slots/word.

4.4 Calculation of Signal and Background Counts

In Sections 4.2 and 4.3 we derived the mathematical relationships governing the amount of signal and noise counts emitted by the photodetector given the signal (laser) and background power present. Now we use some typical component parameters to calculate numerical results.

The following parameter values were chosen for a typical satellite-to-satellite link:

transmission wavelength	$\lambda = 830$ nm
transmitter efficiency	$\eta_T = 0.7$
receiver efficiency	$\eta_r = 0.6$
receiver planar field of view	$\theta_r = 1$ mrad
receiver aperture diameter	$d_r = 0.25$ m
transmitter aperture diameter	$d_T = 0.1$ m
laser power	$P_L = 200$ mW
quantum efficiency	$\eta_d = 10\%$
data rate	$D = 2 \times 10^8$ words/sec
separation length	$z = 3.57 \times 10^7$ m
interference filter bandwidth	$\lambda_i = 20$ Å.

Using the above parameter values in (4.11) yields

$$\langle N \rangle_{max} = 77 \text{ counts/signal pulse.}$$

This is the maximum number of signal counts we can expect under ideal (no pointing error) conditions. Note that pointing error tolerances are severe since the Airy intensity pattern falls away rapidly from the central maximum. In fact, a pointing error of only 5 μrad causes <N> to fall to 29 counts/signal pulse.

Using (4.16) and (4.20) to calculate background counts due to solar radiation reflected from the earth filling the receiver field of view gives

$$\langle N \rangle_B = 3.08/M \text{ counts/time slot (no clouds).}$$

As previously discussed, if extensive cloud cover were present on earth, this value would increase to approximately 30.8/M counts/time slot.

The moon is the other major source of background radiation. Figure 4.4 shows that the spectral irradiance of a full moon is roughly 10^{-3} W/m^2/μm. Substituting this value into (4.19) and (4.20), the maximum number of background counts possible from a full moon is

$$\langle N \rangle_B = 1.52/M \text{ counts/time slot.}$$

This number of counts is attained only if the receiver is pointing directly at a fully illuminated moon. The brightest star with a wavelength larger than 0.5 μm has a spectral irradiance of about 5×10^{-8} W/m^2/μm. Inserting this value into (4.17) and (4.20) results in

$$\langle N \rangle_B = 6.16 \times 10^{-3}/M \text{ counts/time slot/star ,}$$

a value small enough to neglect even from many stars of the same spectral irradiance.

Background counts can also occur by dark counts emitted from the detector. However, dark counts are usually on the order of 10 to 20 counts/sec. With the high data rates under consideration, the dark counts per time slot are extremely small and also negligible.

The above calculations show that the worst possible communication situation is encountered by a satellite in geosynchronous orbit pointed directly towards a cloud-covered section of the earth that is illuminated by the sun. Using 1 to 3 background counts/time slot for the nominal case and 7 to 10 background counts/time slot for the worst case would effectively represent the range of expected operating conditions.

CHAPTER 5

SIMULATION OF THE RECEIVER

The computer simulation of the receiver is comprised of two main parts. The first is the modeling of the photodetector which generates the arrival time records, and the second is the simulation of the PLL.

To generate the arrival time records we follow the procedure described in [11]. We know that the interarrival times of a homogeneous Poisson process with intensity, λ_p, are independent and identically exponentially distributed also with parameter λ_p. Using this property we first generate a sequence of independent and uniformly distributed random variables $u_1, u_2, \ldots, u_i$ on the interval (0,1). Then using the transformation

$$\ell_i = -\ln(u_i) \tag{5.1}$$

a sequence of independent, exponentially distributed random variables of unit parameter is obtained. To generate a homogeneous Poisson process we assign ℓ_1 as the arrival time of the first photon, and then define ℓ_2 as the interarrival time of the second photon and ℓ_k as the interarrival time of the k^{th} photon. Now, the arrival time of the k^{th} photon, x_k, is

$$x_k = \sum_{i=1}^{k} \ell_i \quad . \tag{5.2}$$

Next a random PPM intensity sequence, $\lambda_R(t)$, is created. The final arrival time sequence used in (2.5) is formed by solving

$$x_k = \int_0^{t_k} \lambda_R(z)\, dz \tag{5.3}$$

for the t_k's [11]. Appendix A.1 contains a listing of the Fortran program ARRIVAL used to generate the arrival time record for an M-ary PPM signal using the described method.

The PLL was simulated using the Advanced Continuous Simulation Language (ACSL). This language is designed for modeling and evaluating the performance of continuous systems that are described by time dependent, nonlinear differential equations and transfer functions. ACSL allows direct transformation of the mathematical diagram of Figure 3.2 into a suitable simulation model program. A listing of the ACSL simulation program for the PLL model is in Appendix A.2. This program takes an externally prepared arrival time sequence, processes it through the filter and squaring loop, constructs the shot noise, applies the resulting signal to the PLL, and gathers data on the phase error. The simplicity of ACSL is evident in lines 30-35 of the simulation program. These six lines contain all the model information necessary to implement the PLL. In fact, the filter is completely described on line 33 by the ACSL statement REALPL which implements a simple low-pass filter. The integrating effect of the VCO is contained in line 35 by use of the INTEG statement which performs an integration on the VCO input control voltage. Most of the remaining program is devoted to simulation of the preprocessing components and shot noise construction.

To show the validity of the simulation model, we present results of two simulations: one without signal preprocessing and the second with preprocessing. From the results in Chapter 2, we expect phase-lock behavior only for the preprocessed case due to the presence of the dominating spectral frequency component in the PLL input. Figures 5.1 and 5.2 show the Fourier transforms of the PLL input and VCO output signal when preprocessing is by-passed, and where the frequency scale is normalized to the time slot rate. Note the lack of a dominating frequency in the input spectrum and that the VCO output spectral component occurs below the slot rate at ω_f, the VCO free-running frequency. Figure 5.3 is a plot of $\Delta\omega t$ versus time. Recall that $\Delta\omega t=K_o v_c(t)t$ is the phase change of the VCO due to the control voltage applied to its input. This change, when added with the phase due to the free-running VCO frequency, should equal the phase of the input signal. The frequency difference between the slot rate and ω_f was 0.103 rad/sec, which should equal the slope of Figure 5.3. Instead, Figure 5.3 shows a very random behavior rather than a well-defined slope of 0.1 rad/sec. Clearly with no signal preprocessing, and thus no dominating spectral component, the loop cannot achieve phase lock.

Figures 5.4 and 5.5 display the Fourier transforms of the input and VCO output when preprocessing is used. Again, the frequency scales are normalized to the slot rate. Notice the very strong slot frequency component in the PLL input signal. Now the VCO output spectrum in Figure 5.5 has shifted from its free-running frequency to match the PLL input signal frequency component at the slot rate. The plot of $\Delta\omega t$ versus time of Figure 5.6 now has the desired slope of 0.1 rad/sec.

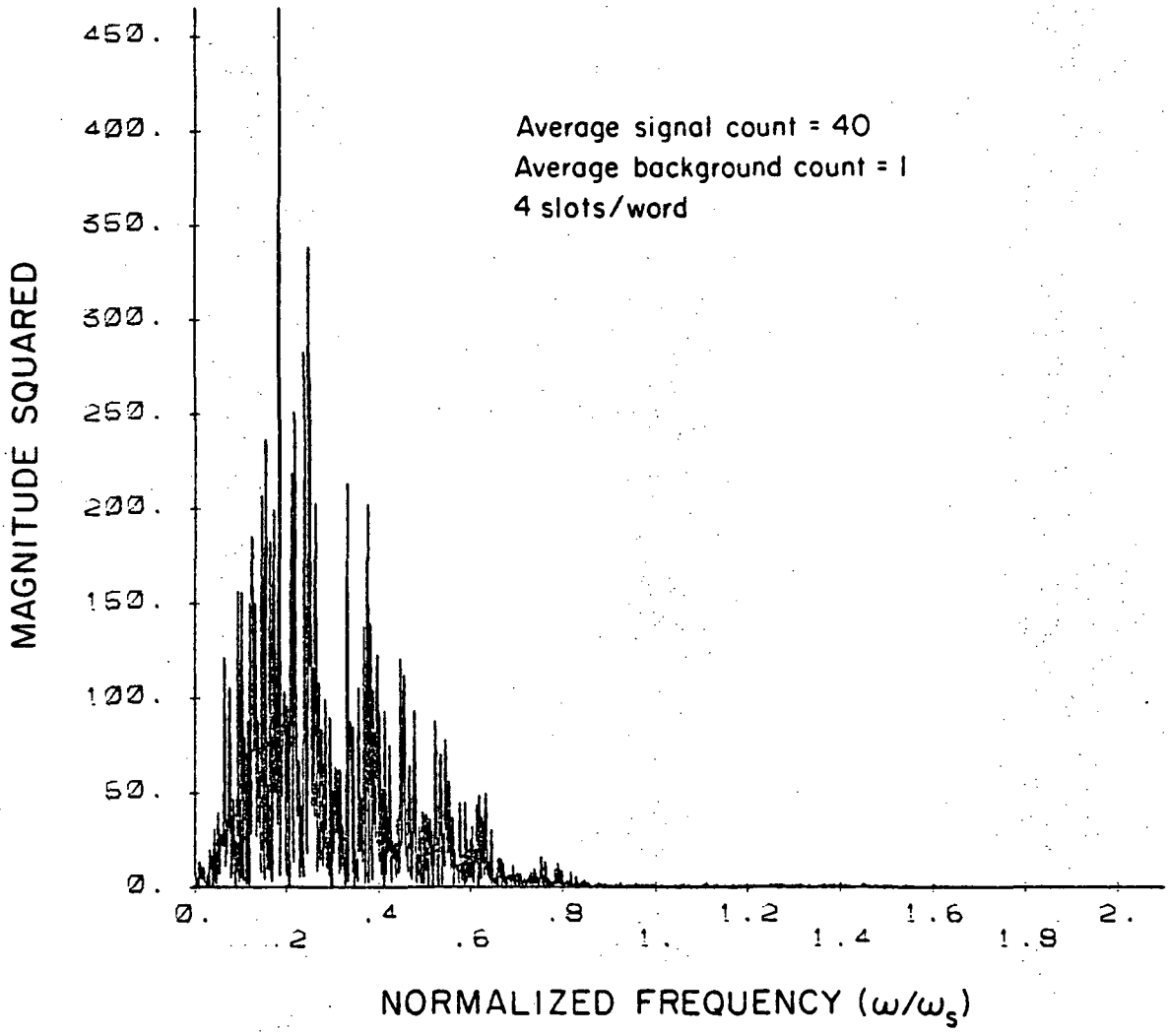

Figure 5.1. Phase-locked loop input signal frequency spectrum when no preprocessing is used. Note the lack of a dominating frequency component.

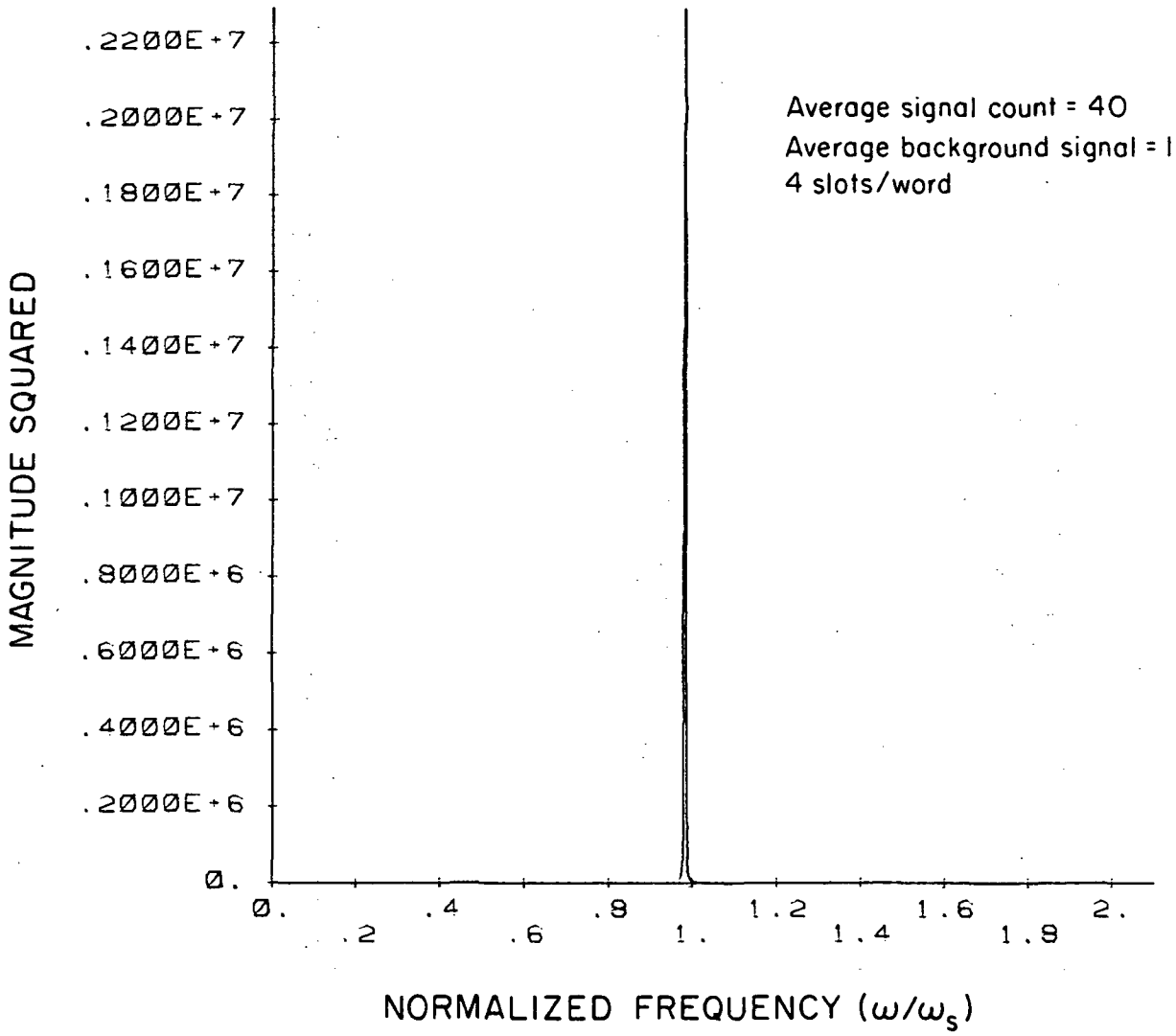

Figure 5.2. VCO output frequency spectrum when no signal preprocessing is used. Note that the dominating frequency component occurs below the slot rate at the VCO free running frequency.

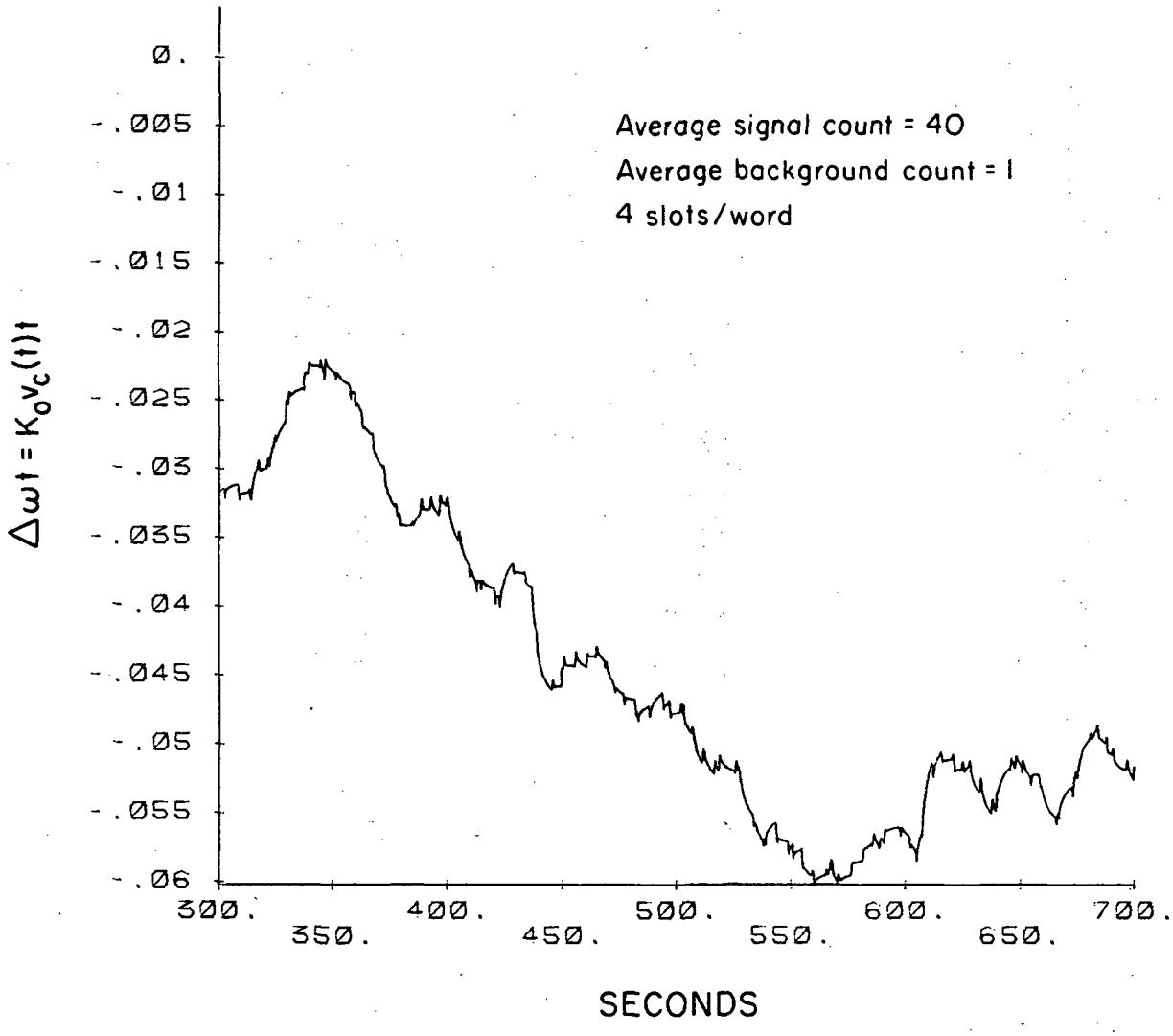

Figure 5.3. $\Delta\omega t$ versus time when no preprocessing is used. The random behavior indicates a lack of tracking.

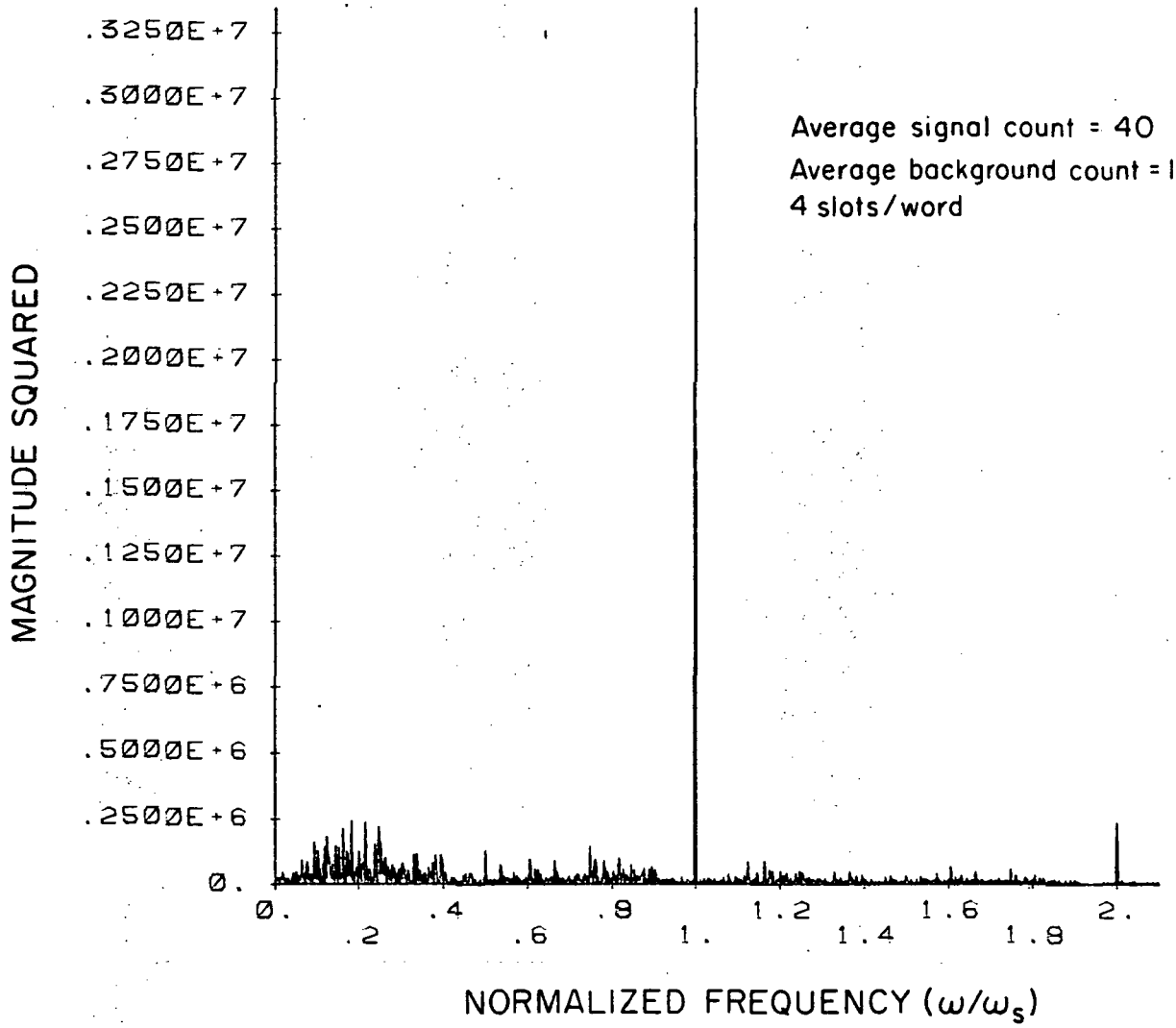

Figure 5.4. Phase-locked loop input signal frequency spectrum when preprocessing is used. The dominating spectral component occurs at the slot frequency.

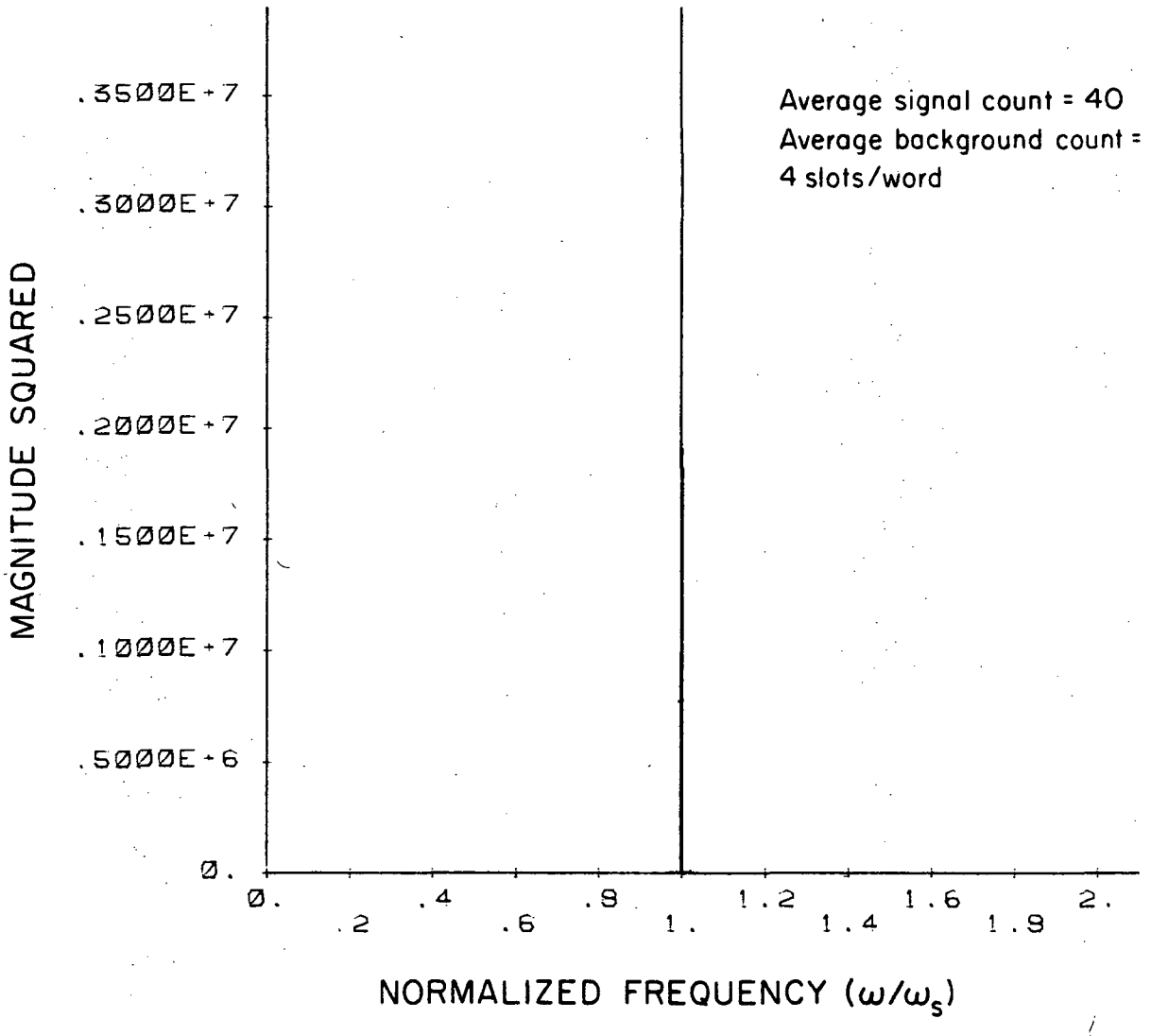

Figure 5.5. VCO output spectrum when preprocessing is used. Note that the spectral component has shifted up to the slot frequency from its free running frequency.

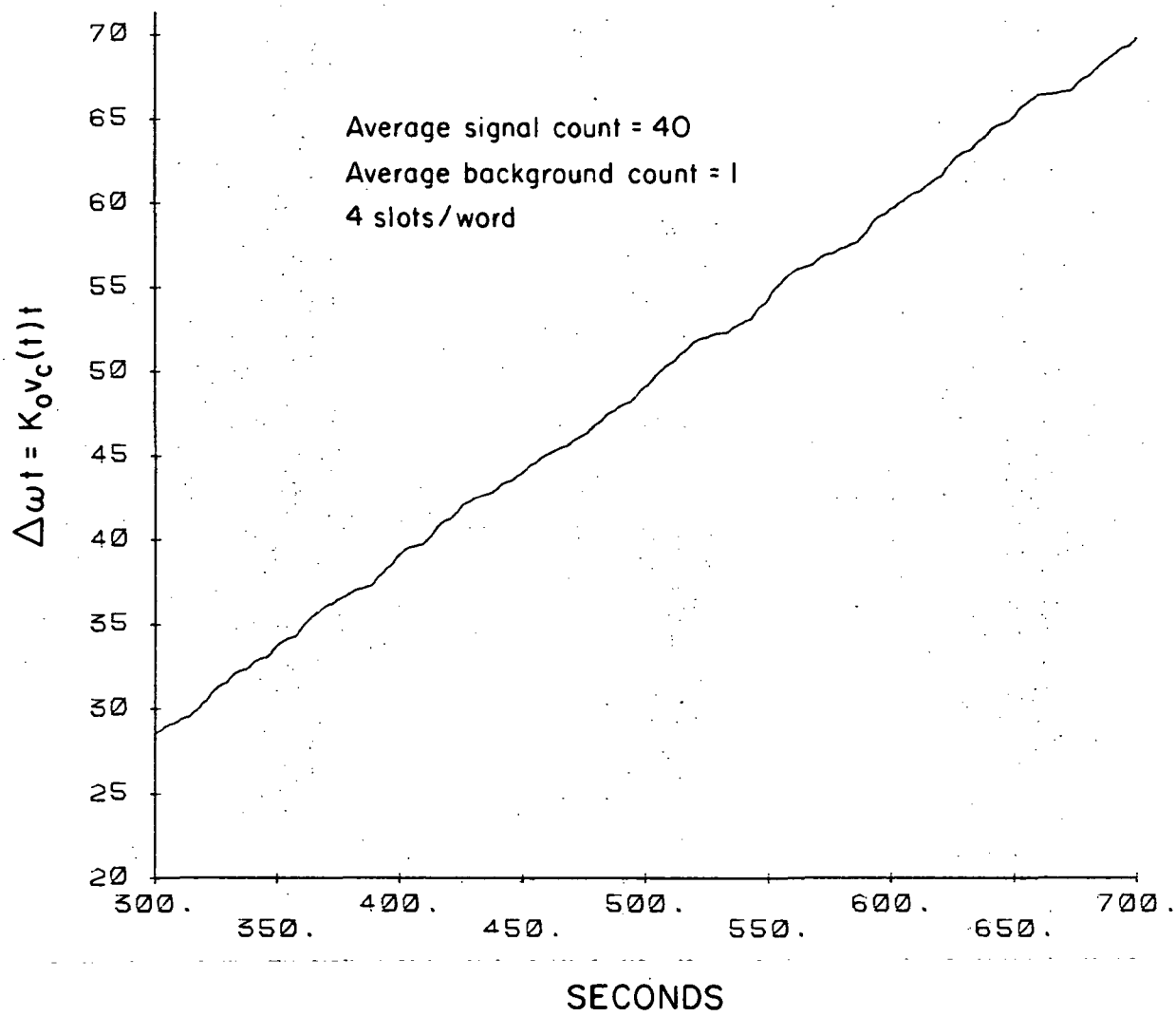

Figure 5.6. $\Delta\omega t$ versus time when preprocessing is used. Note the slope of approximately 0.1 rad/sec indicates tracking performance of the phase-locked loop.

These results indicate that the loop is in lock and is tracking the input frequency.

CHAPTER 6

COMPUTER SIMULATION RESULTS

Computer simulation of the timing subsystem was conducted under varying signal and background strengths to represent a wide range of operating conditions. In this chapter we present the simulation results and compare them to a current theoretical expression.

6.1 Simulation Performance Parameters

The parameter of interest is the phase error, $\phi(t)$, defined as

$$\phi(t) = \theta_s(t) - \theta_o(t) \tag{6.1}$$

where, again, $\theta_s(t)$ and $\theta_o(t)$ are the PLL input and VCO output signal phases, respectively. Once the loop is in lock, we expect the phase error to vary about some constant value. Assuming $\phi(t)$ is approximately Gaussian, the best system performance indicator of the PLL is the RMS phase error, σ_ϕ(rad).

Derivation of an exact expression for σ_ϕ is lengthy and difficult. However, C. Chen has formulated the following approximation of σ_ϕ for the receiver timing subsystem presented above. From [12],

$$\sigma_\phi = \left(\frac{1}{K_s}\right)^{1/2}\left[\frac{2M\pi^4}{T_s}\right]^{1/2}\left[\frac{1}{2\pi}\int_{-\infty}^{\infty}|H_L(\omega)|^2\,dw\right]^{1/2} \tag{6.2}$$

$$\times\left[\frac{1}{4\pi^2}\int_{-\infty}^{\infty}P(\omega')\,P^*(\omega'')\,P^*(\omega'-\omega'')\,H(\omega')\,H(\omega-\omega')\,H^*(\omega-\omega'')\,H^*(\omega'')\,d\omega'\,d\omega''\right]^{1/2}$$

where

K_s = expected signal count

$H_L(\omega)$ = closed-loop frequency response of the PLL

$P(\omega)$ = Fourier transform of received pulse shape

$H(\omega)$ = frequency response of the detector and linear filter

M = number of time slots/word

T_s = slot width.

An important feature of (6.2) is that σ_ϕ is inversely proportional to the square root of the average signal count, K_s. This important property provides a convenient means of comparing the theory to the actual simulation behavior in the next section.

6.2 Numerical Results

A total of 26 computer simulations were completed under varying signal and background count conditions for both 4 slot and 8 slot PPM signals. The following is a summary of system parameters used in the trials:

time slot width	T_s = 1 sec
time slot rate	ω_s = 2π rad/sec
free running frequency	ω_f = 6.18 rad/sec
phase detector gain	K_d = 0.3333 V/rad

VCO gain constant	K_o = 1 rad/sec/V
loop filter bandwidth	$1/\tau$ = 0.3333 rad/sec.

Each trial represents an 8000 sec operation time, corresponding to 2000 data words (4000 bits) for 4 slot PPM and 1000 data words (3000 bits) for 8 slot PPM. The phase error was calculated at the beginning of each time slot, and these values were used to calculate the RMS phase error over the simulation time. Plots of σ_ϕ versus time for each trial appear in Appendix B. Notice as the average background count, K_b, increases and the average signal count, K_s, decreases, the RMS phase error increases and exhibits progressively erratic behavior.

The σ_ϕ versus time plots of Appendix B are summarized in Table 6.1. Table 6.1 lists K_b, K_s, σ_ϕ, as well as the average signal count/bit, K_{bit}, so 4 and 8 slot PPM formats can be correctly compared at the bit level. On a signal count/bit comparision, 8 slot PPM has a higher σ_ϕ (and thus inferior performance) than 4 slot PPM with the same K_{bit} and K_b. Figure 6.1 shows that the difference in performance increases as K_{bit} increases. Also, two of the simulation trials for 8 slot PPM (K_s=45, K_b=5, and K_s=90, K_b=20) exhibited cycle-slipping behavior, indicating that 8 slot PPM may be more sensitive to input signal variations.

Figure 6.2 is a log-log plot of σ_ϕ versus average signal count for 4 slot PPM and a constant K_b of 1, 5, and 10, respectively. Figure 6.3 is a similar plot for 8 slot PPM with K_b=5 only. As indicated in Section 6.1, we expect σ_ϕ to be inversely proportional to the square root of K_s, corresponding to an ideal slope of -0.5 in Figures 6.2 and 6.3. Each of the lines drawn in Figures 6.2 and 6.3 represents a least

TABLE 6.1

NUMERICAL RESULTS OF SIMULATION TRIALS

Average Signal Count K_s	Average Signal Count/Bit K_{bit}	PPM Signaling Order M	Average Background Count K_b	RMS Phase Error σ_ϕ (rad)
30	15	4	1	0.2926
30	15	4	5	0.3399
40	20	4	1	0.2609
40	20	4	5	0.2737
40	20	4	10	0.3146
50	25	4	1	0.2496
50	25	4	5	0.2303
50	25	4	10	0.2572
60	30	4	0	0.2181
60	30	4	1	0.2235
60	30	4	5	0.2239
60	30	4	10	0.2402
60	30	4	20	0.2594
80	40	4	1	0.1974
80	40	4	5	0.1857
80	40	4	10	0.2070
45	15	8	5	0.4257
60	20	8	5	0.3573
75	25	8	5	0.3234
80	26.67	8	5	0.3217
90	30	8	0	0.2990
90	30	8	1	0.2978
90	30	8	5	0.3029
90	30	8	10	0.3053
90	30	8	20	0.3823
120	40	8	5	0.2805

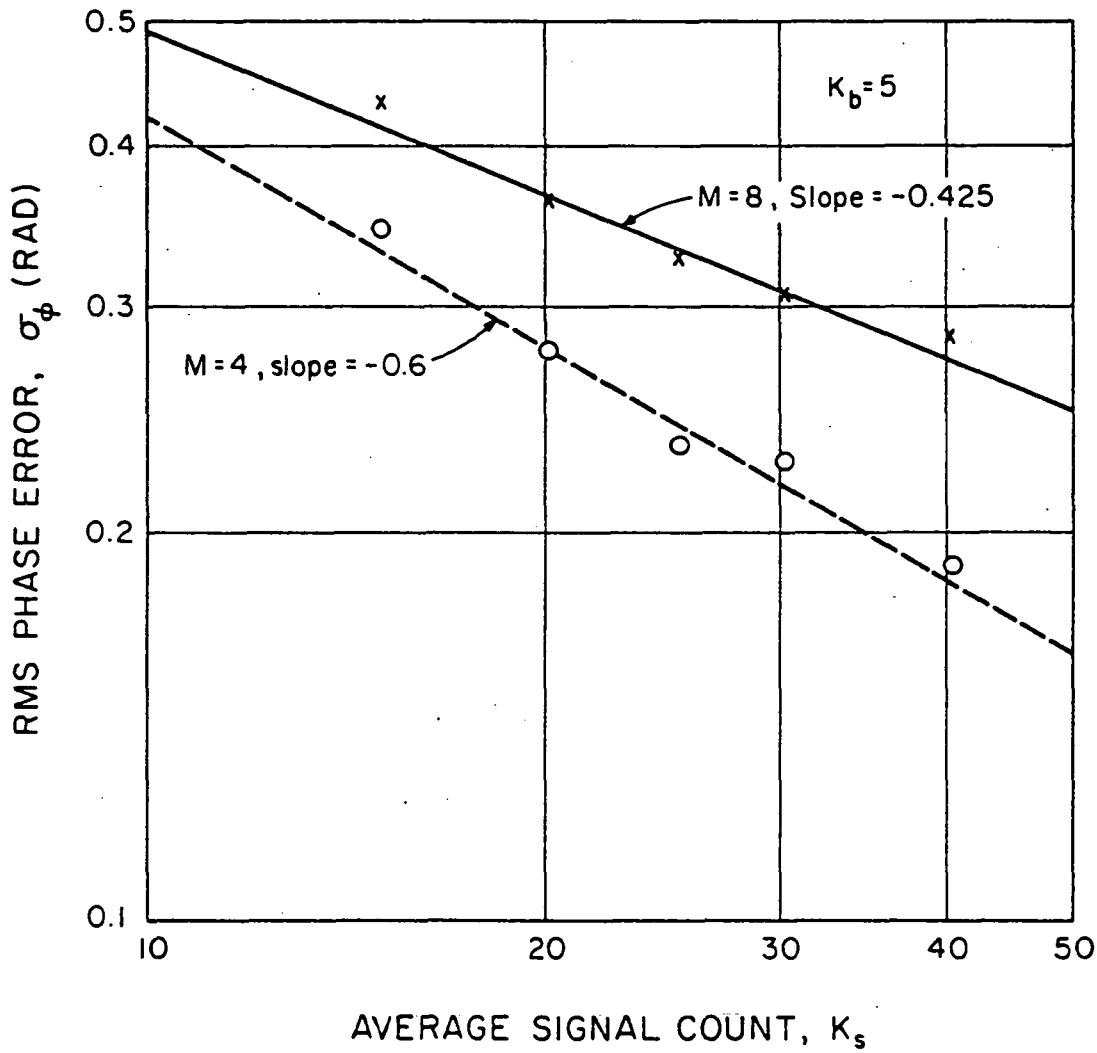

Figure 6.1. RMS phase error versus average signal count/bit for M = 4 and M = 8.

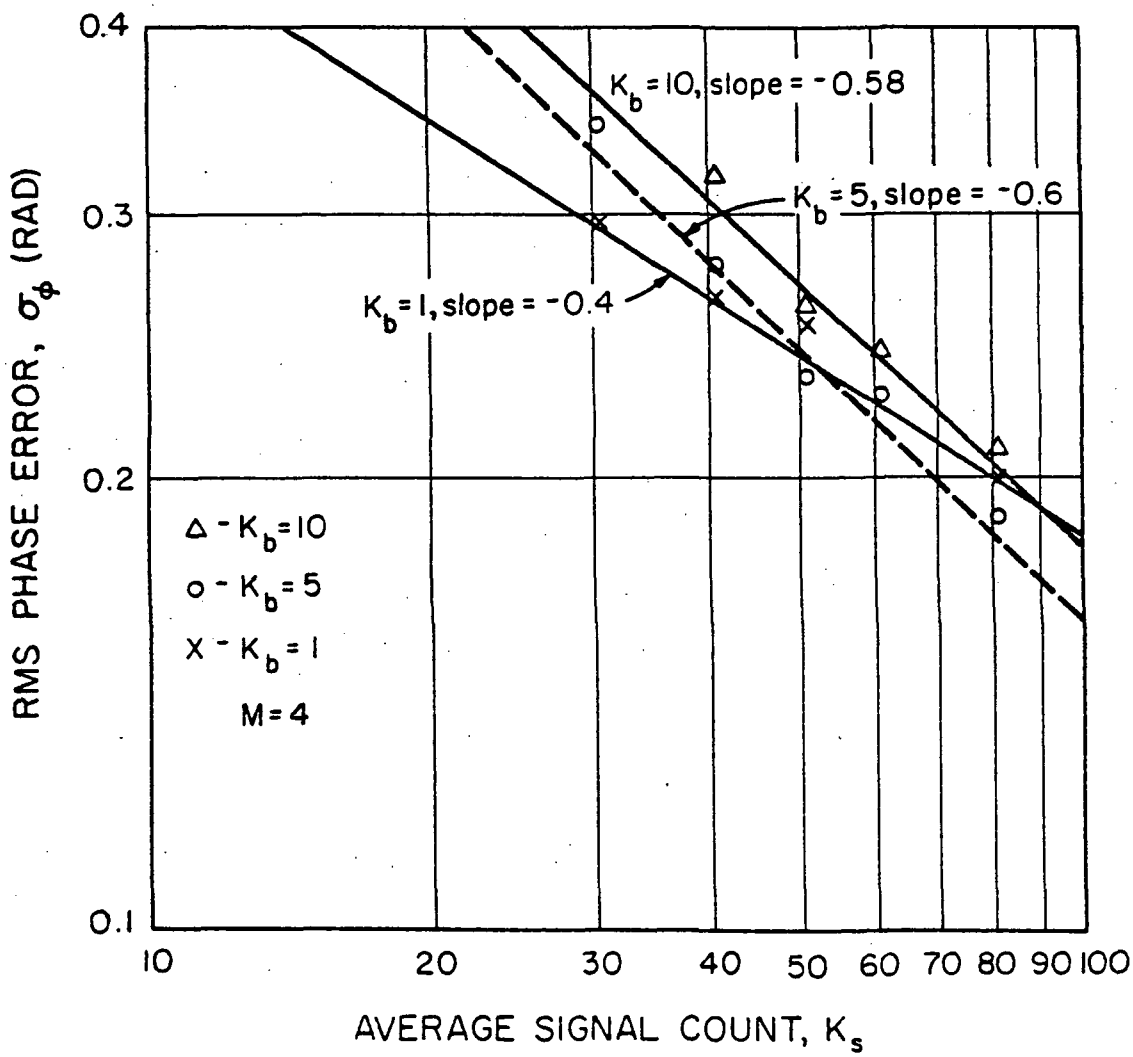

Figure 6.2. RMS phase error versus average signal count for M = 4.

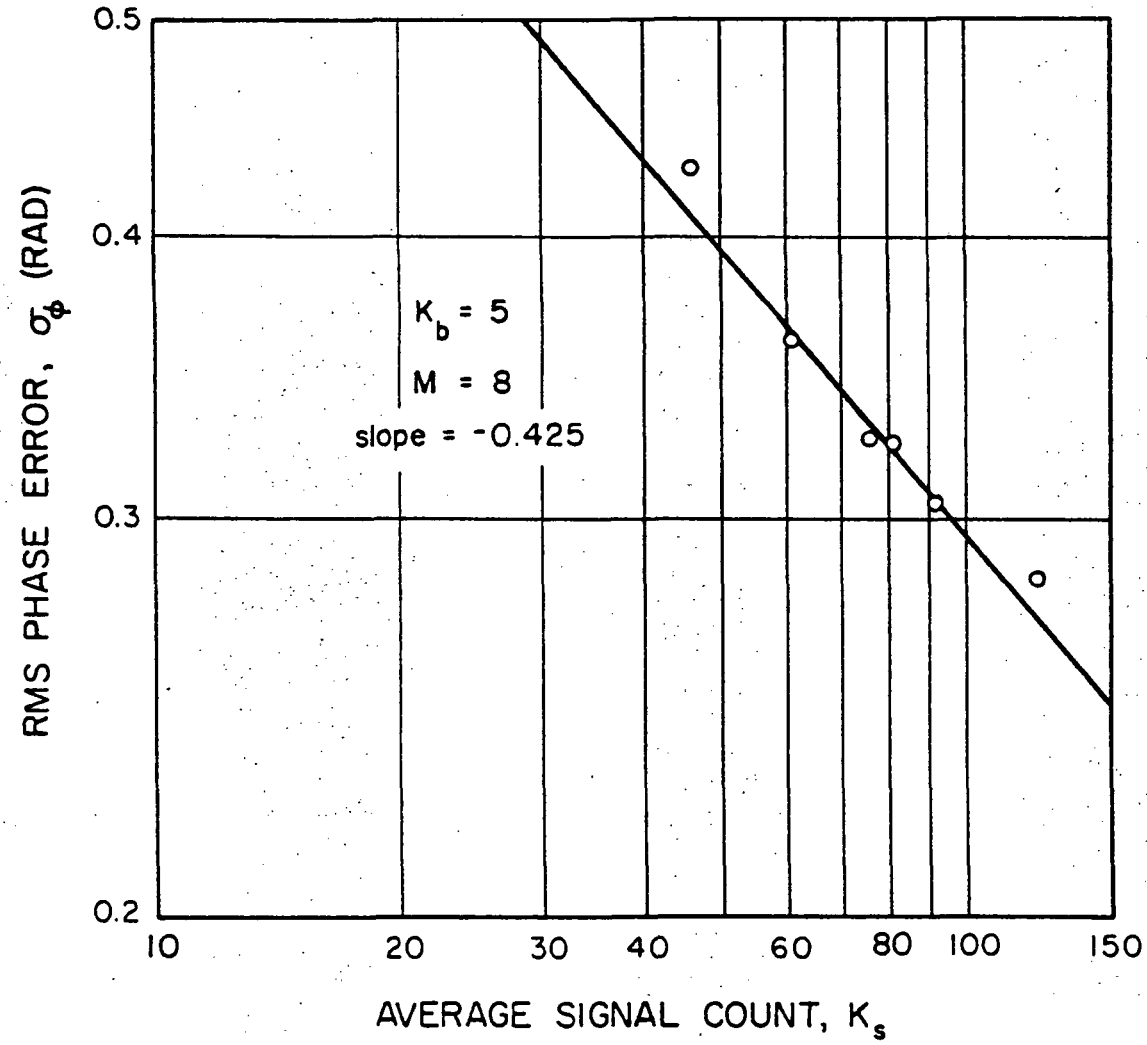

Figure 6.3. RMS phase error versus average signal count for M = 8.

squares fit of data points with respect to a constant value of K_b. In Figure 6.2 the slopes for 4 slot PPM trials are: -0.40 for K_b=1, -0.60 for K_b=5, and -0.58 for K_b=10. For 8 slot PPM trials in Figure 6.3, the slope was -0.425 for K_b=5. These results compare favorably to the ideal slope of -0.5 predicted by (6.2). Currently, a factor of between three and four separates the theoretical and simulation values. It is reemphasized that (6.2) is an approximation, not an exact expresssion. The exact expression for σ_ϕ is unwieldy and difficult to evaluate. Efforts are continuing to obtain a more accurate approximation of the exact expression for σ_ϕ [12].

Figure 6.4 shows the relationship, for 4 slot PPM, between σ_ϕ and K_b when K_s is held constant to 40, 50, 60, and 80 average signal counts. Figure 6.5 is a similar plot for 8 slot PPM for K_s=90 only. In all cases, the relationship between the RMS phase error and background count is not a simple one. For lower background counts, the RMS phase error rises moderately with increasing K_b. As the background count continues to increase, the RMS phase error rises sharply at about K_b=5, indicating a rapid deterioration of timing performance.

The ratio between the timing offset, ΔT, and the time slot width, T_s, called the time slot error (TSE), is related to the RMS phase error by

$$TSE = \frac{\Delta T}{T_s} = \frac{\sigma_\phi}{2\pi} \quad . \tag{6.3}$$

An increasing TSE indicates receiver timing degradation and an increasing probability of bit error, PBE. In fact, the advantages

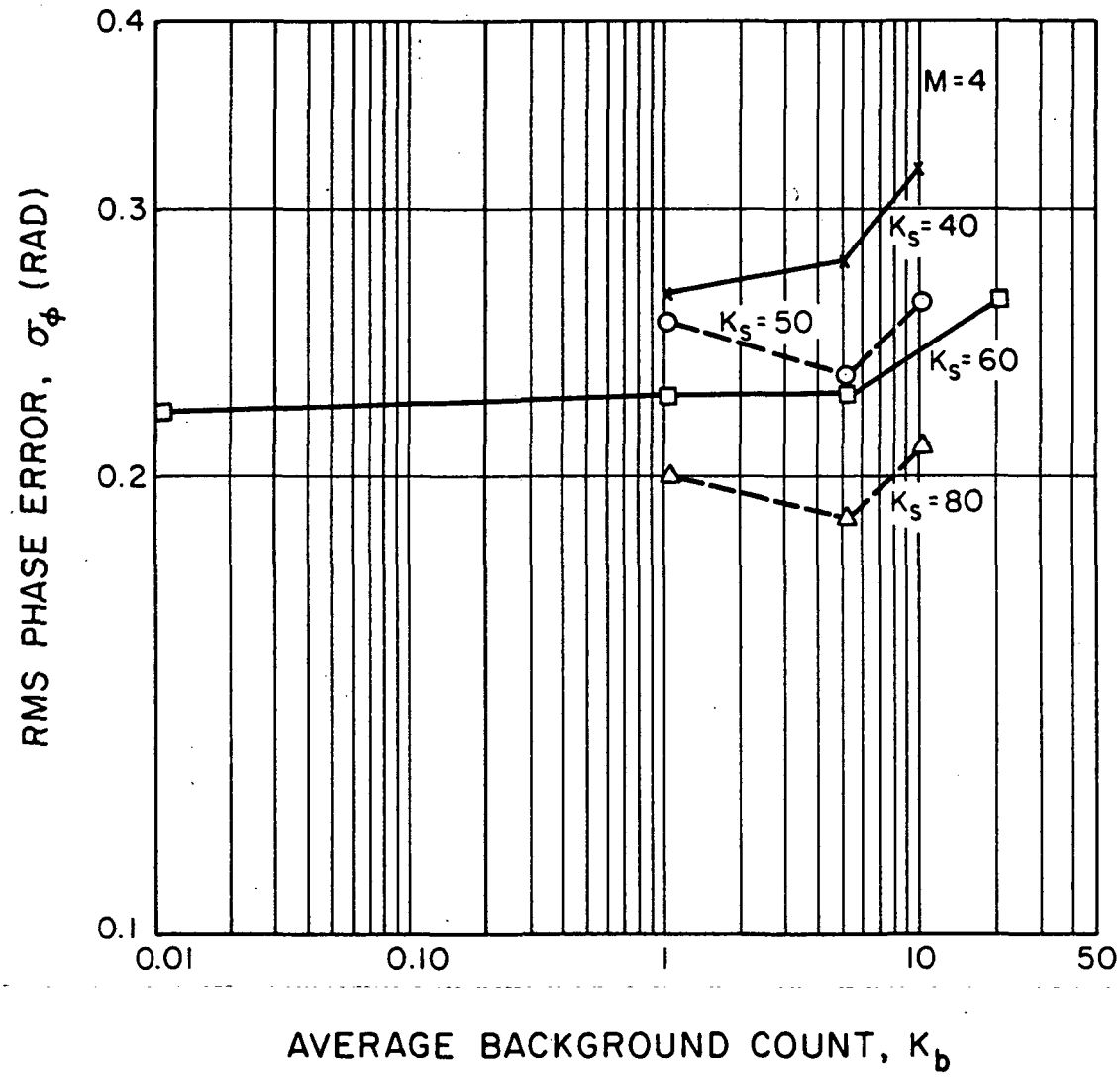

Figure 6.4. RMS phase error versus average background count for M = 4.

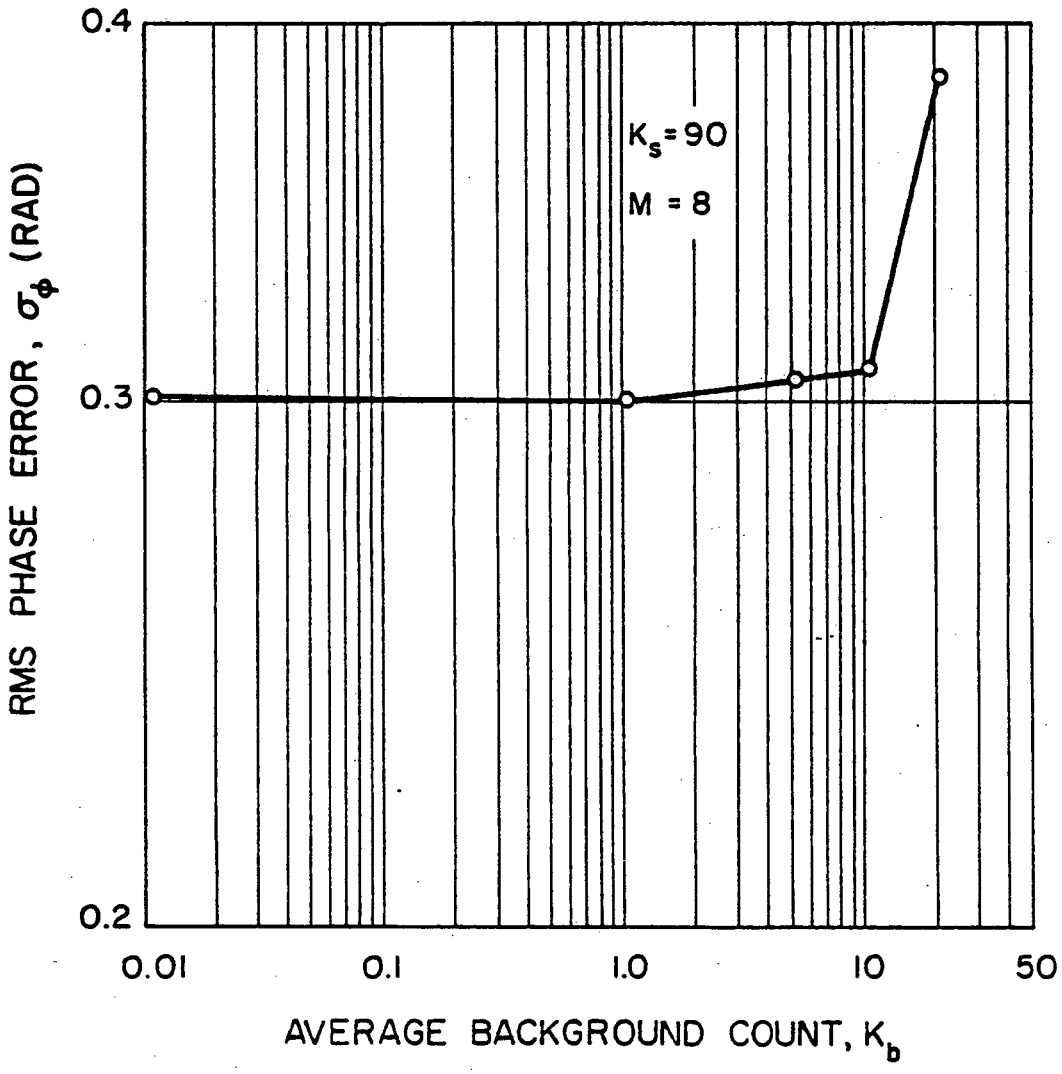

Figure 6.5. RMS phase error versus average background count for M = 8.

gained in block coding (when the probability of word error (PWE) is converted to PBE at normalized rates) are almost eliminated as the timing error (or TSE) increases [4]. As a typical example, consider the 4 slot simulation run of K_s=60 and K_b=1 of Table 6.1. The RMS phase error is 0.2235 rad/sec, corresponding to a TSE of 0.0356. This indicates the receiver timing is off by 3.56%. The 8 slot simulation trial of K_s=90 and K_b=1 has a RMS phase error of 0.2978 rad/sec and a TSE of 0.0474, corresponding to a 4.74% timing error. Detailed discussion and analysis of timing error effects on optical PPM communication systems can be found in [1] and [4].

This concludes the numerical results of the computer simulation data.

CHAPTER 7

CONCLUSION

In this report we have investigated the timing performance of a phase-locked loop (PLL) in an optical pulse position modulation (PPM) communication system. It was shown that the output from a photodetector alone contains no dominating spectral frequency component and is insufficient as a signal source for the PLL. A simple filter and squaring loop was shown to generate a strong spectral component at the slot frequency. Preprocessing the signal in this manner enables the PLL to lock up, track the signal, and provide timing information to the receiver decision section.

We have discussed various PLL design considerations. Once design parameters are fixed, a change in the input signal magnitude can alter the PLL performance. To alleviate this problem, an expression for an attenuation constant was derived which would limit the average PLL input signal to unity, allowing the intended design parameters to remain unchanged over a wide range of signal inputs.

A general satellite-to-satellite link equation was derived to calculate the average number of signal counts emitted by the receiver detector. Average signal count depends on many factors, including physical component values (aperture size, wavelength, etc.), data rate, and pointing error. Sources of background radiation such as the moon,

stars, and earth were examined and it was shown that a cloudy, illuminated section of the earth results in the largest amount of background radiation at the receiver. Typical component values for the link were chosen, and average signal and background counts calculated.

Finally, the entire timing subsystem was simulated on a digital computer and the RMS phase error of the PLL was calculated. The simulations showed the RMS phase error is (approximately) inversely proportional to the square root of the average signal count for both 4 slot and 8 slot PPM signals. This agrees with a theoretical expression recently derived for this timing subsystem which predicts an exact inverse relationship between the RMS phase error and the square root of the average signal count.

APPENDIX A

PROGRAM LISTINGS

A.1 Arrival

```
      PROGRAM ARRIVAL
C
C       THIS PROGRAM CONSTRUCTS THE PHOTON ARRIVAL
C       TIMES FOR A M-ARY PPM DATA SEQUENCE DETECTED
C       BY A PHOTODETECTOR.
C       PULSHI=AMPLITUDE OF SIGNAL PULSE
C       NSLOT=ORDER OF THE PPM SIGNAL
C       TMAX=LENGTH OF RECORD DESIRED IN SECONDS
C       DARK=BACKROUND RADIATION PER PULSE
C       TSLOT=DURATION OF A SINGLE PULSE
C
        DIMENSION ARIVAL(1024)
        INTEGER ISLOT(25)
        DATA NSLOT/4/,TMAX/9000.0/
        DATA PULSHI/40./,DARK/10./,TSLOT/1.0/
        AREA = 0.0
        TNOW = 0.0
        TIMLST = 0.0
        CALL RANSET(31)
        DO 10 I=1,10
   10           U = RANF()
        CALL DATGEN(ISLOT,NSLOT)
        KK = 1
  100   CALL POISSN(ARIVAL,TIMLST,1024,1.0)
        DO 200 I = 1,1024
  170           DIFF1 = (ISLOT(KK) * PULSHI + DARK) * TSLOT
                DIFF2 = ARIVAL(I) - AREA
                IF (DIFF2 .LE. DIFF1) GO TO 180
                KK = KK+1
                TNOW = TNOW + TSLOT
                AREA = AREA + DIFF1
                IF (KK.LE.NSLOT) GO TO 170
                CALL DATGEN(ISLOT,NSLOT)
                KK = 1
                GO TO 170
  180           ARIVAL(I) = TNOW + DIFF2/DIFF1
  200   CONTINUE
        WRITE(3) (ARIVAL(IW),IW=1,1024)
        IF (TNOW .LT. TMAX) GO TO 100
        RETURN
        END
C
C
```

```
44 C
45          SUBROUTINE POISSN(ARIVAL,TIMLST,NUMTRY,PARAM)
46 C
47 C        SUBROUTINE POISSN GENERATES THE POISSON INPUT
48 C        SEQUENCE OF UNIT PARAMETER USING UNIFORM
49 C        RANDOM VARIABLES.
50 C
51          DIMENSION ARIVAL(1)
52 1        UNIF = RANF()
53          IF (UNIF.EQ.0.0) GO TO 1
54          ARIVAL(1) = TIMLST - (ALOG(UNIF)/PARAM)
55          DO 10 J=2,NUMTRY
56 12               UNIF = RANF()
57                  IF (UNIF.EQ.0.0) GO TO 12
58                  ARIVAL(J) = ARIVAL(J-1) - (ALOG(UNIF)/PARAM)
59 10       CONTINUE
60          TIMLST = ARIVAL(NUMTRY)
61          RETURN
62          END
63 C
64 C
65          SUBROUTINE DATGEN(ISLOT,NSLOT)
66 C
67 C        SUBROUTINE DATGEN GENERATES THE RANDOM
68 C        SIMULATED PPM DATA SEQUENCE.
69 C
70          INTEGER ISLOT(1)
71          INTEGER MASK,IRAND
72          MASK = NSLOT
73          DO 10 I=1,NSLOT
74 10             ISLOT(I) = 0
75          IRAND = IFIX(RANF() * 1000)
76          IRAND = MOD(IRAND,MASK)
77          ISLOT(IRAND+1) = 1
78          RETURN
79          END
```

A.2 Simulation of a Phased-Locked Loop

```
 1 PROGRAM SIMULATION OF A PHASE-LOCKED LOOP
 2         "THIS PROGRAM IS DONE IN THE ADVANCED"
 3         "CONTINUOUS SIMULATION LANGUAGE (ACSL)"
 4         " "
 5         INTEGER INDEX
 6         REAL W0,KV
 7         REAL ARIVAL(2049)
 8         CONSTANT THETA = 0.,KV =.3333,...
 9             FIC2 = 0.0,          ...
10             PHI0 =  0.0,W0 = 6.18, ...
11 INITIAL
12         CINTERVAL CINT = 0.125
13         NSTEPS   NSTEP = 3
14         IALG = 4
15         INDEX = 1
16         ENDTIM = 8050.0
17         PROCEDURAL (ARIVAL=ARIVAL)
18         CALL SETVAL(ARIVAL)
19       END $"OF PROCEDURAL"
20 END $ " OF INITIAL "
21         " "
22 DYNAMIC
23     DERIVATIVE $"THIS SECTION CONTAINS THE PLL"
24                  "SIMULATION MODEL EQUATIONS."
25
26         " "
27         PROCEDURAL (SHOT=T,ARIVAL,INDEX)
28             CALL SHOTNZ(T,ARIVAL,INDEX,SHOT)
29         END$ " OF PROCEDURE "
30         PHASE = W0*T+PHI+THETA
31         COPHAS=COS(PHASE)
32         MIXOUT = SHOT*COS(PHASE)
33         FILOUT = REALPL(3.,MIXOUT,0.0)
34         PHIDOT = KV*FILOUT
35         PHI    = INTEG(PHIDOT,PHI0)
36         TERMT(T.GE.ENDTIM)
37     END $ " OF DERIVATIVE "
38         WRITE(1) PHASE  $ "SAVES THE VCO OUTPUT PHASE FOR ANALYSIS"
39 END $ " OF DYNAMIC SECTION "
40 END $ " OF PROGRAM "
41
42
```

```
43          SUBROUTINE SETVAL(ARIVAL)
44 C
45 C        SETVAL READS IN THE FIRST TWO BLOCKS (2048 VALUES) OF
46 C        THE ARRIVAL TIMES FROM THE EXTERNALLY PREPARED ARRIVAL
47 C        TAPE.
48 C
49          REAL ARIVAL(2049)
50                READ(3) (ARIVAL(J),J=1,1024)
51                READ(3) (ARIVAL(J),J=1025,2048)
52           RETURN
53           END
54
55
56
57           SUBROUTINE SHOTNZ(T,ARIVAL,INDEX,SHOT)
58 C
59 C        SUBROUTINE SHOTNZ EVALUATES THE SHOTNZ SIGNAL
60 C        FOR INPUT TO THE PLL AT A GIVEN TIME T.  SHOTNZ
61 C        RETURNS THE CURRENT VALUE IN THE PARAMETER SHOT.
62 C
63 C
64          REAL ARIVAL(2048)
65          INTEGER INDEX
66          Q=T+10
67 10       IF (ARIVAL(INDEX).GE.Q) GO TO 100
68                INDEX = INDEX + 1
69                IF (INDEX.LT.2049) GO TO 10
70                DO 20 I=1,1024
71 20                  ARIVAL(I) = ARIVAL(I+1024)
72                READ(3) (ARIVAL(I),I=1025,2048)
73                INDEX = 1025
74                GO TO 10
75 100            SHOT =0.0
76                FLAG = 1
77                II = 0
78 101            II = II +1
79                SHOT = SHOT + GATE(Q-ARIVAL(INDEX-II),IFLAG)
80                IF (IFLAG.GE.0) GO TO 101
81 C
82 C        THE NEXT LINE TAKES THE SHOT NOISE VALUE AND
83 C        SQUARES IT AND DIVIDES BY THE ATTENUATION
84 C        CONSTANT OF THE PREPROCESSING SECTION.
85 C
```

```
 86                SHOT1 = SHOT*SHOT/40.528
 87                SHOT = SHOT1
 88           RETURN
 89           END
 90 C
 91 C
 92           REAL FUNCTION GATE(X,IFLAG)
 93 C
 94 C         FUNCTION GATE SIMULATES THE COMBINED
 95 C         PREPROCESSING FILTER IMPULSE RESPONSE.
 96 C
 97           REAL PI2
 98           DATA PI2/6.283185307/
 99           IF (X.GT.1.0) GO TO 10
100              G = SIN(PI2*X)
101              IFLAG = 1
102              GATE = G
103           RETURN
104 10           IFLAG = -1
105              GATE = 0.0
106           RETURN
107           END
```

APPENDIX B

RMS PHASE ERROR VERSUS TIME FOR SIMULATION TRIALS

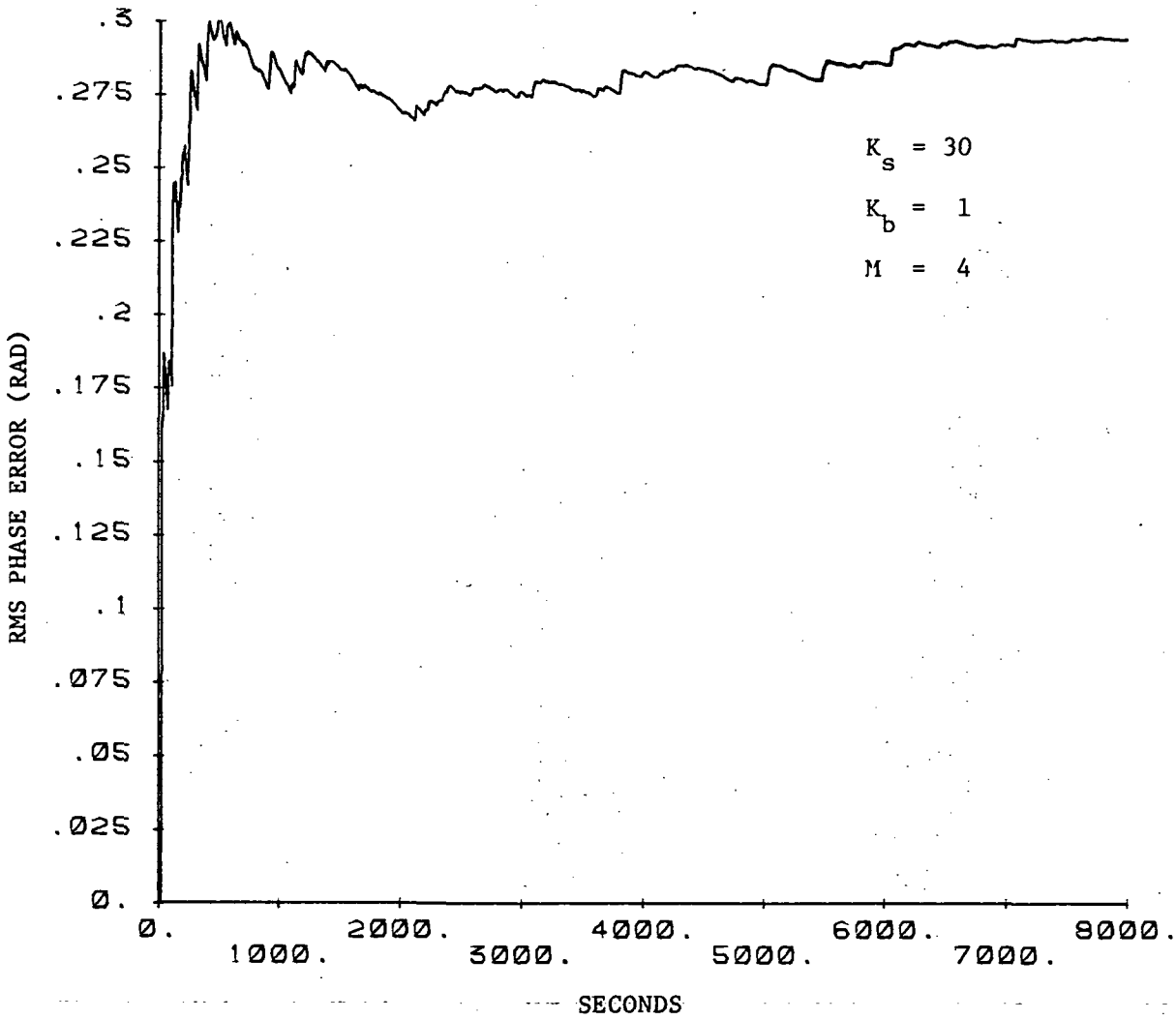

Figure B.1. Simulation trial for $K_s = 30$, $K_b = 1$ and $M = 4$.

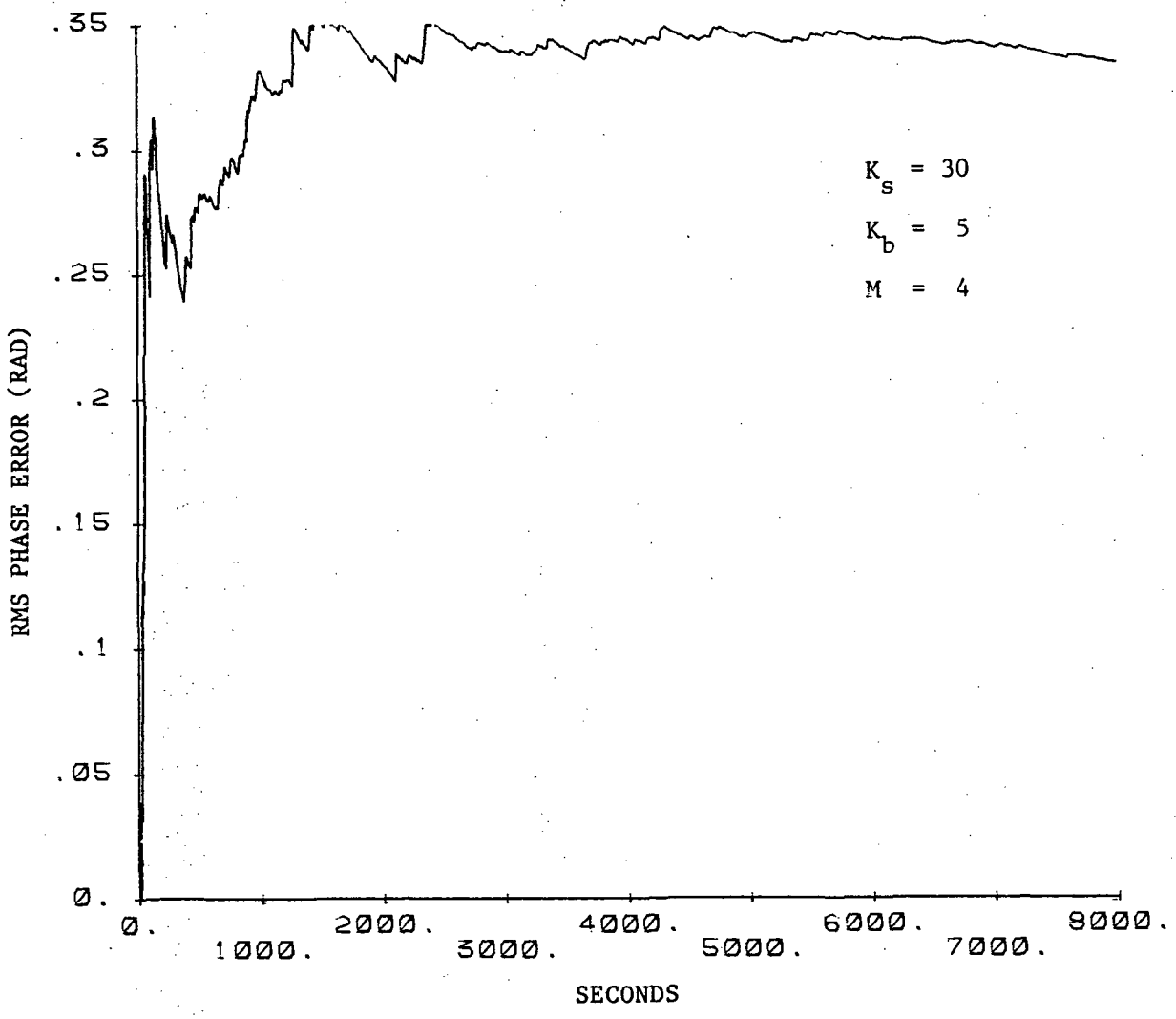

Figure B.2. Simulation trial for K_s = 30, K_b = 5 and M = 4.

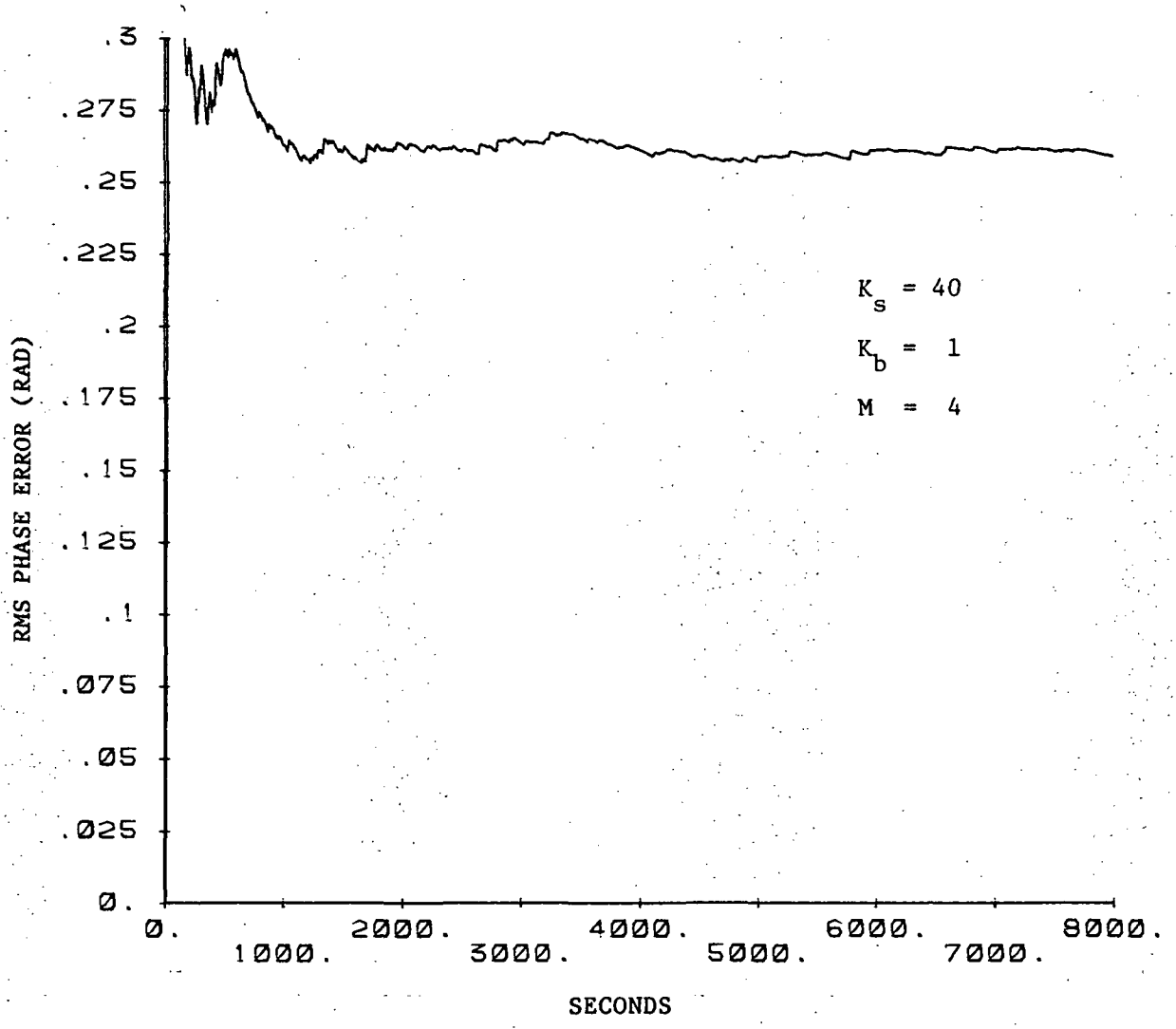

Figure B.3. Simulation trial for $K_s = 40$, $K_b = 1$ and $M = 4$.

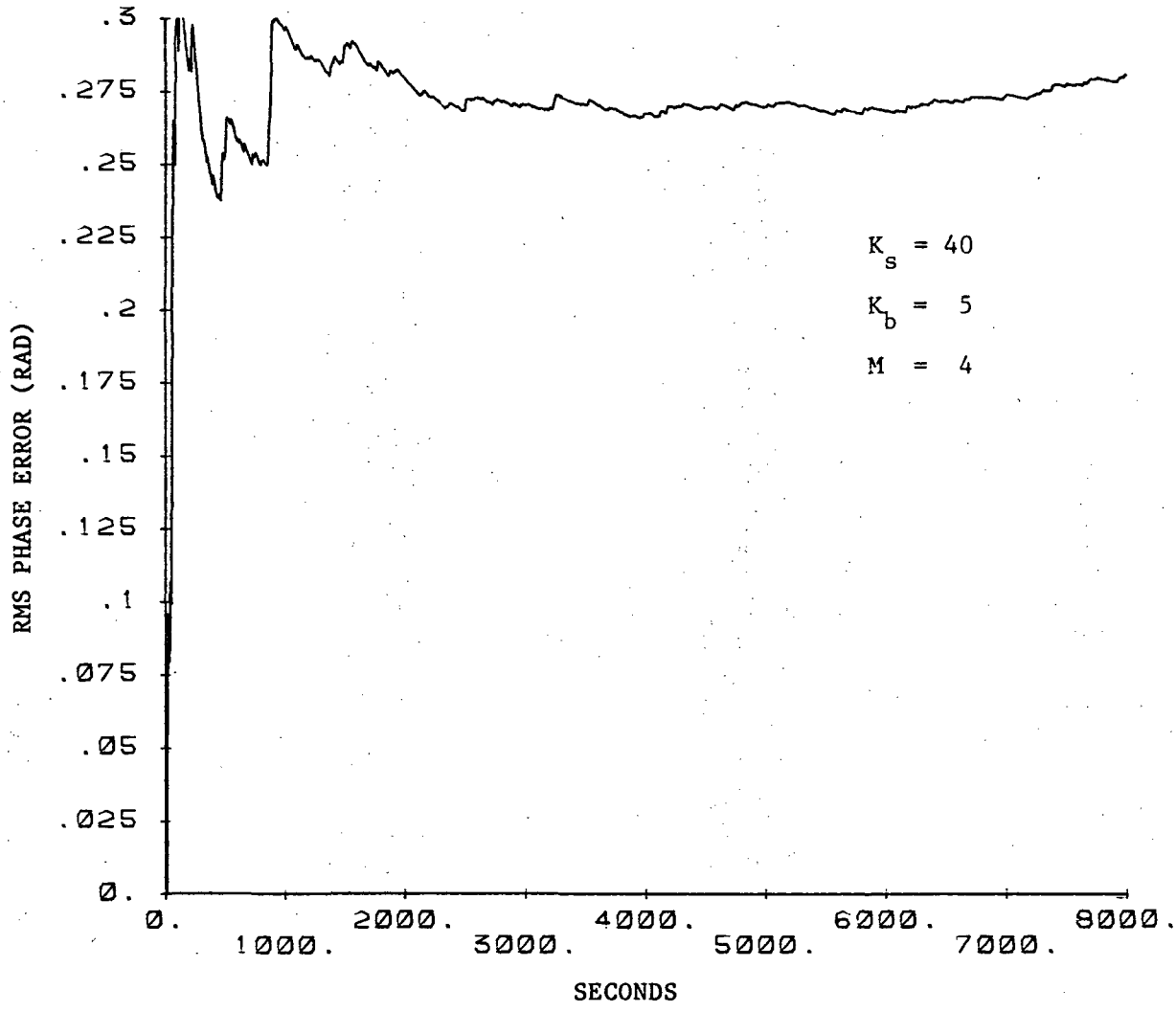

Figure B.4. Simulation trial for $K_s = 40$, $K_b = 5$ and $M = 4$.

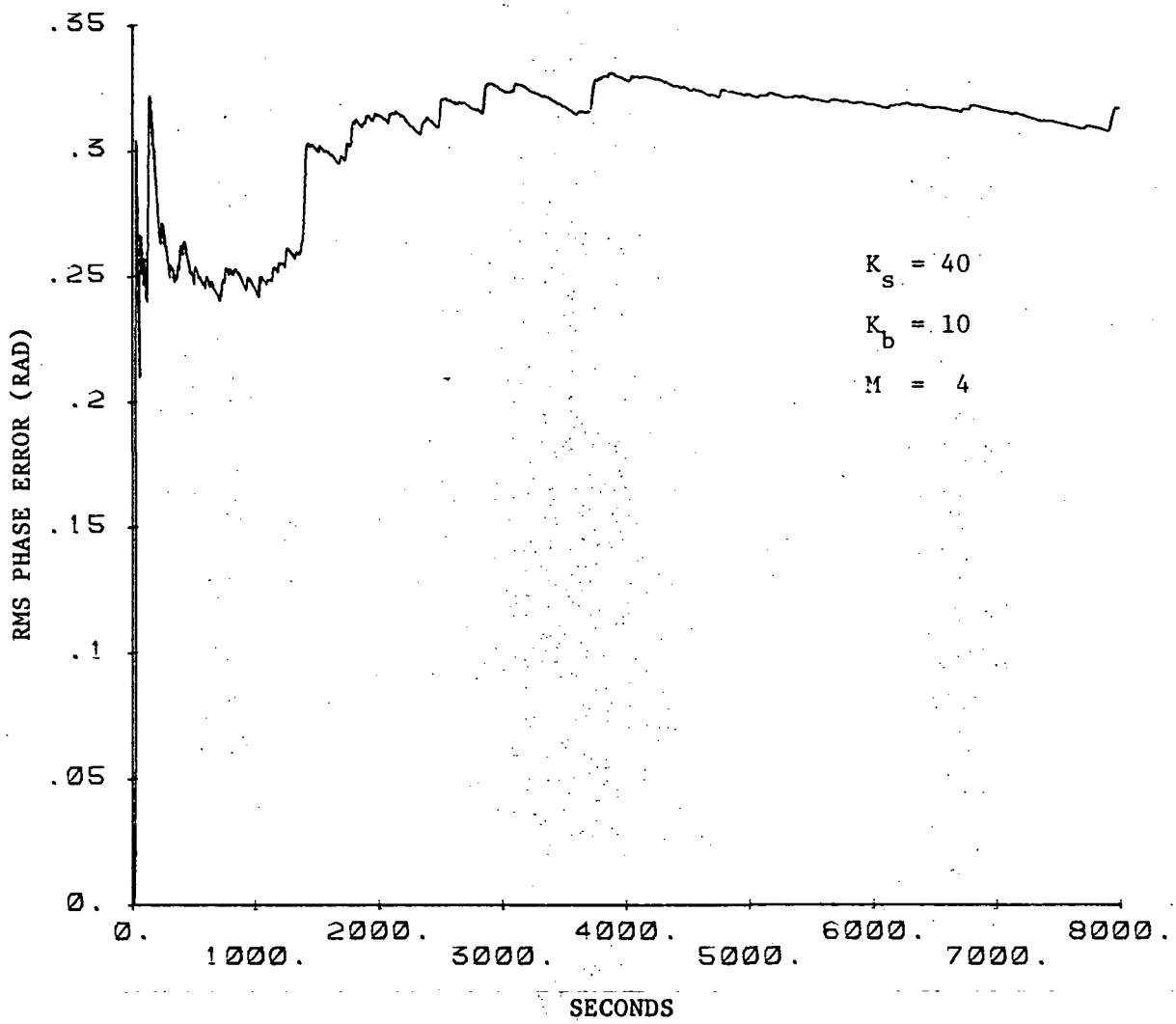

Figure B.5. Simulation trial for $K_s = 40$, $K_b = 10$ and $M = 4$.

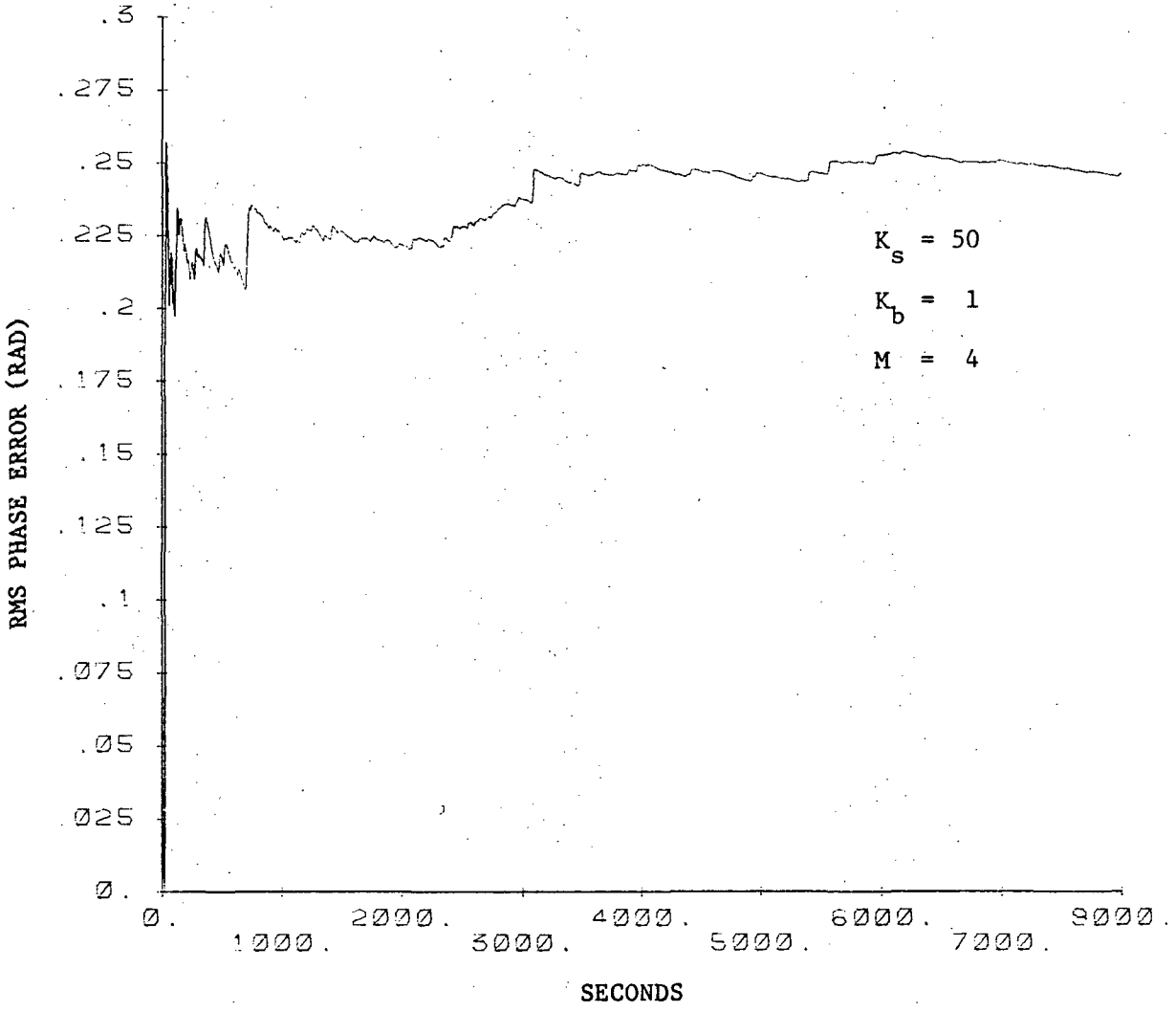

Figure B.6. Simulation trial for K_s = 50, K_b = 1 and M = 4.

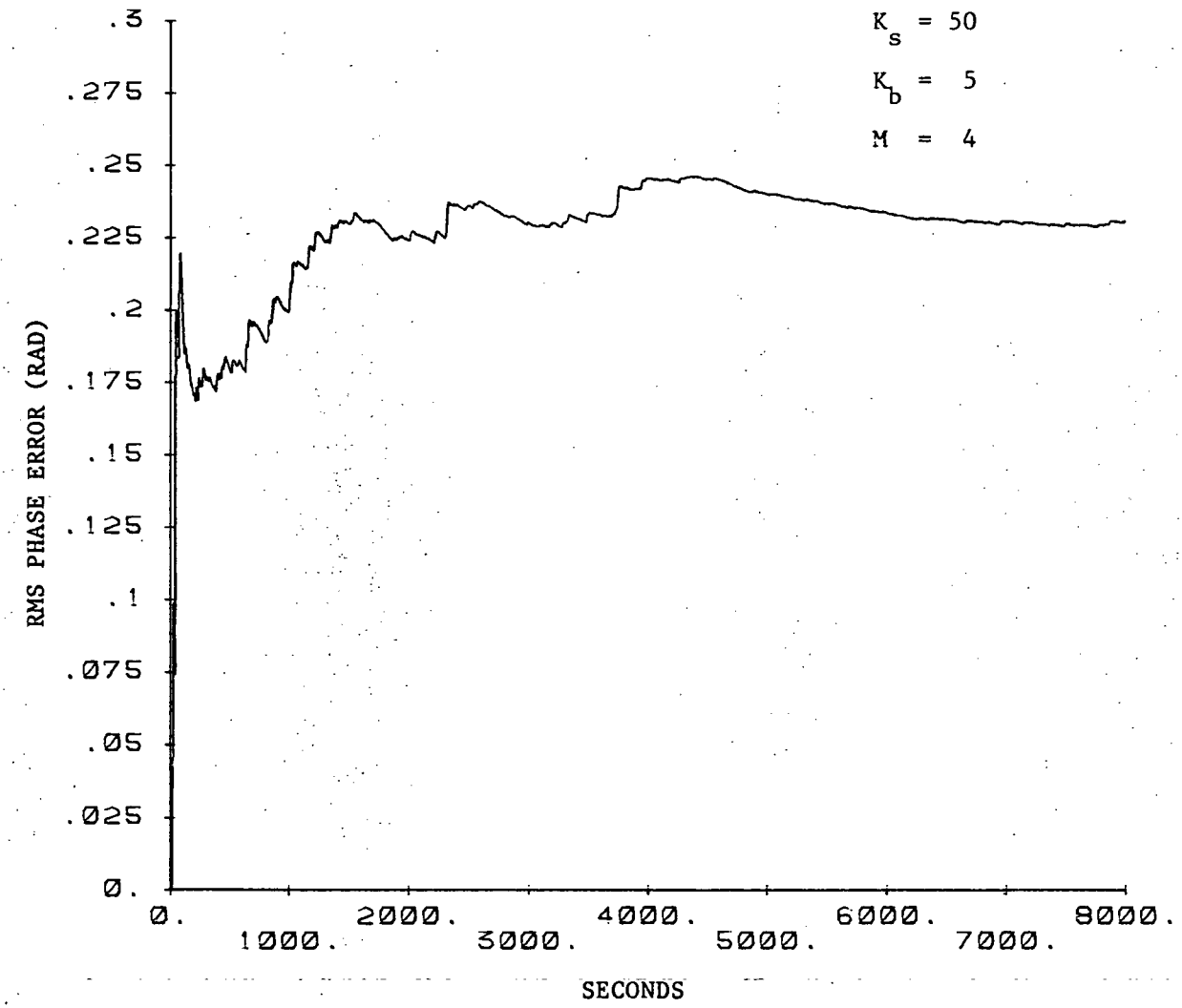

Figure B.7. Simulation trial for K_s = 50, K_b = 5 and M = 4.

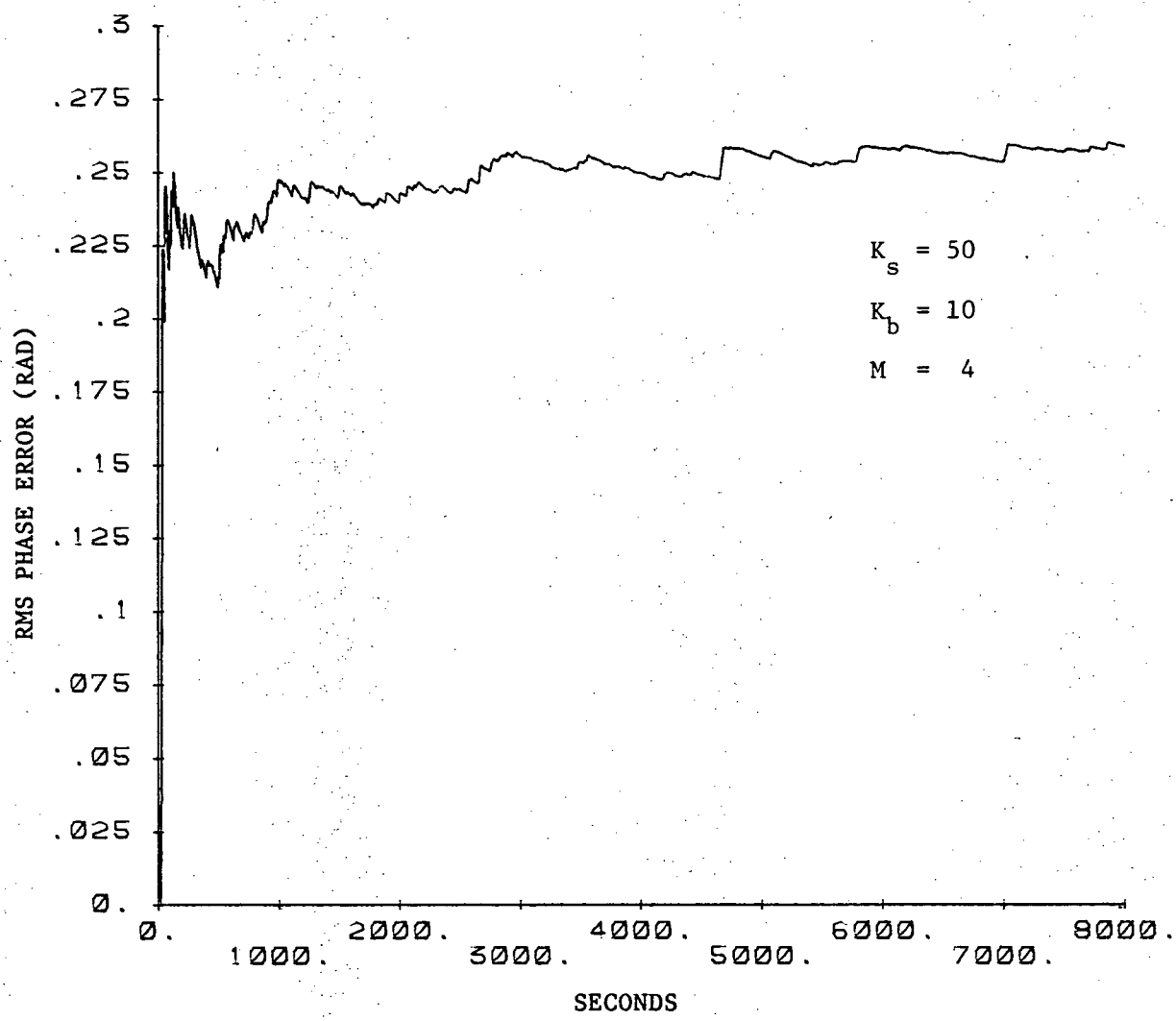

Figure B.8. Simulation trial for $K_s = 50$, $K_b = 10$ and $M = 4$.

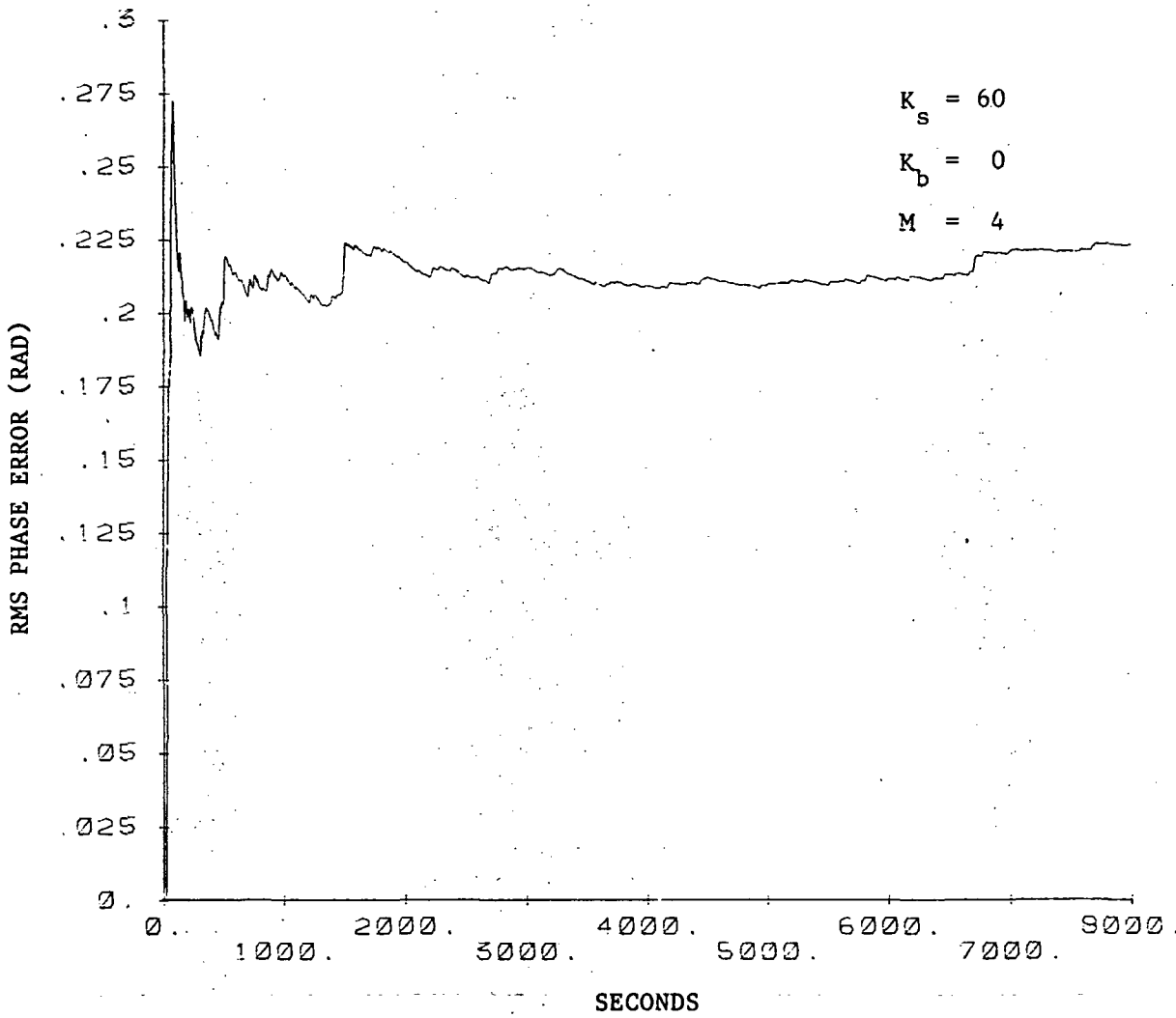

Figure B.9. Simulation trial for $K_s = 60$, $K_b = 0$ and $M = 4$.

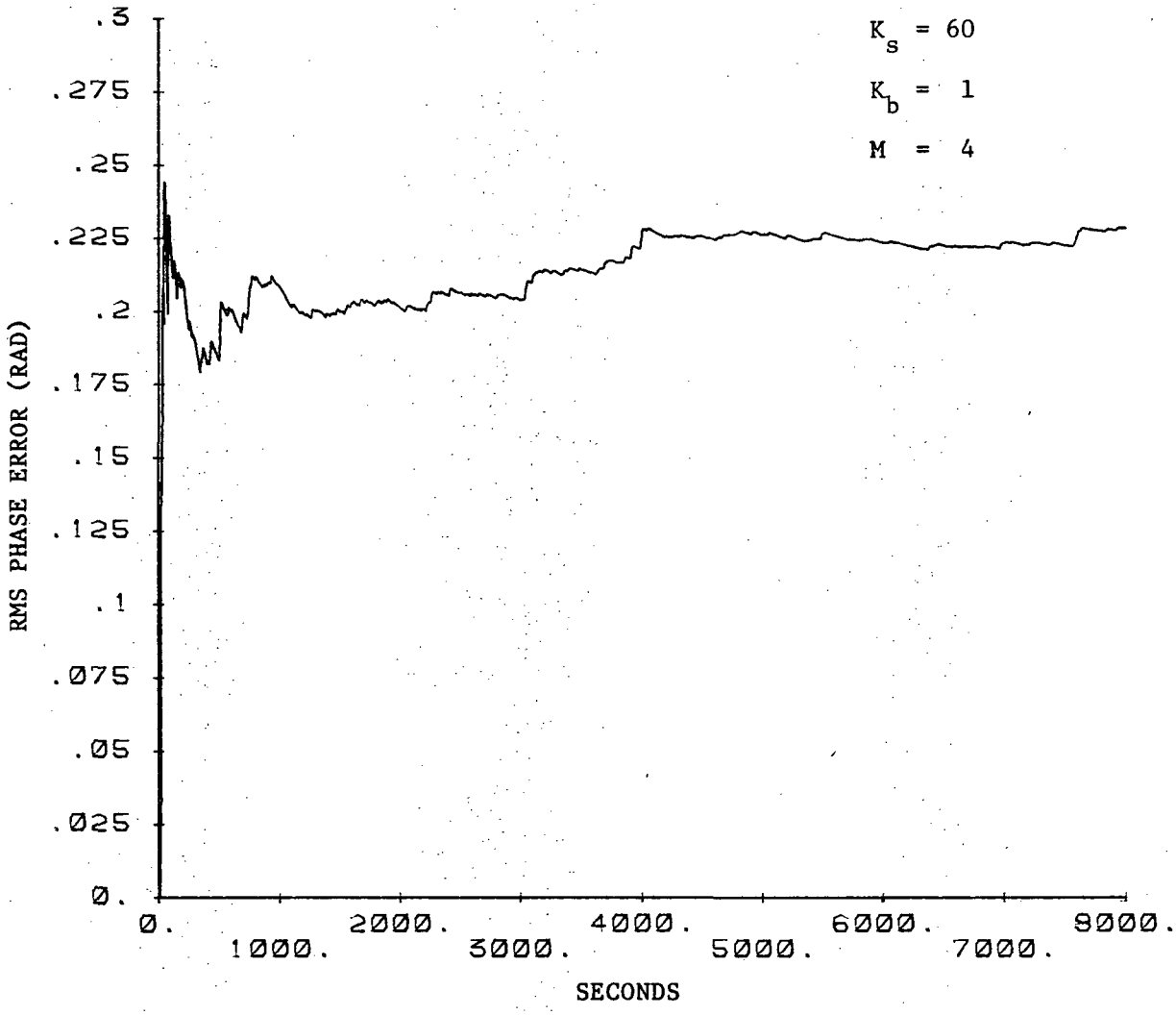

Figure B.10. Simulation trial for K_s = 60, K_b = 1 and M = 4.

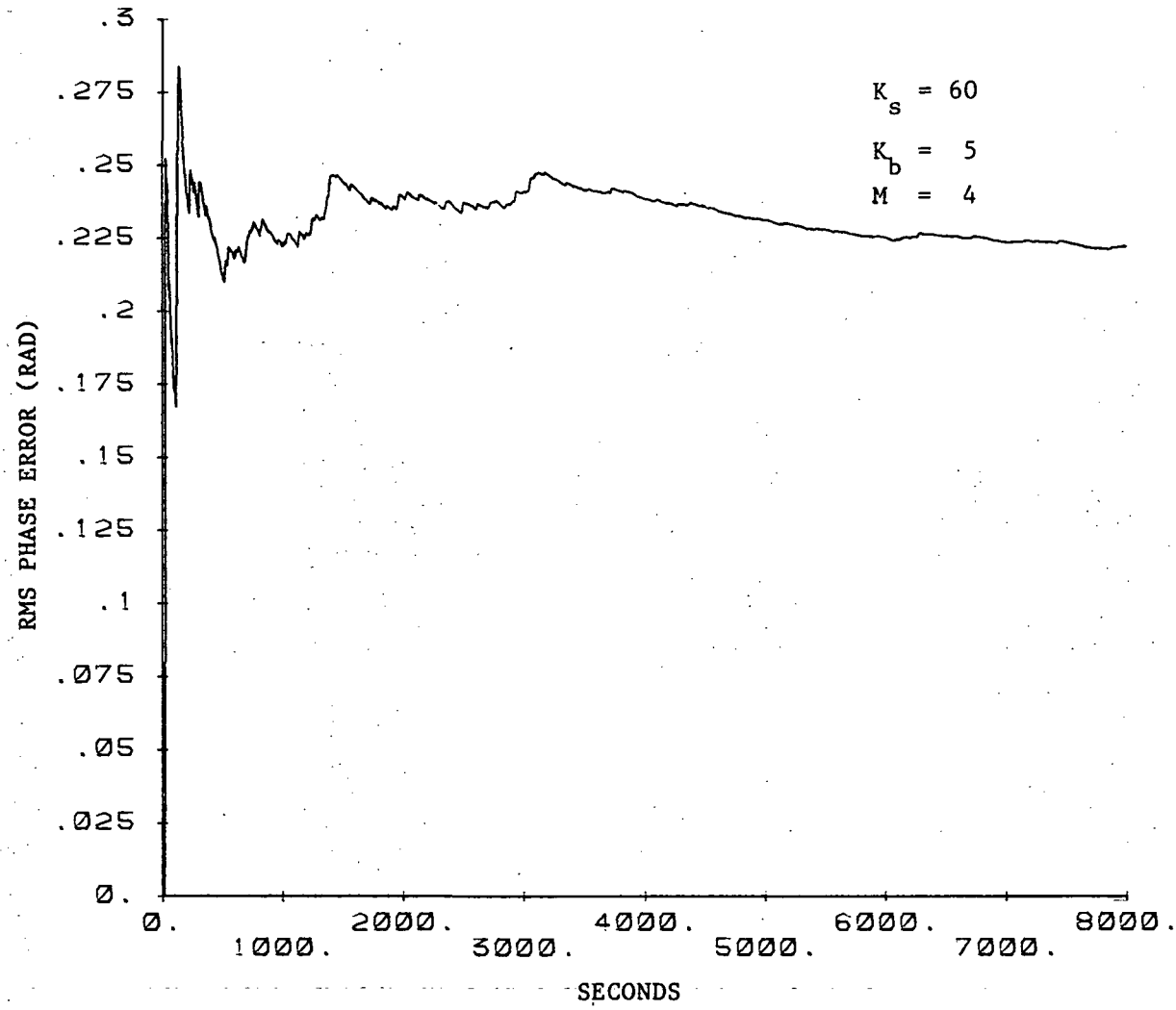

Figure B.11. Simulation trial for K_s = 60, K_b = 5 and M = 4.

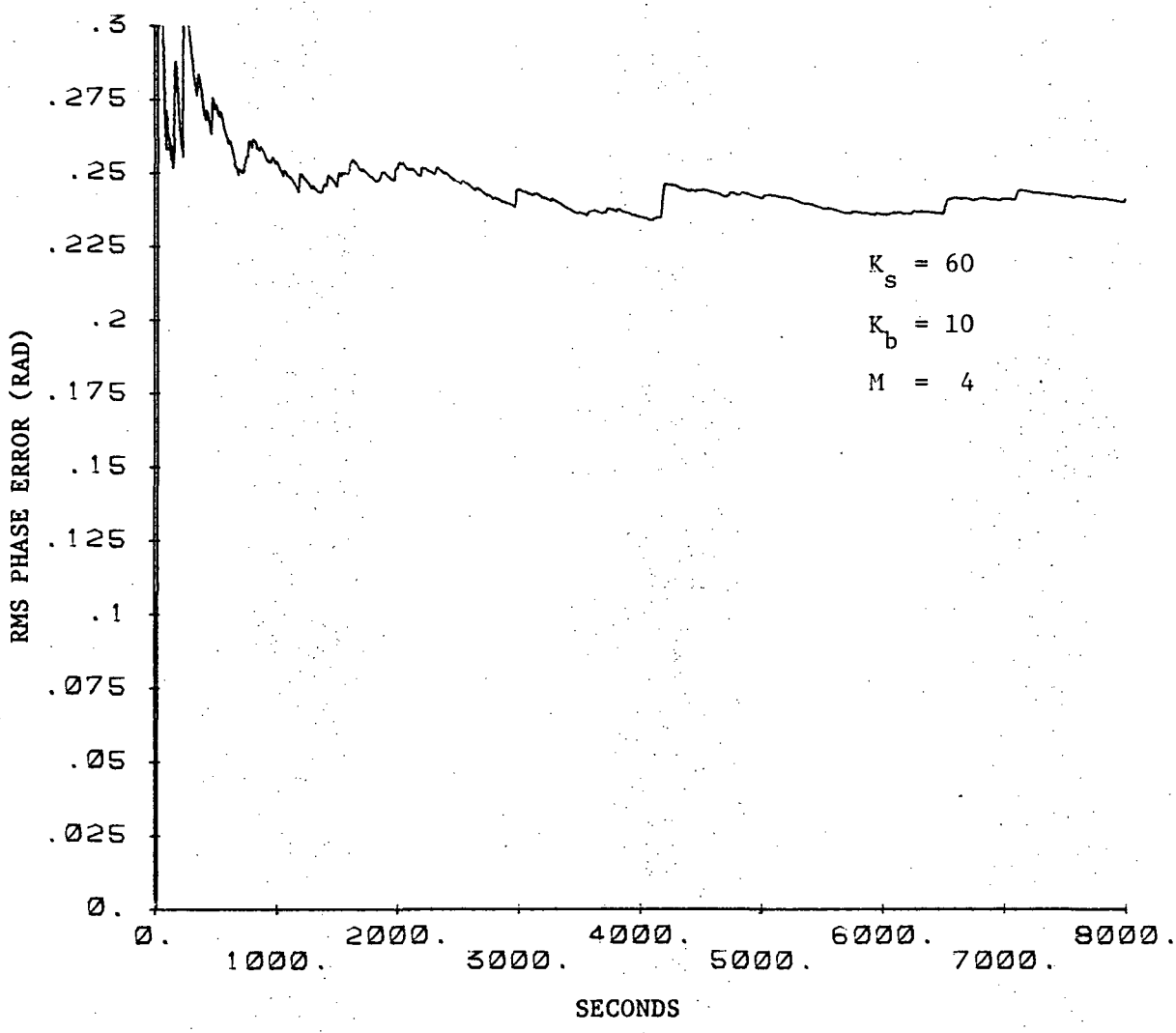

Figure B.12. Simulation trial for K_s = 60, K_b =10 and M = 4.

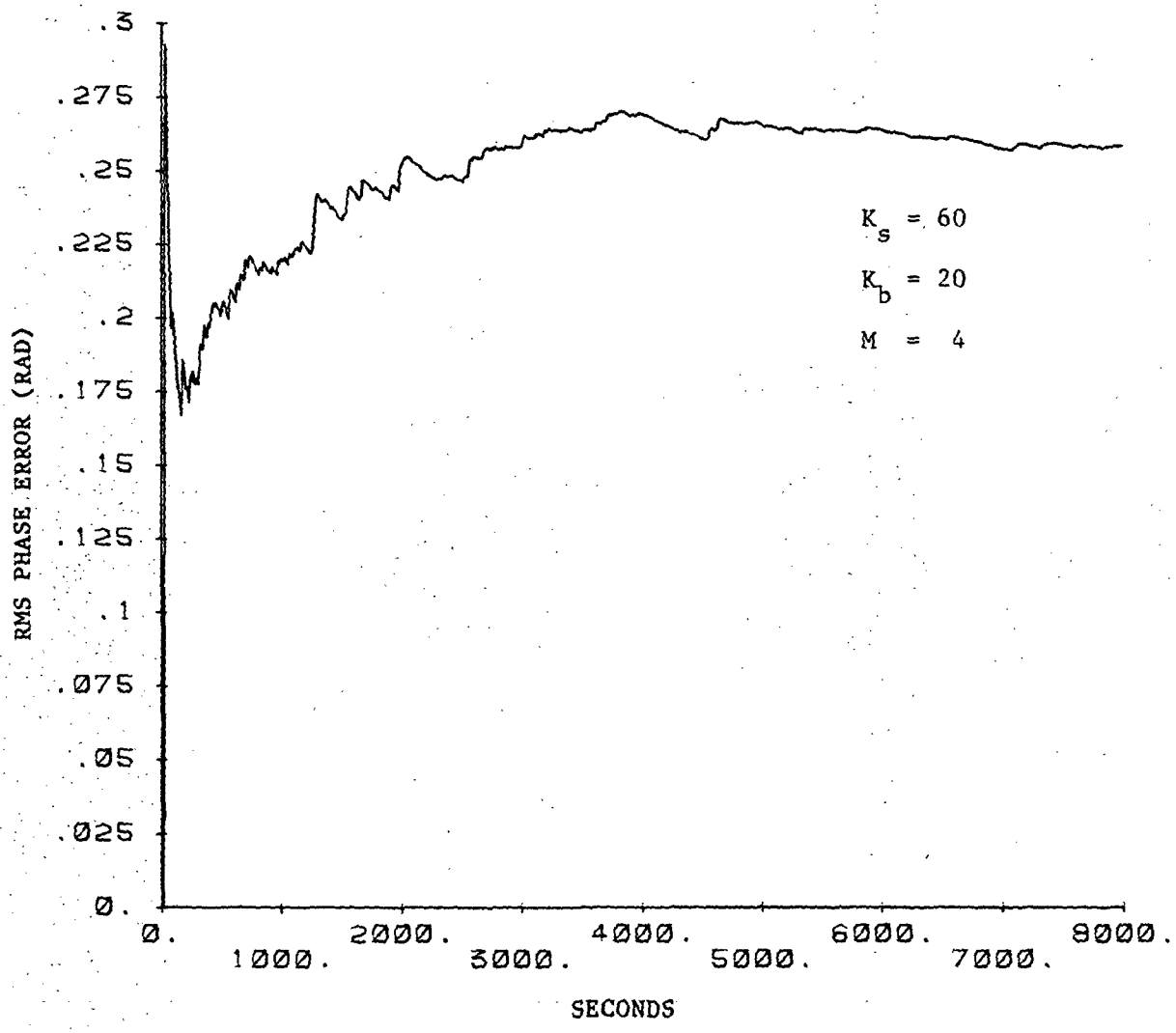

Figure B.13. Simulation trial for $K_s = 60$, $K_b = 20$ and $M = 4$.

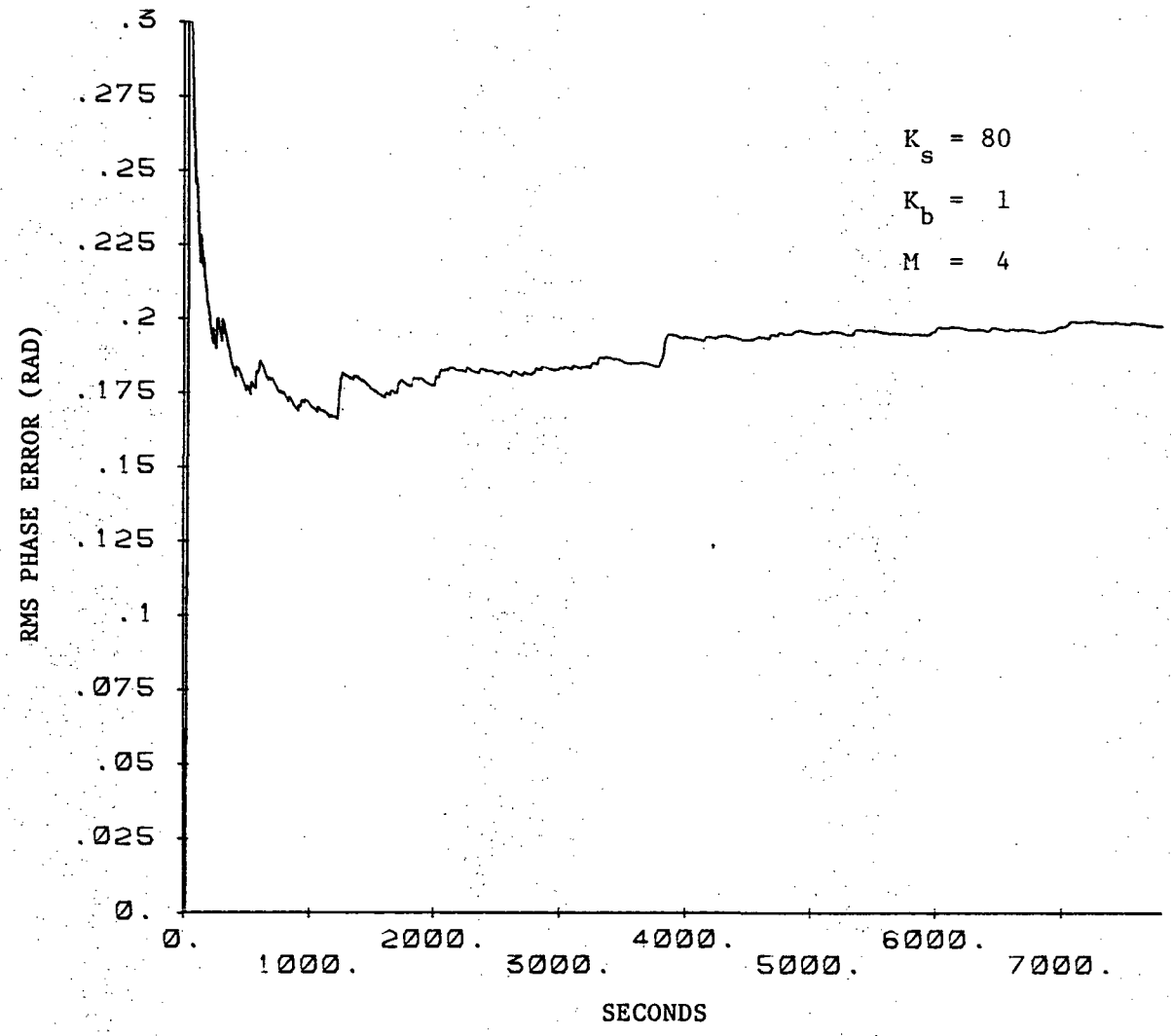

Figure B.14. Simulation trial for K_s = 80, K_b = 1 and M = 4.

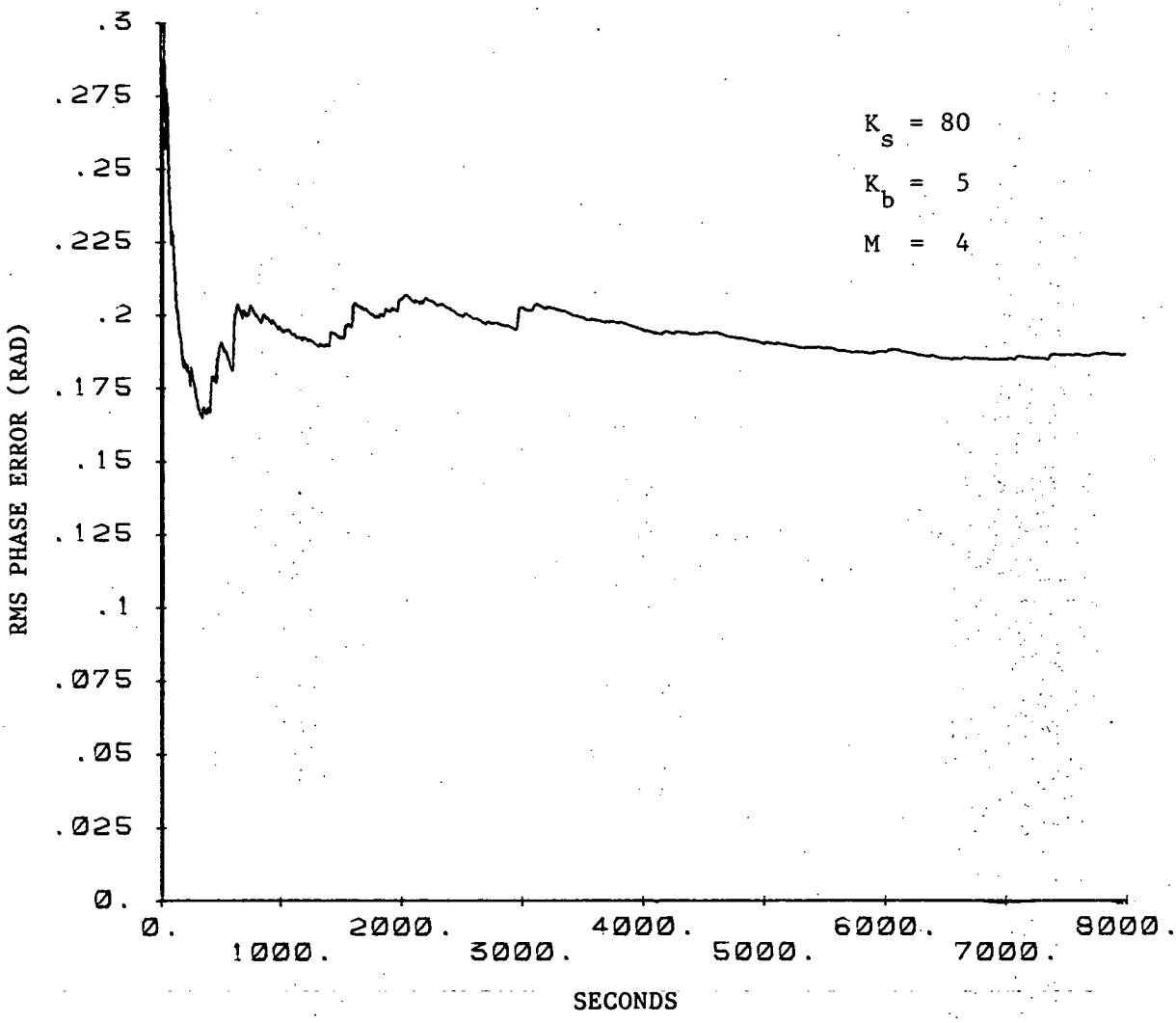

Figure B.15. Simulation trial for K_s = 80, K_b = 5 and M = 4.

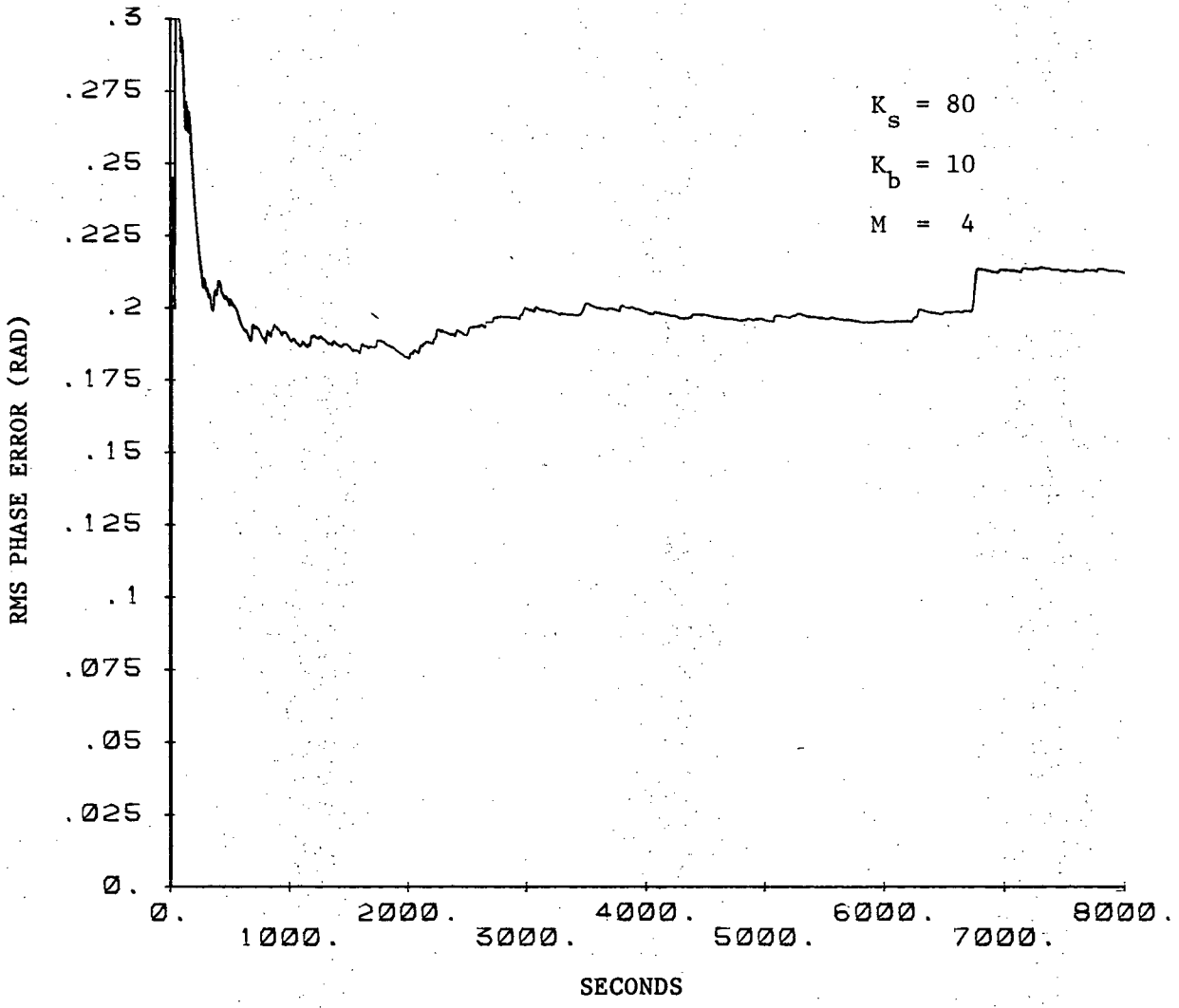

Figure B.16. Simulation trial for K_s = 80, K_b = 10 and M = 4.

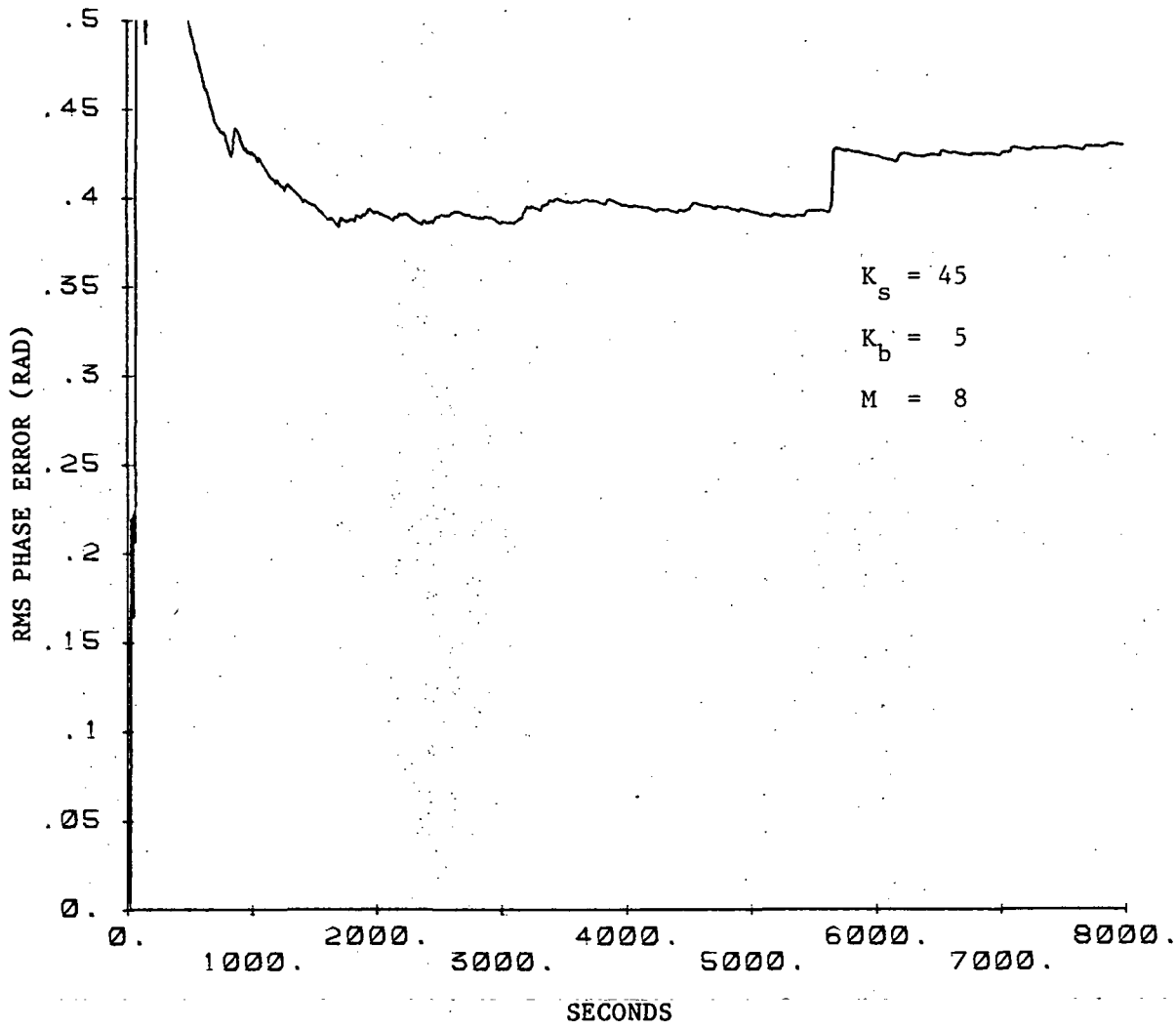

Figure B.17. Simulation trial for K_s = 45, K_b = 5 and M = 8.

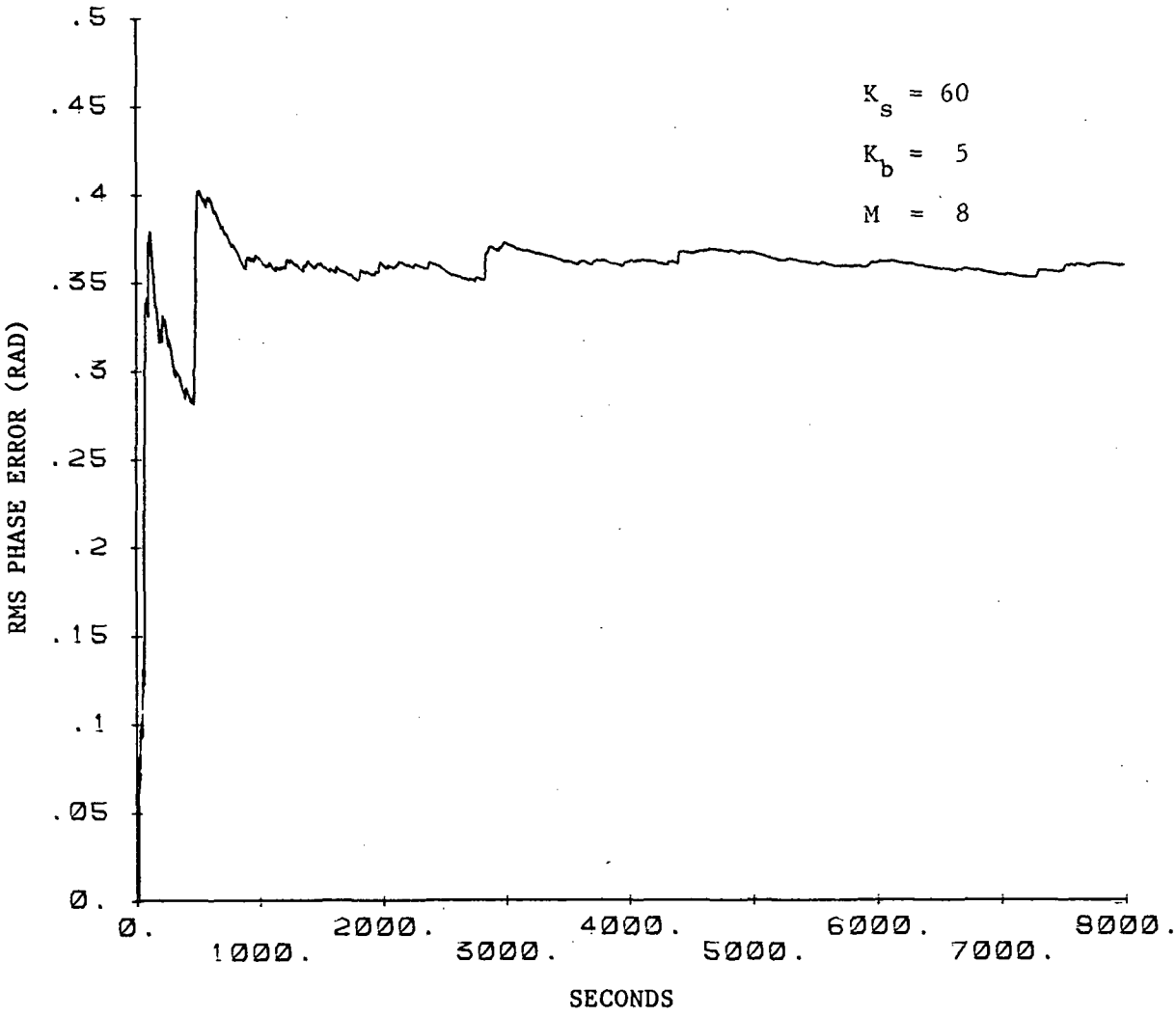

Figure B.18. Simulation trial for K_s = 60, K_b = 5 and M = 8.

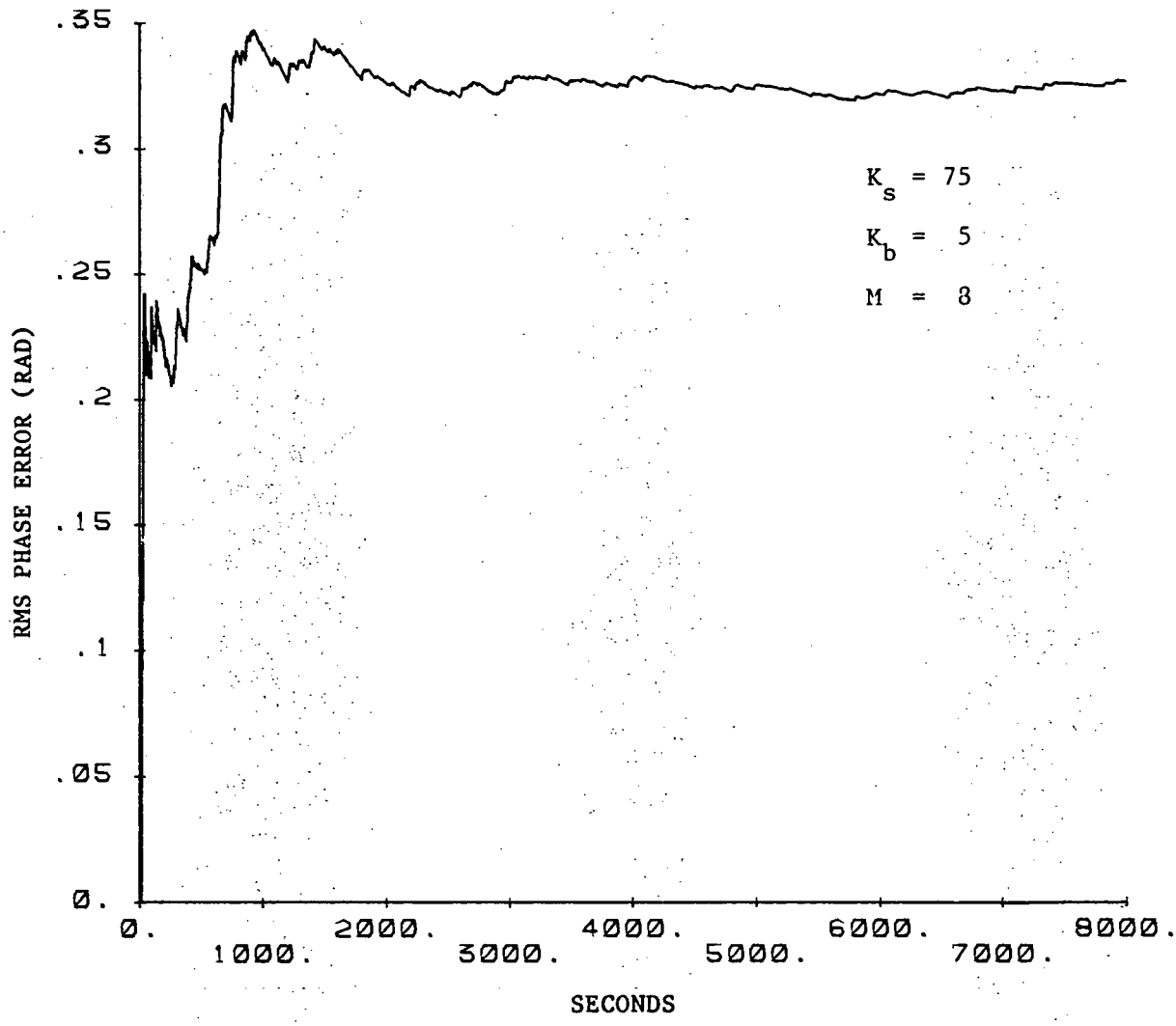

Figure B.19. Simulation trial for K_s = 75, K_b = 5 and M = 8.

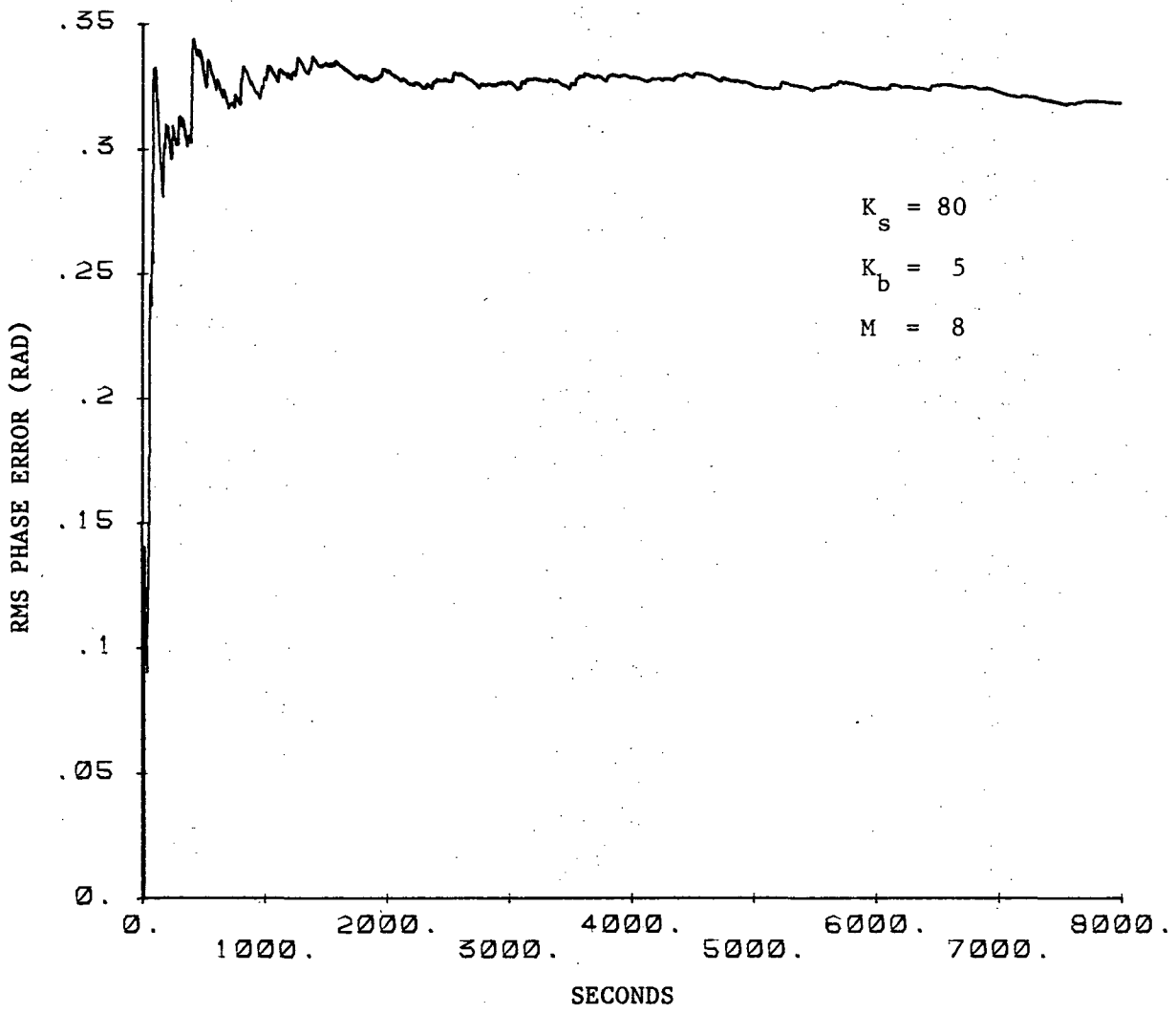

Figure B.20. Simulation trial for K_s = 80, K_b = 5 and M = 8.

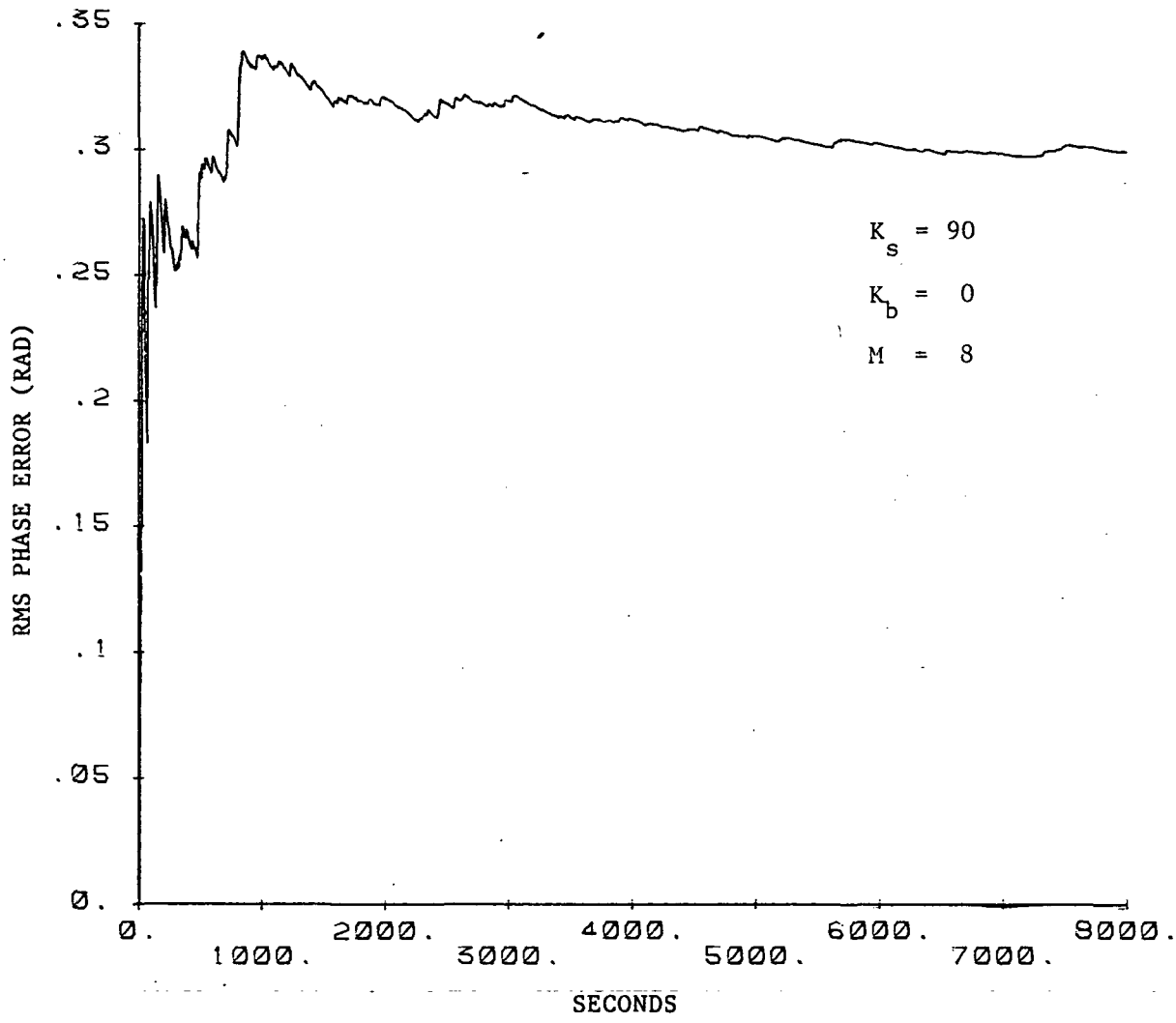

Figure B.21. Simulation trial for $K_s = 90$, $K_b = 0$ and $M = 8$.

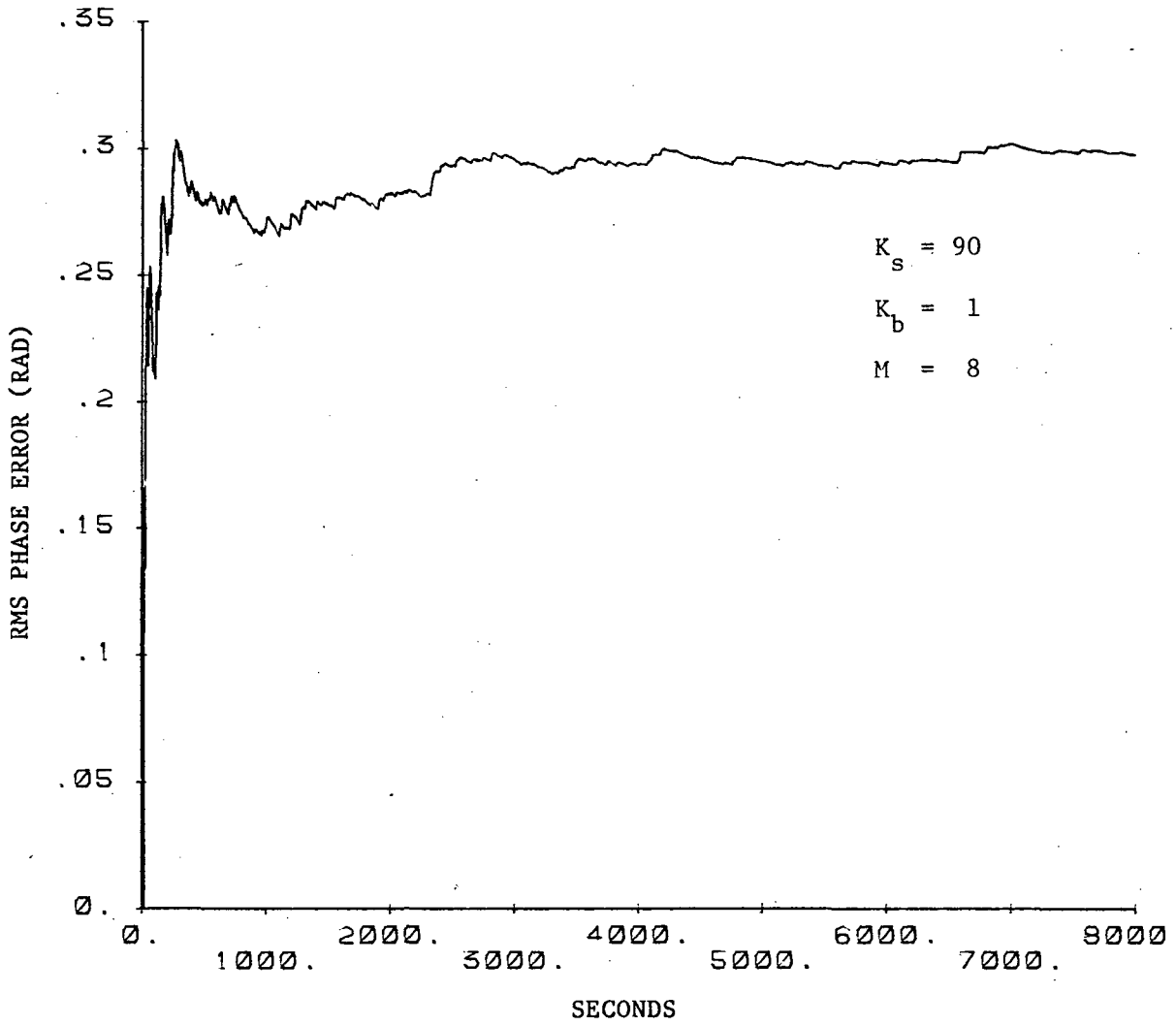

Figure B.22. Simulation trial for K_s = 90, K_b = 1 and M = 8.

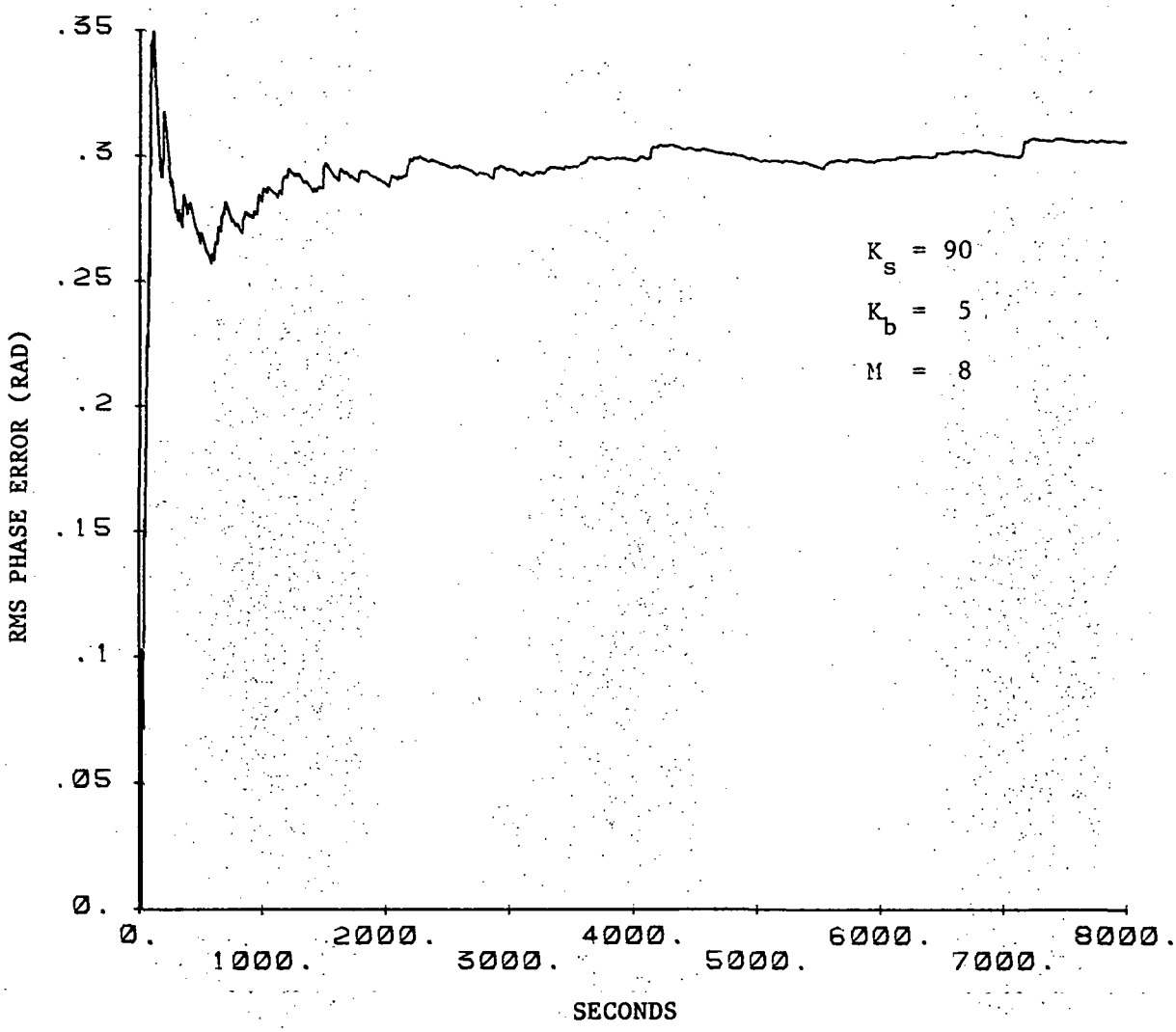

Figure B.23. Simulation trial for K_s = 90, K_b = 5 and M = 8.

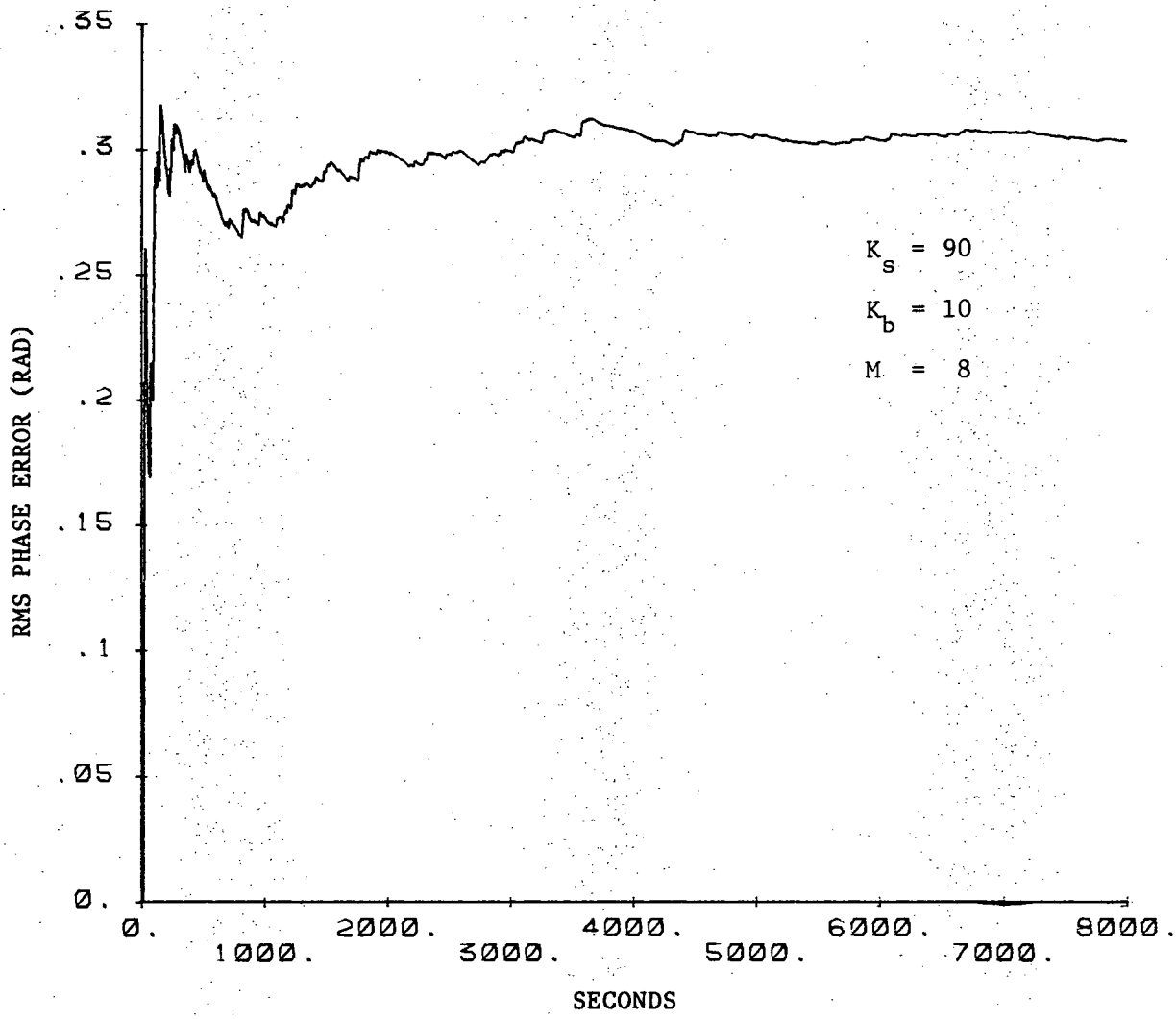

Figure B.24. Simulation trial for K_s = 90, K_b = 10 and M = 8.

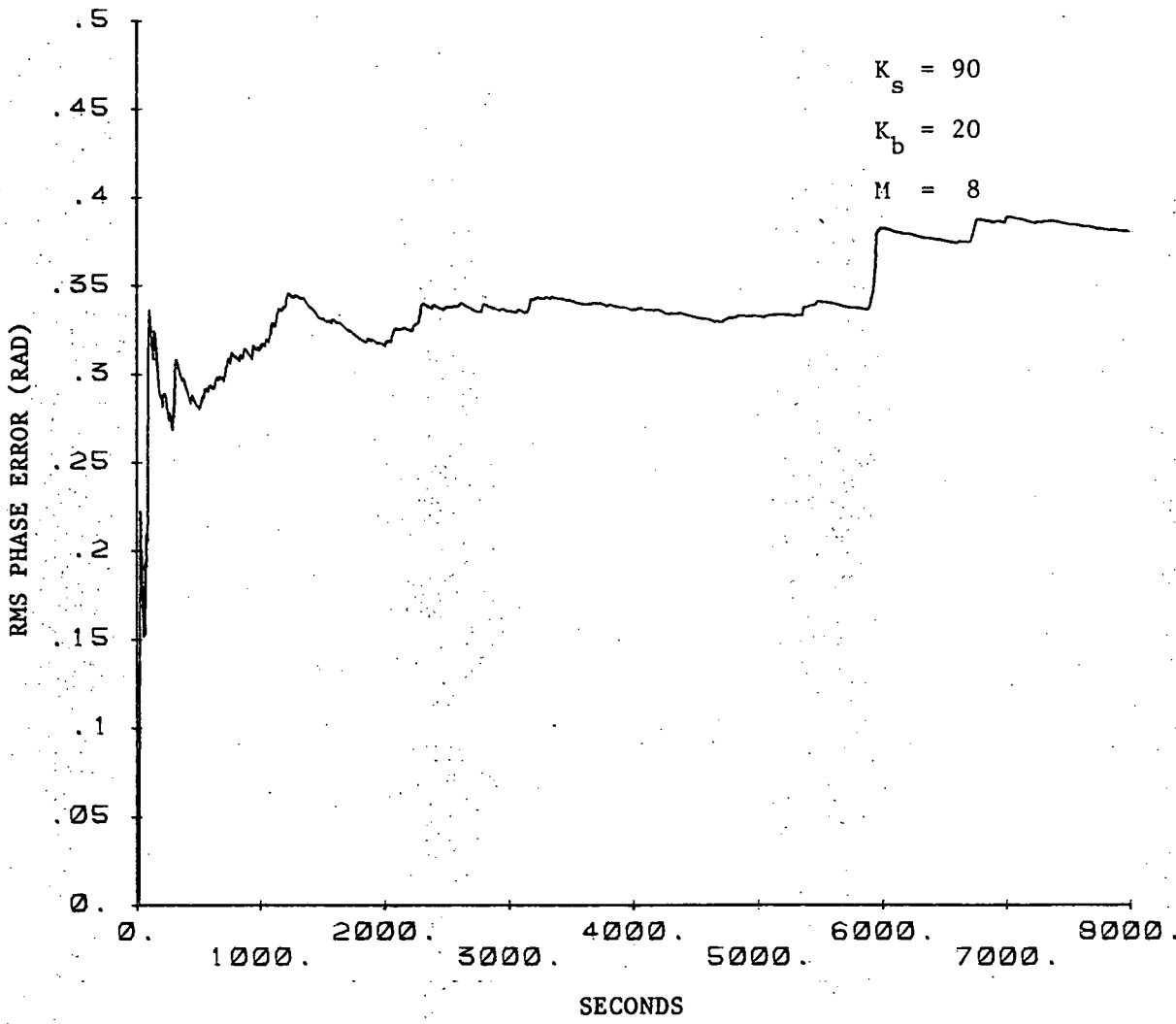

Figure B.25. Simulation trial for K_s = 90, K_b = 20 and M = 8.

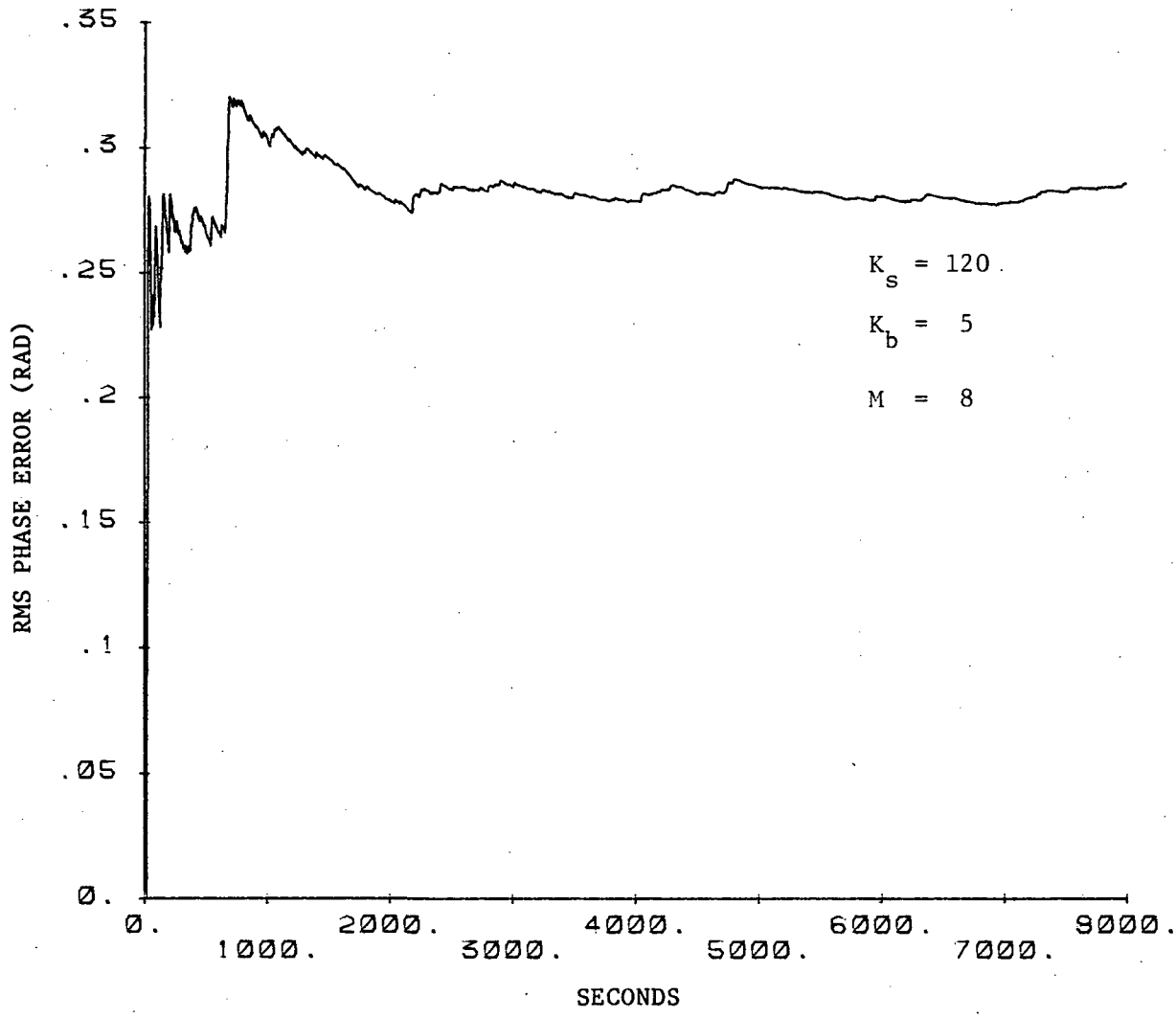

Figure B.26. Simulation trial for K_s = 120, K_b = 5 and M = 8.

REFERENCES

1. Galiardi, R., "The effects of timing errors in optical digital systems," IEEE Trans. Comm., vol. COM-20, no. 2, pp. 87-93, April 1972.

2. Mengali, U. and Pezzani E., "Tracking properties of phase-locked loops in optical communication systems," IEEE Trans. Comm., vol. COM-26, no. 12, pp. 1811-1818, December 1978.

3. Gagliardi, R. and Haney M., "Optical synchronization-phase locking with shot noise processes," USCEE Report 396, University of Southern California, Los Angeles; California, August 1970.

4. Galiardi, R. and Karp, S., Optical Communications. New York: John Wiley and Sons, 1976.

5. Gardner, F. M., Phaselock Techniques. New Jersey: John Wiley and Sons, 1966.

6. Viterbi, A. J., Principles of Coherent Communication. New York: McGraw-Hill Book Company, 1966.

7. Goodman, J. W., Introduction to Fourier Optics. New York: McGraw-Hill Book Company, 1968.

8. Klein, B. J. and Degnan, J. J., "Optical antenna gain. 1: Transmitting antennas," Applied Opt., vol. 13, pp. 2134-2141, September 1974.

9. Klein, B. J. and Degnan, J. J., "Optical antenna gain. 3: The effect of secondary support struts on transmitter gain," Applied Opt., vol. 15, pp. 977-979, April 1976.

10. Pratt, W. K., Laser Communication Systems. New York: John Wiley and Sons, 1969.

11. Snyder, D. L., Random Point Processes. New York: John Wiley and Sons, 1975.

12. Chen, C., personal communication.

CUMULATIVE LIST OF RADIO RESEARCH LABORATORY
AND ELECTRO-OPTIC SYSTEMS LABORATORY REPORTS
PREPARED UNDER NASA GRANT NSG-5049

RRL Rep. No. 469 - Gardner, C. S. (December 1975), The Effects of Random Path Fluctuations on the Accuracy of Laser Ranging Systems.

RRL Rep. No. 471 - Zanter, D. L., C. S. Gardner and N. N. Rao (January 1976), The Effects of Atomospheric Refraction on the Accuracy of Laser Ranging Systems.

RRL Rep. No. 477 - Gardner, C. S. and J. R. Rowlett (November 1976), Atmospheric Refraction Errors in Lasar Ranging Data.

RRL Rep. No. 478 - Gardner, C. S. and B. E. Hendrickson (December 1976), Correction of Laser Ranging Data for the Effects of Horizontal Refractivity Gradients.

RRL Rep. No. 481 - Gardner, C. S. (January 1977), Statistics of the Residual Refraction Errors in Laser Ranging Data.

RRL Rep. No. 486 - Gardner, C. S. (June 1977), Comparison Between the Refraction Error Covariance Model and Ray Tracing.

RRL Rep. No. 488 - Gardner, C. S. (December 1977), Speckle Noise in Satellite Based Lidar Systems.

RRL Rep. No. 495 - Gardner, C. S. and G. S. Mercherle (April 1978), Speckle Noise in Direct-Detection Lidar Systems.

RRL Rep. No. 496 - Gardner, C. S. and A. M. Saleh (October 1978), Speckle Noise in Differeintial Absortion Lidar Systems.

RRL Rep. No. 499 - Gardner, C. S. (January 1979), A Technique for Remotely Measuring Surface Pressure from a Satellite Using a Multicolor Laser Ranging System.

RRL Rep. No. 502 - Palluch, E., J. Shelton and C. S. Gardner (May 1979), Operating Manual for the RRL 8 Channel Data Logger.

RRL Rep. No. 505 - Gardner, C. S. and R. Axford, Jr. (March 1980), Regression Models for Multicolor Satellite Laser Ranging.

RRL Rep. No. 510 - Gardner, C. S. (April 1981), Analysis of Target Signatures for Laser Altimeters.

RRL Rep. No. 514 - Tsai, B. and C. S. Gardner (December 1981), Remote Sensing of Sea State by Laser Altimeters.

RRL Rep. No. 518 - Gardner, C. S. (August 1982), Optical Communications.

RRL Rep. No. 519 - Im, K. E. and C. S. Gardner (September 1982), Atmospheric Refraction Effects on Baseline Error in Satellite Laser Ranging Systems.

RRL Rep. No. 526 - Im, K. E., B. M. Tsai, and C. S. Gardner (September 1983), Analysis of Short Pulse Laser Altimetry Data Obtained Over Horizontal Path.

RRL Rep. No. 527 - Tsai, B. M. and C. S. Gardner (March 1984), Theoretical and Experimental Analysis of Laser Altimeters for Barometric Measurements Over the Ocean.

EOSL Rep. No. 84-001 - Lafaw, D. A. and C. S. Gardner (August 1984), Timing Performance of Phase-Locked Loops in Optical Pulse Position Modulation Communication Systems.

PAPERS PUBLISHED

C. S. Gardner, "Effects of Random Path Fluctuations on the Accuracy of Laser Ranging Data," Applied Optics, 15, 2539-2545, October 1976.

C. S. Gardner, "Effects of Horizontal Refractivity Gradients on the Accuracy of Laser Ranging to Satellites," Radio Science, 11, 1037-1044, December 1976.

C. S. Gardner, "Correction of Laser Tracking Data for the Effects of Horizontal Refractivity Gradients," Applied Optics, 16, 2427-2432, September 1977.

C. S. Gardner, R. Rowlett, and B. E. Hendrickson, "Ray Tracing Evaluation of a Technique for Correcting the Refraction Errors in Satellite Tracking Data," Applied Optics, 17, 3143-3145, October 1978.

C. S. Gardner, "Technique for Remotely Measuring Surface Pressure from a Satellite Using a Multicolor Laser Ranging System," Applied Optics, 18, 3184=3189, September 15, 1979.

C. S. Gardner, "Target Signatures for Laser Altimeters: An Analysis," Applied Optics, 21, 448-453, February 1, 1982.

B. M. Tsai and C. S. Gardener, "Remote Sensing of Sea State Using Laser Altimeters," Applied Optics, 21, 3932-3940, November 1, 1982.

C. S. Gardner, B. M. Tsai and J. B. Abshire, "Remote Sensing of Atmospheric Pressure and Sea State from Satellites Using Short-Pulse Multicolor Laser Altimeters," Proceedings of NATO-AGARD Symposium on Propogation Factors Affecting Remote Sensing by Radio Waves, Oberammergau, FRG, May 24-28, 1983.

C. S. Gardner, B. M. Tsai and K. E. Im, "Multicolor Laser Altimeters for Barometric Measurements over the Ocean: Theorectical," Applied Optics, 22, September, 1983.